FACULDADE DE ENGENHARIA DA UNIVERSIDADE DO PORTO

# Study of different element formulations for the finite element analysis of a roll forming process

**Diogo Forte**




Integrated Master in Mechanical Engineer

Supervisors:

Dr. Thomas Dietl

Prof. Dr. Abel Santos

M.Sc. Miguel Pereira

ir. André Abee

Dipl.-Ing. Johann Harrasser

June 28, 2021

# Study of different element formulations for the finite element analysis of a roll forming process

**Diogo Forte**

Integrated Master in Mechanical Engineer

June 28, 2021

# Abstract

Roll forming is a metal forming manufacturing process used to obtain profiles with the desired cross-section by continuously bending a sheet through a series of rolls. Manufacturing parts through roll forming can be extremely advantageous given the complexity of shapes that can be achieved and the high productivity of the process.

The software COPRA® FEA RF allows to simulate, study and validate the designed roll forming process using finite element analysis in order to optimize the roll forming line assuring good profile quality and trouble-free manufacturing. The software package creates models using, by default, hexahedral solid elements. With the surge of new developments in finite element analysis, the current project aims to explore new element formulations to create models that yield results faster than the standard model used by COPRA® FEA RF.

The different element types were first studied through a series of simple tests which replicated the forming mechanisms involved in roll forming. The preliminary tests allowed to get insights into the behavior of the different element types and to tune certain model parameters.

Subsequently, the behavior of elements was tested by finite element analysis of a roll forming process. Most of the conclusions drawn during the simple element tests complied with the results of the roll forming tests. When using shell elements, five is the minimum number of integration layers for the correct representation of bending, and contact parameters can be tuned in order to solve convergence issues. The usage of only one layer of solid elements has some limitations, such as in the representation of in-plane shear and of total equivalent plastic strain. Models with shell elements with reduced integration, solid shell elements, and thick shell elements, all with five layers of integration, can be used to reduce computation time, but with some drawbacks in depicting product defects such as end flare and edge wave. The model with thick shell elements and seven layers of integration is the only model to correctly picture the geometry of the bends but at the cost of a higher computation time. The model with thin shell elements incorrectly represents the geometry of the profile in both bends, making it an unattractive option.

# Resumo

Perfilagem a frio é um processo de conformação usado para obter perfis com uma determinada secção através da dobragem de uma chapa em sucessivos rolos. Produzir componentes através de prefilagem pode ser extremamente vantajoso dada a complexidade de formas que podem ser obtidas e dada a elevada produtividade do processo.

O software COPRA® FEA RF permite simular, estudar e validar o processo de perfilagem desenhado através da utilização de análise de elementos finitos, por forma a otimizar a linha de perfilagem e a garantir a boa qualidade do perfil e a não-existência de problemas de produção. Este software cria modelos que, por predefinição, utilizam elementos sólidos hexaédricos. Dado o aparecimento de novos avanços na área de análise de elementos finitos, o presente trabalho tem como objetivo explorar novas formulações de elementos para criar modelos que forneçam resultados mais rapidamente que o modelo pré-definido utilizado pelo COPRA® FEA RF.

Diferentes tipos de elementos foram estudados através de uma série de testes simples, os quais replicaram os mecanismos de deformação envolvidos na perfilagem. Estes testes preliminares permitiram obter informação quanto ao comportamento dos diferentes tipos de elementos e ajustar alguns parâmetros dos modelos.

Posteriormente, testou-se o comportamento dos elementos através da análise de elementos finitos aplicada à perfilagem. A maioria das conclusões retiradas durante os testes simples estão de acordo com os resultados dos testes de perfilagem. Ao usar elementos de casca, cinco é o número mínimo de camadas de integração para garantir uma correta representação da dobragem da chapa, e os parâmetros de definição de contacto podem ser ajustados por forma a evitar problemas de convergência. Utilizar apenas uma camada de elementos sólidos tem algumas limitações, como por exemplo na representação dos esforços de corte no plano da chapa e na representação do valor acumulado da deformação plástica equivalente. Modelos com elementos de casca com integração reduzida, com elementos híbridos entre sólidos e cascas, e com elementos de casca grossa, todos com cinco camadas de integração, podem ser utilizados por forma a reduzir o tempo de computação, mas com algumas limitações em retratar defeitos como o alargamento nas pontas e ondulação na borda do produto. O modelo com elementos de casca grossa e sete camadas de integração é o unico a representar corretamente a geometria das dobras mas à custa de um maior tempo de computação. O modelo com elementos de casca fina não é uma boa opção na medida em que não retrata corretamente a geometria das dobras.

# Acknowledgments

I would like to take this opportunity to express my gratitude to data M Sheet Metal Solutions GmbH., and especially Dipl.-Ing. Albert Sedlmaier for the opportunity to develop this master thesis in the company's facilities in Munich, Germany, and for the fruitful experience even in pandemic times.

I must thank my supervisor at FEUP, Prof. Dr. Abel Santos, for all the guidance since the beginning of the project and the encouragement and advice given during my studies at Faculdade de Engenharia da Universidade do Porto.

I would like to thank my supervisor at data M, Dr. Thomas Dietl, for all the support and strategical guidance throughout the project, and for the insightful and direct feedback important to make me aware and focused on the goals of the project. To M.Sc. Miguel Pereira for all the mentorship and help even before the project officially started. The daily contact and the fruitful discussions with M.Sc. Miguel Pereira were key to my motivation and to the development of the project's content. To ir. André Abee and Dipl.-Ing Johann Harrasser for the valuable feedback on the models, the constructive criticism towards the results, and the knowledgeable insights on the fields of roll forming and numerical simulation. Finally, to Benedikt Kohl, Felix Randl, Mattias Wimmer, and Viviane Bauer for the friendship and companionship.

Last, but not least, I must thank my family for always staying by my side and backing my decisions. I owe them all of my future success. Thank you.

*"Be strong and courageous.*
*Do not fear or be in dread of them,*
*for it is the Lord your God who goes with you.*
*He will not leave you or forsake you."*

Deuteronomy 31:6

# Contents


**1 Introduction** **1**
- 1.1 data M Sheet Metal Solutions GmbH . . . 1
- 1.2 Current challenges . . . 2
- 1.3 Scientific approach . . . 3
- 1.4 Dissertation structure . . . 3

**2 Field of investigation** **5**
- 2.1 Roll forming . . . 5
  - 2.1.1 Sheet behavior during the roll forming process . . . 8
  - 2.1.2 Common defects . . . 11
- 2.2 Finite element analysis in sheet metal forming . . . 14

**3 Project requirements** **17**

**4 State of art** **21**
- 4.1 Available roll forming simulation tools . . . 21
- 4.2 Marc/Mentat element library . . . 22
  - 4.2.1 Solid - Element 7 . . . 22
  - 4.2.2 Thick shell - Element 75 . . . 23
  - 4.2.3 Thick shell with reduced integration - Element 140 . . . 24
  - 4.2.4 Thin shell - Element 139 . . . 25
  - 4.2.5 Solid shell - Element 185 . . . 25
- 4.3 Finite element analysis of roll forming . . . 27
  - 4.3.1 Relevant parameters and comparison criteria . . . 27
  - 4.3.2 Previous studies . . . 28

**5 Behavioral element tests** **31**
- 5.1 Compression with double-sided contact test . . . 32
- 5.2 Uniaxial tensile test . . . 36
- 5.3 Tensile test . . . 39
- 5.4 Edge contact test . . . 41
- 5.5 Single element bending moment test . . . 43
- 5.6 Air bending test . . . 46
- 5.7 Conclusions . . . 53

**6 Roll forming tests** **55**
- 6.1 Model definition . . . 55
  - 6.1.1 Geometry and flower . . . 55
  - 6.1.2 Geometry modeling . . . 58

6.1.3 Mesh definition . . . 58
6.1.4 Material model . . . 59
6.1.5 Boundary conditions . . . 60
6.1.6 Contact definition . . . 63
6.2 Results and discussion . . . 63
6.2.1 Double-sided contact . . . 65
6.2.2 Lateral edge contact . . . 70
6.2.3 In-plane shear stress . . . 72
6.2.4 Bending angles and springback . . . 75
6.2.5 End flare . . . 77
6.2.6 Total Equivalent Plastic Strain . . . 81
6.2.7 Edge wave . . . 83
6.2.8 Thickness . . . 89
6.2.9 Computation time . . . 91
6.2.10 Discussion of the results . . . 92

**7 Conclusions** **97**
7.1 Future work . . . 98

**References** **101**

# List of Figures


1.1 Graphic interface of the software COPRA® RF, used to design roll forming processes . . . 1
1.2 Graphic interface of the FEA software COPRA® FEA RF . . . 2

2.1 Roll forming line where an undeformed sheet is turned into a finished profile. Each station, comprised of two or more rolls, gradually changes the profile cross-section [Halmos (2006)] . . . 6
2.2 Impact of the number of passes on the final product [Halmos (2006)] . . . 6
2.3 Flower pattern obtained using COPRA® RF . . . 7
2.4 Design process of a roll forming line [Ferreira (2016)] . . . 7
2.5 Transverse bending of the metal sheet during the roll forming process [Halmos (2006)] . . . 8
2.6 Edge travel schematic representation during the roll forming process [Halmos (2006)] . . . 9
2.7 Redundant transverse tensions that may appear during roll forming [Halmos (2006)] 9
2.8 Longitudinal bending phenomenon in roll forming [Halmos (2006)] . . . 10
2.9 Rotary grooving of a sheet [Halmos (2006)] . . . 11
2.10 Springback of a sheet [Benson (2018)] . . . 11
2.11 Bow and twist deffects in roll forming [Halmos (2006)] . . . 12
2.12 Impact of guided rolls on the longitudinal strain [Halmos (2006)] . . . 13
2.13 Flare of cut-off ends [Halmos (2006)] . . . 13
2.14 Visual representation of a mesh with elements and nodes . . . 14
2.15 Von Mises stress countour-bands for a roll forming model . . . 14
2.16 Visual representation of a eight-noded solid element with 8 integration points [MARC (2021b)] . . . 16
2.17 Visual representation of a shell element [MARC (2021b)] . . . 16

4.1 Visual representation of element 7 [MARC (2021b)] . . . 23
4.2 Visual representation of element 75 [MARC (2021b)] . . . 23
4.3 Recommended integration order for a two dimensional element [Bathe (2014)] . 24
4.4 Visual representation of element 140 [MARC (2021b)] . . . 25
4.5 Visual representation of element 139 [MARC (2021b)] . . . 25
4.6 Visual representation of element 185 [MARC (2021b)] . . . 26

5.1 Single element specimen, with dimensions in mm. The coloured axes represent the normal coordinate system; the black axes on the right represent the global coordinate system. . . . 31
5.2 Model of the compression with double-sided contact test for the shell elements . 32

5.3 Model of the compression with double-sided contact test for the solid and solid shell elements . . . 33
5.4 Stretched solid element after compression, with dimensions in mm . . . 33
5.5 Plot of the Y Force on top contact surface for the solid and solid shell elements . . . 34
5.6 Stress-Strain curve of the compression test for the solid and solid shell elements . . . 34
5.7 Top view of stretched element (bottom surface on the background in red) with corresponding nodal rotation quantities [rad]. 10× scale factor for X and Z displacements . . . 35
5.8 Model of the uniaxial tensile test for the shell elements . . . 37
5.9 Model of the uniaxial tensile test for the solid and solid shell elements . . . 37
5.10 Stretched solid element after the uniaxial tensile test . . . 38
5.11 Model of the tensile test for the shell elements . . . 39
5.12 Model of the tensile test for the solid and solid shell elements . . . 39
5.13 Stretched elements after the tensile test . . . 40
5.14 Model of the edge contact test for the shell elements . . . 41
5.15 Model of the edge contact test for the solid and solid shell elements . . . 42
5.16 Deformed solid element after the edge contact test . . . 43
5.17 Model of the bending moment test for the shell elements . . . 43
5.18 Model of the bending moment test for the solid and solid shell elements . . . 44
5.19 Deformed elements after the bending moment test . . . 44
5.20 Air bending test models . . . 47
5.21 Boundary conditions of the air bending test for the solid and solid shell elements 48
5.22 Distance tolerance (D) and bias factor (B) [Gu (2021)] . . . 49
5.23 Representation of a sharp bend. The material was stamped in the middle of the bend, leading to a thickness reduction [Benson (2015b)]. . . . 50
5.24 Sharp bend phenomenon for the model with solid elements and die width of 10mm. There is a local thickness reduction in the bend line . . . 50
5.25 Shifting of the neutral axis towards the inside radius [Benson (2018)] . . . 51

6.1 Cross-section of the C-shaped profile . . . 56
6.2 Isometric view of the C-shaped profile . . . 56
6.3 Flower diagram with the forming sequence of the C-Profile, and the expected cross-section in each station; . . . 56
6.4 Global coordinate system of the roll forming simulation. $x$ axis is red; $y$ axis is green; $z$ axis is blue . . . 57
6.5 Local coordinate system of solid elements in the beginning of a roll forming simulation. Direction 1 direction is red; direction 2 is magenta; direction 3 is blue . . . 57
6.6 Mesh refining tab in COPRA2FEA . . . 58
6.7 Preview of the mesh . . . 59
6.8 $x$-direction boundary condition . . . 60
6.9 $y$-direction boundary condition . . . 61
6.10 $z$-direction boundary condition . . . 61
6.11 Additional boundary condition for the cut-off . . . 62
6.12 x-direction boundary condition for the models with shell elements . . . 63
6.13 Isometric view of the first stations for the roll forming model with induced double-sided contact . . . 65
6.14 Cross-section view of the sheet in Station 3 evidencing a roll gap of 1.987$mm$, which is 0.013$mm$ smaller than the sheet thickness of 2.000$mm$ . . . 65

6.15 Output of Contact Touched Body via coloured symbols in Station 3 (roll gap smaller than sheet thickness). Nodes in blue are in contact with the top roll; nodes in red are in contact with the bottom roll. . . . . 66
6.16 Forces on the top rolls for the first four stations. In Station 1 and Station 4 double-sided contact does not occur; in Station 2 and Station 3 double-sided contact occurs 67
6.17 Position of the roll plane in relation to the nodes in contact for the model with solid elements in Station 3 . . . . . 68
6.18 Expected profile cross-section in Station 3, where the values of thickness reduction were taken . . . . . 69
6.19 Profile and rolls in Station 11. Profile in black, top roll in blue, bottom roll in red 70
6.20 Situation of edge contact on a shell element in station 11. Contour bands highlight the nodes in contact . . . . . 71
6.21 Situation of edge contact on a shell element. Vectors indicate the contact forces in each node . . . . . 71
6.22 Isometric view of the in-plane shear in the model with 4 layers of solid elements. Sheet is in contact with rolls in 3 stations: Station 2, Station 3 and Station 4 . . . 72
6.23 Station 3 top view of the in-plane shear in the model with 4 layers of solid elements. Results presented in a deformed mesh . . . . . 73
6.24 In-plane shear on the top layer of the sheet for the different models in Station 3. Results presented in a undeformed mesh . . . . . 74
6.25 C-Profile cross-section indicating measured angles $\alpha$ and $\beta$ . . . . . 75
6.26 Auxiliary lines for angle measurement . . . . . 75
6.27 Angle measurement in the last station . . . . . 75
6.28 Angle measurement after cut-off . . . . . 75
6.29 Flower diagram with the forming sequence of the C-Profile. $\alpha$ is formed until station 5, and is over bent between stations 10 and 13. $\beta$ is formed from station 6 until the end of the roll forming line. . . . . 77
6.30 Locations where the angles were measured in order to calculate end flare . . . . . 78
6.31 End flare values [°] for $\alpha$ and $\beta$ angles, at the tail and lead of the profile . . . . . 78
6.32 Row of nodes and corresponding local coordinates considered for Figure 6.33 and Figure 6.34 . . . . . 79
6.33 In-plane shear stress distribution before cut-off. Black and red lines signalize the center of $\alpha$ and $\beta$ bends . . . . . 80
6.34 Longitudinal stress distribution before cut-off. Black and red lines signalize the center of $\alpha$ and $\beta$ bends . . . . . 80
6.35 Sheet in the last increment before cut-off . . . . . 81
6.36 Cross-section view of the Total Equivalent Plastic Strain [-] for the model with four layers of solid elements . . . . . 81
6.37 Cross-section view of the Total Equivalent Plastic Strain [-] for the model with one layer of solid elements . . . . . 82
6.38 Cross-section view of the model with four layers of solid elements, signalizing the locations where the values of Total Equivalent Plastic Strain were collected for Table 6.8 . . . . . 82
6.39 Cross-section of the profile indicating the row of nodes where the longitudinal strain was measured. . . . . 84
6.40 History of the longitudinal strain for a row of nodes in the bottom layer of the sheet edge, in the model with 4 layer of solid elements . . . . . 84

6.41 Longitudinal strain in station 2 for the model with 4 layers of solid element. The sheet undergoes longitudinal bending when entering the rolls . . . . . 85
6.42 Row of nodes in the bottom layer where the longitudinal strain was collected . . 85
6.43 History of average value of longitudinal strain for the top and bottom layers of the sheet edge . . . . . 87
6.44 Top layer longitudinal strain in station 2 for the model with thick shell elements with 7 integration layers. The sheet undergoes longitudinal bending when entering the rolls and accumulates compressive strain in the top layer . . . . . 88
6.45 Sheet in the last increment before cut-off . . . . . 89
6.46 Cross-section view of the thickness of the elements . . . . . 90
6.47 CPU time for the different models in minutes . . . . . 92
6.48 Visual representation of a eight-noded solid element with 8 integration points [MARC (2021b)] . . . . . 94

# List of Tables


4.1 Summary of each element type . . . . . 26

5.1 Uniaxial tensile test results: Z Displacement for the nodes not locked in the Z direction; stresses in the local coordinates and von Mises stresses (which, for one model, are the same for all the nodes) . . . . . 38
5.2 Tensile test results: element thickness for both sides; Z displacement and $\tau_{12}$ for Node 1 (Figure 5.13) . . . . . 40
5.3 Edge contact tensile test results . . . . . 42
5.4 Results of the single element bending test: Displacement Y in Node 1 for the shells and average value between Node 1 and Node 3 for the solid and solid shell; von Mises $\sigma$, $\tau_{12}$, and $\tau_{23}$ for the bottom layer of Node 2 for the shells and in Node 2 for the solid and solid shell . . . . . 45
5.5 Air bending test results for a die width of 10mm before springback . . . . . 49
5.6 Springback and punch force results for a die width of 10mm . . . . . 51
5.7 Springback and punch force results for a die width of 100mm . . . . . 52
5.8 Summary of conclusions for the behavioral tests . . . . . 54

6.1 Mechanical properties of DP600 . . . . . 60
6.2 Swift Law constants for the DP600 . . . . . 60
6.3 Parameters analyzed during the study of the numerical simulation of a roll forming process . . . . . 64
6.4 Peak value of the forces on the top roll [$kN$]. Station 1 and Station 4 have a roll gap bigger than the sheet thickness; Station 2 and Station 3 have a roll gap smaller than the sheet thickness, which induces double-sided contact . . . . . 68
6.5 Thickness reduction [$mm$] of the sheet on Zone A (Figure 6.18). Results collected for increment 390 in Station 3, which has double-sided contact. . . . . 69
6.6 Computation time for the simulation of the models with and without double-sided contact . . . . . 69
6.7 Results of the measured angles $\alpha$ and $\beta$, for the different models with different element types. Springback calculated using the difference between the angles after cut-off and in the last station. Model with 4 layers of solid elements used as reference . . . . . 76
6.8 Values of Total Equivalent Plastic Strain [-] for the top, middle and bottom layers in the center of the two bends $\alpha$ and $\beta$, as seen in Figure 6.38 . . . . . 83
6.9 Peak values of longitudinal strain and corresponding critical station . . . . . 86
6.10 Results for the computation time of each model . . . . . 91
6.11 Summary of the results of the roll forming numerical simulation . . . . . 93

# Abbreviations and symbols

| | |
|---|---|
| ALE | Arbitrary Lagrangian Eulerian |
| CPU Time | Computation Time |
| FEA | Finite Element Analysis |
| FEM | Finite Element Method |
| $\varepsilon_i$ | Normal strain in the direction $i$ |
| $\sigma_i$ | Normal stress in the direction $i$ |
| $\gamma_{ij}$ | Shear strain in the plane $ij$ |
| $\tau_{ij}$ | Shear stress in the plane $ij$ |

# Chapter 1

# Introduction

The project and work that lead to the development of this dissertation were conducted in data M Sheet Metal Solutions GmbH, Munich, Germany, during a four-and-a-half-month internship. In this chapter, the company is presented, as well as the current challenges that motivated this project, its goals, the scientific approach used in the research, and the structure of this dissertation.

## 1.1 data M Sheet Metal Solutions GmbH

data M Sheet Metal Solutions GmbH (data M) is a company based in Oberlaindern, 40km to the south of Munich, in Germany, founded in 1987. data M is specialized in the field of sheet metal processing and has been developing and distributing the world's leading software solutions for roll forming COPRA® RF and COPRA® FEA RF, and for metal bending COPRA® MetalBender. COPRA® RF (Figure 1.1) works as an add-in integrated into AutoCAD, which supports the design process of tools and stations for roll forming lines. COPRA® FEA RF (Figure 1.2) was developed using the software MSC Marc/Mentat and is used to simulate the roll forming operation by nonlinear elastoplastic calculation, using finite element analysis (FEA) [data M Sheet Metal Solutions GmbH (2021)].

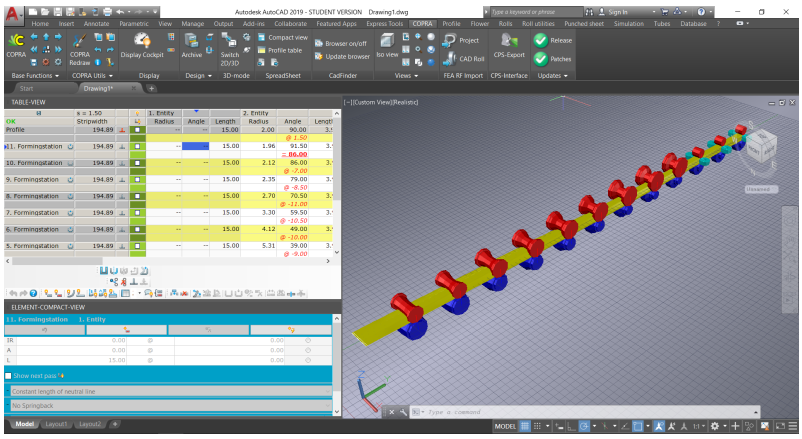


Figure 1.1: Graphic interface of the software COPRA® RF, used to design roll forming processes

Moreover, data M provides not only software solutions but also consulting and engineering services, including design activities, analysis of forming processes or customized research and development in the field of roll forming.

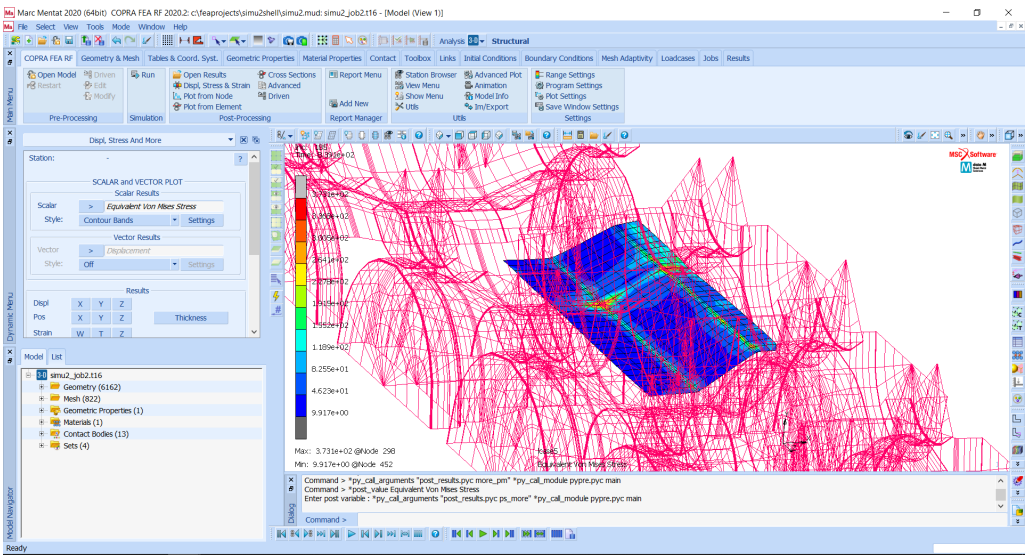


Figure 1.2: Graphic interface of the FEA software COPRA® FEA RF

## 1.2 Current challenges

Roll forming is a sheet metal bending process that obtains a profile with a desired cross-section by gradually bending a strip of metal over several stations. As a highly productive manufacturing process that allows to obtain a wide variety of cross-sections, roll forming has applications in a vast array of industries.

COPRA® FEA RF simulates the roll forming process using eight-node isoparametric solid elements. By default, only one solid element through the thickness is used, aided by an enhanced assumed strain formulation to improve the bending behavior of the elements. The results obtained through these models are considered reliable and efficient.

The simulation time is of utmost importance as it has a direct impact on productivity. This is even more relevant considering COPRA® FEA RF is usually used in an industrial context, where time and efficiency play an important role.

Thus, research has been conducted in the field of FEA in order to continuously improve the performance of numerical models even further. From these studies, several findings arise, such as different element types, improvements to element formulations, and other simulation parameters, which are gradually introduced to Marc/Mentat, the software package that powers the COPRA® FEA RF simulations.

Therefore, the present dissertation aimed to fulfill the need for efficient model parameters that yield even faster results, without compromising the reliability of the results, the possibility of correctly detecting and preventing defects in the final product, and the ability to predict the behavior

of the sheet during the process. These objectives were achieved by assessing the usage of alternative element formulations in the finite element analysis of roll forming, namely shell elements, and assessing the possibility of coupling different element types. By the end of the project, an alternative to the COPRA® FEA RF default model was expected to be achieved, together with the conditions in which this alternative model is suitable to be used.

## 1.3 Scientific approach

The present work was divided into three main stages. Firstly, the theory of roll forming and its main deformation mode, bending, was studied in order to understand basic concepts and to know what to analyze when conducting numerical simulations. Secondly, the available elements in the Marc/Mentat library were studied. This was done not only by understanding the theory behind their formulation but also by subjecting them to simple standard tests which allow analyzing the behavior of the elements and their strengths and limitations. Lastly, based on the conclusions of the more simple tests, roll forming models were created and the results analyzed, in order to successfully achieve a suitable alternative to the solid elements in the simulation of roll forming.

## 1.4 Dissertation structure

The present dissertation is divided into seven chapters and is structured as follows:

- **Chapter 2 - Field of investigation** provides a general introduction to the roll forming and to finite element analysis, the two core topics of the present dissertation. On the topic of roll forming, the process is presented, together with the main forming modes involved and with the most common defects. On the topic of finite element analysis, some basic concepts are reviewed with a focus on sheet bending numerical problems.

- **Chapter 3 - Project requirements** lists the requirements that the present work strives to fulfill, in order to define a vision for the project and to create a framework to objectively evaluate the final results of the dissertation.

- **Chapter 4 - State of art** conducts a review of existing studies on the numerical simulation of roll forming and the already existing tools, which are also evaluated in the light of the defined project requirements. The element types used during this work are also introduced.

- **Chapter 5 - Behavioral element tests** covers six different tests in order to understand the behavior of the different element types when subjected to basic loads, reflecting the forming mechanisms studied in Chapter 2. Preliminary conclusions are drawn regarding the strengths and limitations of each element type.

- **Chapter 6 - Roll forming tests** presents the results for the different element types when used to simulate a roll forming process, and validates conclusions drawn in Chapter 5.

- **Chapter 7 - Conclusions** summarizes the conclusions drawn throughout the work, assesses the project, and proposes an outlook of possible future work and research.

# Chapter 2

# Field of investigation

This chapter presents the field of investigation, together with the introduction of some relevant theoretical concepts. Section 2.1 introduces the roll forming process, which is the core of the current project, as all the results are intended to be applied to the finite element analysis of roll forming. The sheet behavior and the common defects are covered in order to better understand relevant process parameters and criteria to take into consideration during the simulations. The forming mechanisms are studied and will be the basis for the creation of relevant behavioral tests. Lastly, a brief introduction to finite element analysis is given.

## 2.1 Roll forming

Roll forming is a manufacturing forming process used to obtain profiles of a desired shape through permanent plastic deformation of a sheet [Lundh (1997)]. This deformation is obtained as the sheet successively passes through a series of contoured rolls, gradually changing its shape along straight, longitudinal, parallel bend lines, allowing to obtain relatively complex geometries [Halmos (2006)]. The friction involved in the contact between the sheet and the rotating rolls is responsible for the longitudinal movement of the sheet. The rotation speed of the rolls is adjusted in order to obtain a constant flow of the material, which can range from as low as 1m/min to 200m/min [Groche and Müller (2013)]. As a pure forming process that applies bending instead of compression, the thickness of the sheet is preserved except at the bend lines where it is normally reduced [Halmos (2006)] [Groover (2010)].

Apart from the complexity of the cross-sections, another main advantage of roll forming is the ability to apply tight bending radii without crack formation [Lundh (1997)]. Figure 2.1 illustrates a roll forming line, where a sheet is gradually bent in each station (also referred to as pass) in order to obtain the final cross-section. Additionally, a roll forming line can also incorporate secondary operations, such as punching, cutting, flanging and welding, avoiding additional space, labor and inventory costs [Halmos (2006)].

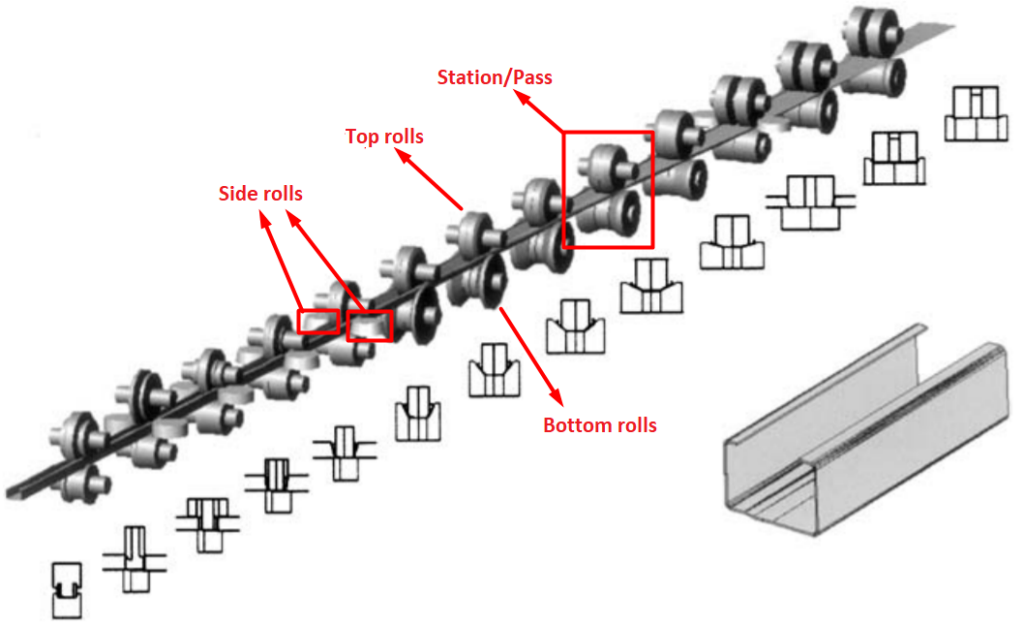



Figure 2.1: Roll forming line where an undeformed sheet is turned into a finished profile. Each station, comprised of two or more rolls, gradually changes the profile cross-section [Halmos (2006)]

A wide variety of materials can be subjected to roll forming, from metals to composites and multi-materials. Yield strength, tensile strength, and elongation are the most important mechanical properties in order to guarantee good results, and the design of the roll forming line must take these material properties into consideration. Steels and aluminum alloys are the most commonly formed materials [Halmos (2006)] [Lindgren et al. (2009)].

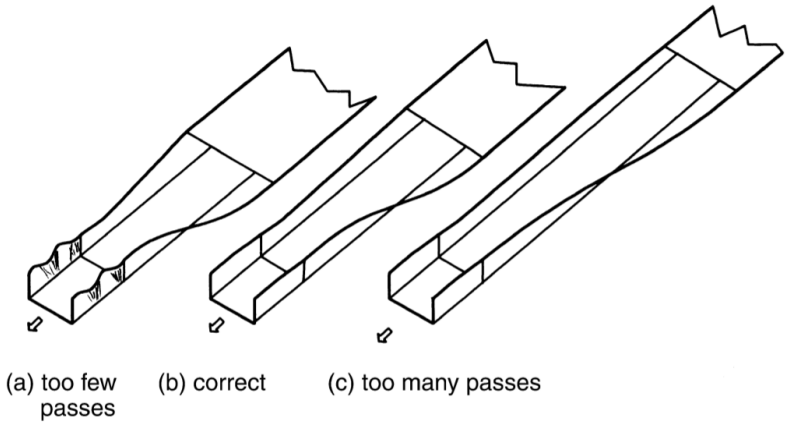



Figure 2.2: Impact of the number of passes on the final product [Halmos (2006)]

The design of a roll forming line is an iterative process that goes through several stages. The main aim during the design of the process, of the rolls and of the profile, is to obtain a good compromise between the quality of the finished product and the costs associated with its production. The first stage of the roll forming design process consists in defining the orientation of the part and how the profile will exit the line. The product orientation will dictate the tool design and

the positioning of the rolls, and influence other additional operations such as punching and welding. Secondly, the designer decides the number of passes for each bend. In general, the fewer the passes, the smaller the cost of the machine and rolls, but higher the likelihood of producing a product with defects associated with the high stresses resulting from the harsh bending [Halmos (2006)], as it can be observed in Figure 2.2.

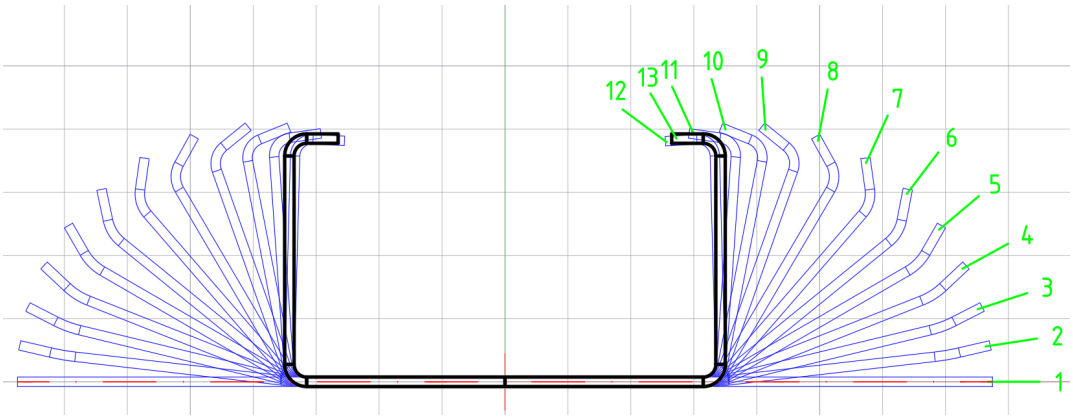



Figure 2.3: Flower pattern obtained using COPRA® RF

After planing the bends and the flow of the material, the flower pattern (Figure 2.3) containing the section drawing of each successive pass is created, allowing for a quick and good visual understanding of the bending sequence.

The next stage consists of validating the designed roll forming line, usually by means of Finite Element Analysis (FEA). With the aid of FEA, engineers can better understand the behavior of the sheet during the process and analyze each station and the final product. Thus, the design of the roll forming line can be optimized before starting the production of the tools, which saves both time and money [Martins (2018)]. Figure 2.4 summarizes the different stages of the design process of a roll forming line.

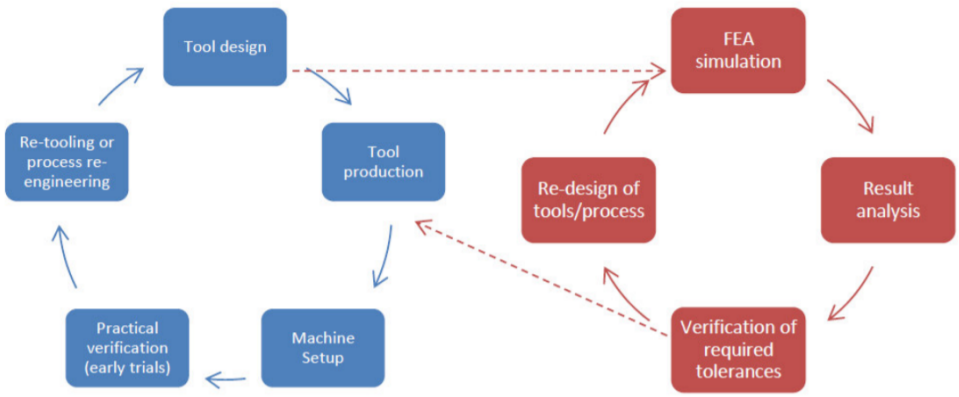



Figure 2.4: Design process of a roll forming line [Ferreira (2016)]

### 2.1.1 Sheet behavior during the roll forming process

In theory, the roll forming process normally tends to be simplified to a pure bending process [Marciniak et al. (2002)]. However, in the real world, different types of deformations are involved in the whole process, which will have an impact on the final product. The different forming mechanisms involved in roll forming are mentioned below in this subsection.

#### 2.1.1.1 Transverse bending

Most sheet forming processes apply bending along a straight line; in the case of roll forming, the desired shape is obtained mainly due to progressive transverse bending, applied using a series of contoured rolls. This applied bending is the main responsible for achieving each different cross-section [Marciniak et al. (2002)], as can be seen in Figure 2.5.

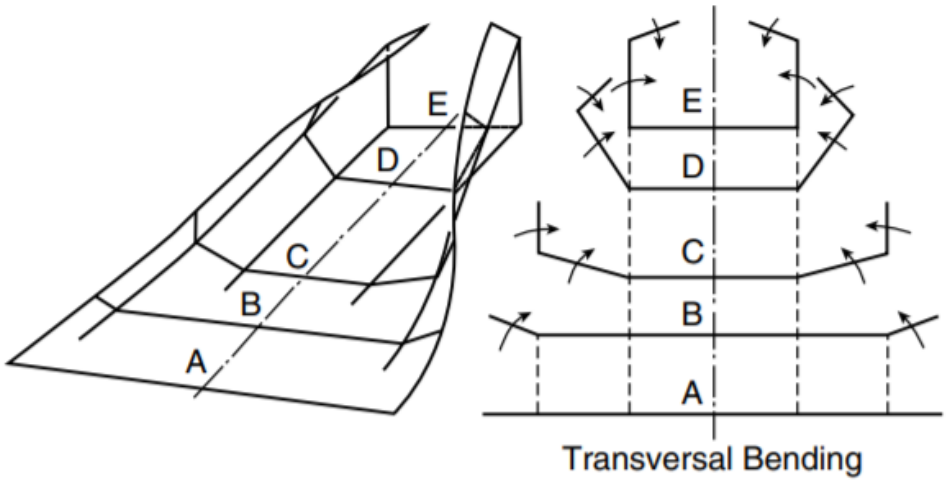



Figure 2.5: Transverse bending of the metal sheet during the roll forming process [Halmos (2006)]

#### 2.1.1.2 Longitudinal deformation

The roll forming process continuously bends the metal sheet along successive passes, which translates into different cross-sections along the length of the sheet. This difference in depth or width of the cross-sections, will impact the flow of the edges and thus induce longitudinal strains.

Take into consideration the Figure 2.6, the length of the bend line from A to B is $l$, whereas the length $s$ of the edge between C and D will be:

$$s = \sqrt{c^2 + l^2} \tag{2.1}$$

with $c$ corresponding to the length of the arc between F and D. As both the pairs A/C, and B/D, are in the same cross-section, the increased length of the edge C-D results in an elongation, inducing a longitudinal strain [Halmos (2006)].

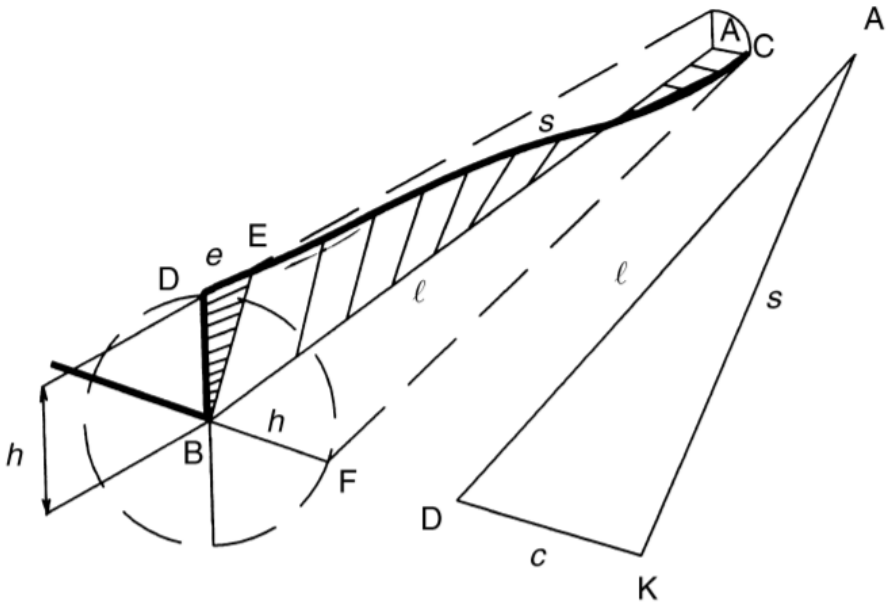



Figure 2.6: Edge travel schematic representation during the roll forming process [Halmos (2006)]

#### 2.1.1.3 Transverse deformation

When working with wide sheets, and mainly when the material enters the line in the form of a coil and not as a precut sheet, stronger forces are required in order to shift the material near the edge of the sheet towards the center. Due to this applied force, and to the width reduction of the cross-section that occurs between two stations, in-plane shear strain and width strain are induced in the edge and intermediate portions of the strip [Halmos (2006)].

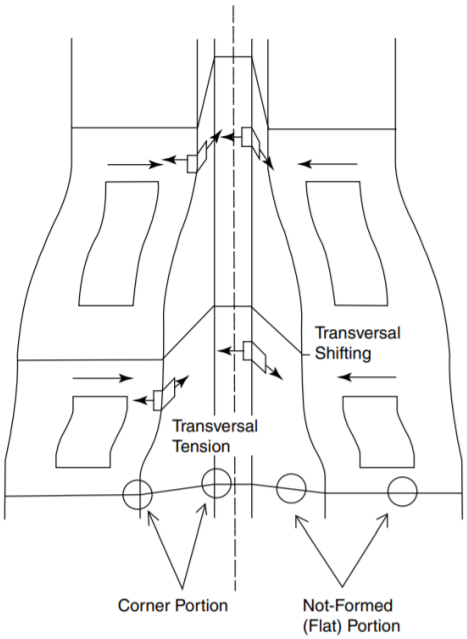



Figure 2.7: Redundant transverse tensions that may appear during roll forming [Halmos (2006)]

Furthermore, in some cases, if the sheet surface is pulled against the roll with a significantly intense force, it can result in a compressive mode being applied in the direction of the thickness, slightly reducing the thickness and inducing additional redundant transverse tensions, which can be visualized in Figure 2.7. This phenomenon is most predominant on the bend lines, areas of intense contact between the rolls and the sheet, and which are further away from the center of the sheet [Halmos (2006)].

#### 2.1.1.4 Longitudinal bending

The metal sheet enters the roll gap along several flow lines. These flow lines might have different inclinations, due to the concave and convex shapes of the rolls, which will induce a longitudinal bending, as can be observed in Figure 2.8. Due to the nature of this bending mechanism, and to the fact that both the radius of this bend and the length of the sheet are significantly bigger than the sheet thickness, a plane assumption can be considered. Therefore, positive longitudinal strains and negative thickness strains are prone to appear, which may result in the thinning of the sheet [Wang et al. (2015)]. According to Halmos (2006), this phenomenon is most prominent on the edge portions of the strip.

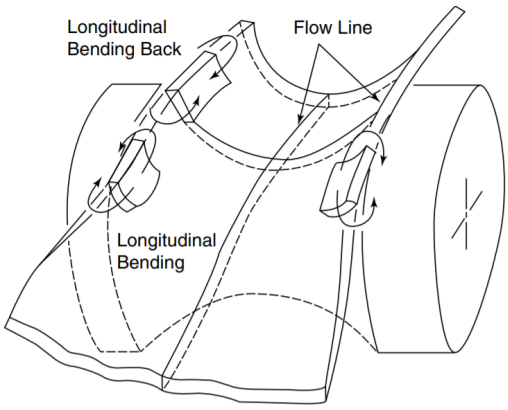



Figure 2.8: Longitudinal bending phenomenon in roll forming [Halmos (2006)]

#### 2.1.1.5 Through-thickness compression

When working with tight roll gaps close to the sheet thickness, some compression in the thickness direction can be induced in the metal strip. As stated by Li et al. (2011), this compression results from the sheet contacting with both the top and bottom rolls. The through-thickness compression is amplified in case the sheet undergoes additional processes that can be integrated into the roll forming line, such as coining and grooving [Halmos (2006)], processes in which the thickness of the sheet is locally reduced, as seen in Figure 2.9.

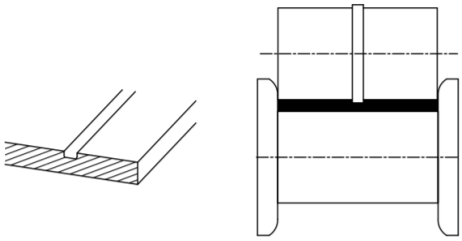


Figure 2.9: Rotary grooving of a sheet [Halmos (2006)]

#### 2.1.1.6 Springback

As stated by Halmos (2006), springback occurs when the material angularity returns towards its initial shape after a bending . It is a phenomenon common in most of the metal forming processes, and roll forming is no exception. When bending the sheet, the material will change its permanent shape by entering the plastic domain, but an elastic recovery of the material occurs after the bending moments are released. The magnitude of the elastic recovery will depend on the material properties, mainly on the yield stress and on the Young's modulus. Furthermore, wider and thicker sheets are also more prone to bigger sprinback angles. Figure 2.10 shows how springback can influence the bend angle. To compensate for the effects of springback, the sheet is usually over bent and, ideally, the desired bending angles are achieved after the elastic recovery [Wang et al. (2017)].

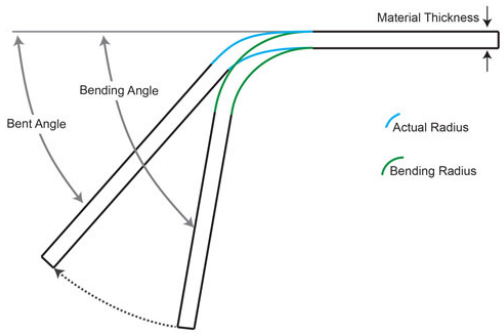



Figure 2.10: Springback of a sheet [Benson (2018)]

### 2.1.2 Common defects

As mentioned in Section 2.1.1, transverse bending is the most important forming mechanism in order to form the desired cross-section. The other mentioned forming mechanisms are a secondary result of the process, are normally mentioned as redundant forming mechanisms, and cause a variety of defects in the final product [Halmos (2006)]. Due to potential losses through product rejection, it is important to study common defects and which process parameters influence them, to better predict material behavior and adjust roll settings, minimizing defects [Weiss et al. (2009)]. The most common roll forming defects are mentioned in this subsection.

#### 2.1.2.1 Bow and twist

Longitudinal bow and twist are caused by a nonuniform transverse distribution of the longitudinal membrane strain and are the most common defects in narrow roll formed products, leading to an anticlastic curvature along the final profile, as seen in Figure 2.11 [Safari and Joudaki (2018)].

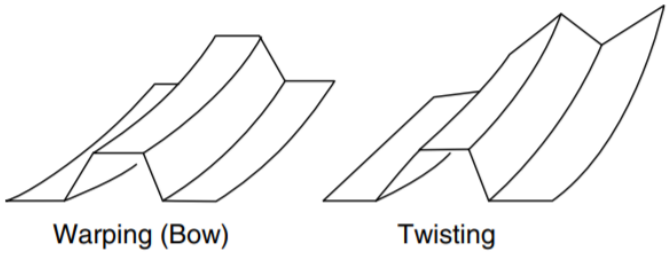



Figure 2.11: Bow and twist deffects in roll forming [Halmos (2006)]

The nonuniformity in the transverse distribution of the longitudinal strain is inevitable, especially when the metal strip is roll-formed into a product with a cross-section having height and width significantly different from the initial of a flat metal strip [Halmos (2006)]. However, it can be reduced. These defects are more prone to appear for harsher bending angles, and thus increasing the number of passes might be a solution to tackle this problem by reducing the overall magnitude of the longitudinal strains. Moreover, entry guides and intermediate guides, allied with a correct alignment and positioning of the rolls, help to stabilize the sheet minimizing the height and width variations and consequently reducing longitudinal strains [Sajjad et al. (2020)] [Halmos (2006)].

#### 2.1.2.2 Waviness (edge wave)

The edge wave is another common roll forming defect and is caused by elastoplastic buckling. Buckling occurs when there is an excessively large longitudinal membrane strain, which tends to appear in the edge portion of the sheet.

Longitudinal strain in the edge portion of the sheet is inevitable, *"because the edge portion has to move both in the vertical and transverse directions"* [Halmos (2006)]. The edge portion shrinks in the gaps between the rolls, but this shrinkage can occur smoothly with the use of guide rolls, reducing the magnitude of the longitudinal strain (Figure 2.12). Furthermore, there are other solutions for waviness such as local heating. The impact of this solution could also be studied by FEA. However, it requires a thermal-mechanical coupling analysis that considers the stress-strain field and an additional temperature field, and thus, the simulations would have a longer computation time [Gao et al. (2013)].

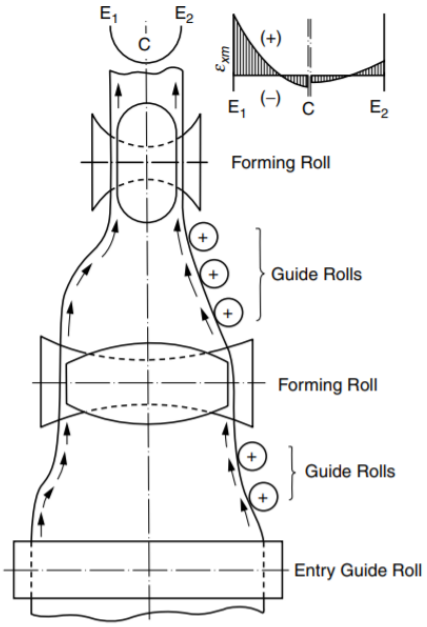



Figure 2.12: Impact of guided rolls on the longitudinal strain [Halmos (2006)]

#### 2.1.2.3 End flare

As previously mentioned, the forming of the metal sheet induces residual stresses, which are then released during the cutting process, causing the profile ends at the cut-off to undergo additional deformation [Halmos (2006)]. The effect on the angles of the bends can be seen in Figure 2.13.

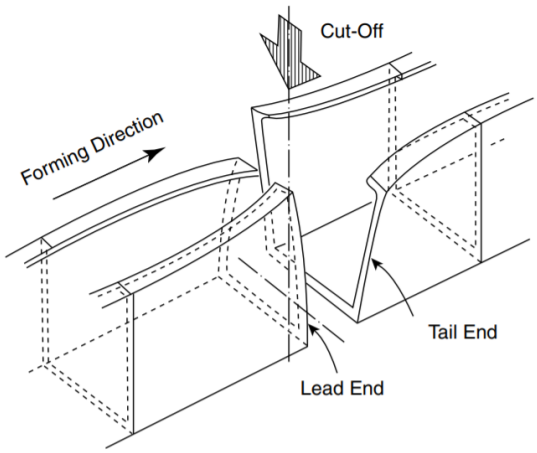



Figure 2.13: Flare of cut-off ends [Halmos (2006)]

The residual stresses most commonly associated with end flare are the in-plane shear stress and the longitudinal stress [Moneke and Groche (2018)]. As a counter-measure for end flare, the profile can be over bent and bent back in the last stations of the roll forming line, inducing residual stresses in the opposite direction of the already existing ones and reducing the overall magnitude of

the residual stresses [Jimma and Ona (1981)]. Furthermore, it has also been found that additional pressure can be applied in the flanges by reducing the roll gap, in order to reduce the residual shear stresses at the cost of slightly increasing the longitudinal strains [Moneke and Groche (2018)].

## 2.2 Finite element analysis in sheet metal forming

The finite element method is a numerical method used to solve physical problems in engineering analysis and design, and can be applied in several areas of interest conducting different types of analysis, such as structural, heat transfer, fluid flow, mass transport, among others. There are problems that, due to their complexity and size, are difficult to convert to equations in order to be analytically solved. Thus, the finite element method converts the problem of an entire body into multiple problems of interconnected smaller bodies, solving systems of simultaneous algebraic equations instead of differential equations [Logan (2007)] [Bathe (2014)]. These smaller bodies are referred to as elements, and the points that connect each of them and where the results of the algebraic equations are visualized are referred to as nodes (Figure 2.14). Through numerical extrapolation, the results can be visualized with the use of contour bands, making it easier to analyze results and detect the critical parts of products or components (Figure 2.15).

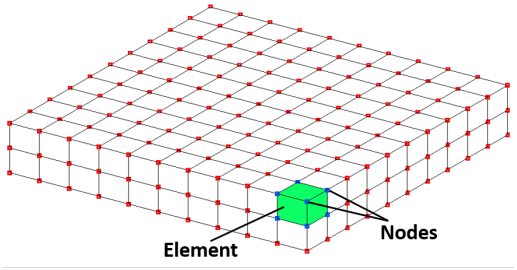



Figure 2.14: Visual representation of a mesh with elements and nodes

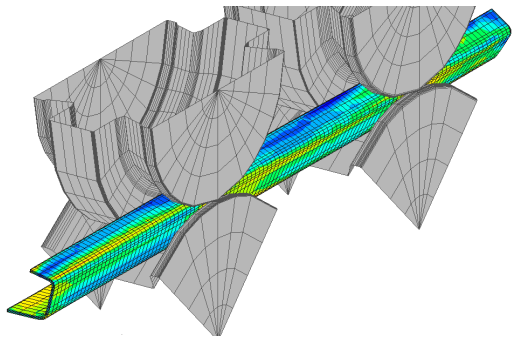


Figure 2.15: Von Mises stress countour-bands for a roll forming model

The most important traits when validating and evaluating a finite element model are reliability and effectiveness. A model is reliable if the physical phenomenona represent real-life behavior

and if the results are within the desired level of accuracy. A model is effective when it can produce results with the desired accuracy in the shortest processing time possible [Bathe (2014)].

The solution for metal forming problems normally resides around displacements, rotations, stresses, and strains. However, the created mathematical model is tailored to one's needs and thus, in the prediction of the physical phenomenon, no more information can be expected than the information contained in the mathematical model, which underlies the importance of the choice of the most appropriate mathematical model [Bathe (2014)].

During the present work, simulations will be conducted using the displacement-based method, which has the principle of virtual work (or principle of virtual displacements) as a core for its formulation [Bucalem and Bathe (2011)].

*"If a deformable body in equilibrium is subjected to arbitrary virtual (imaginary) displacements associated with a compatible deformation of the body, the virtual work of external forces on the body is equal to the virtual strain energy of the internal stresses."* [Logan (2007)]

For an arbitrary virtual displacement to be considered compatible, it must satisfy boundary and continuity conditions. These will include strain-displacement relations, stress-strain relations, and force balance [Vlassak (2011)]. The principle of virtual work can be rewritten as:

$$F = KU \tag{2.2}$$

where:

- K is the stiffness matrix of a structure
- U is a vector of the system's global displacements
- F is a vector of the applied forces

The principle of virtual work is valid for static problems [Logan (2007)]. All simulations in the present work are conducted with an implicit solver, and that the roll forming process is considered a quasi-static problem [Bathe (2014)].

Furthermore, linear and nonlinear analysis can be conducted. For linear problems, the stiffness matrix does not depend on the displacement and force vectors. However, contact and friction, which are relevant for roll forming, are usually a source of nonlinearities. Moreover, when plasticity is considered, the stresses and strains behave nonlinearly in the plastic domain [MARC (2021a)]. Therefore, a nonlinear approach should be considered during the roll forming simulations, in order to represent the elastoplastic behavior of the sheet.

Considering the existence of nonlinearities, in order to improve the accuracy of the values of the stress and strain fields, the results in the nodes can be calculated by extrapolating the results from the integration points of each element [Bathe (2014)]. This is known as the Gaussian-integration method. The number and location of the integration points will depend on the element, but an example can be visualized in Figure 2.16.

There are several types of elements and different formulations, which can vary in terms of number of nodes, number of integration points, number of nodal degrees of freedom, interpolation

methods, among others [MARC (2021b)]. For the analysis of three-dimensional problems, the different elements can fall into two major categories: solid elements and shell elements.

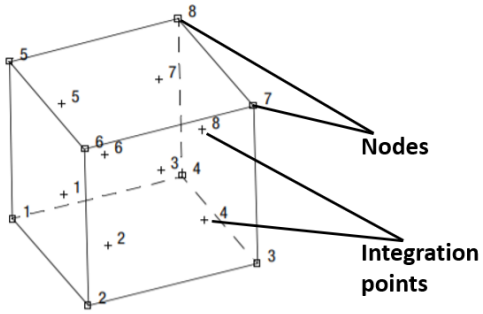



Figure 2.16: Visual representation of a eight-noded solid element with 8 integration points [MARC (2021b)]

Solid elements are three-dimensional volume elements whose cross-section and thickness can vary [Dassault Systèmes Simulia Corp (2011)]. Solid elements can have several different shapes such as a tetrahedron, a pentahedron, or a hexahedron. The most commonly used solid elements are the hexahedral elements, also referred to as bricks, such as the one seen in Figure 2.16. The main disadvantage of solid elements is the prominence to locking under bending loads, in other words, to present an over stiffing behavior. By analyzing Equation 2.2, with an over stiffing behavior to a certain load the element is resistant to displacements. Locking can be avoided by using several layers of elements through the thickness, which increases the computational costs [Xia and Tang (1999)] [Autodesk (2018)].

Shell elements are generally used to model structures in which one of the dimensions is significantly smaller than the other two dimensions. The smallest dimension will be in the thickness direction of the element. The geometry of the body is represented at a reference surface, as seen in Figure 2.17, and its thickness is numerically defined as a nodal property or as an element property [Dassault Systèmes Simulia Corp (2011)]. Shell elements can be used as an alternative to reduce computational costs. It is not recommended to use shell elements when the structure is subjected to out-of-plane loads. The main disadvantage of shell elements lies in its use being limited to thin structures and in the non-three-dimensional visualization of the results [DIANA FEA (2017)].

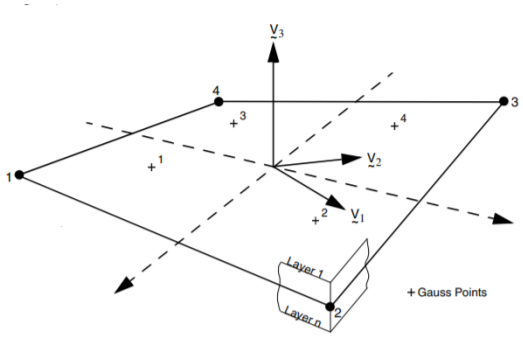



Figure 2.17: Visual representation of a shell element [MARC (2021b)]

# Chapter 3

# Project requirements

Chapter 2 reviewed the field of the investigation of the present work, where some current challenges and opportunities in the field of numerical simulation of roll forming were analyzed. The project requirements were based on the knowledge from the field of investigation, and their aim is to clearly and objectively define the goals of the dissertation. These goals served as guidelines for monitoring the progress of the project and will be used to objectively assess the work in the end.

Firstly, the basic requirements for the entire project were drawn. In order for this project to be deemed successful, the following requirements must be met:

- To analyze alternatives to the already used 8-node isoparametric solid element (Element 7 from the Marc/Mentat library).
  - New element formulations have already been developed, such as shells and solid shells. This is an opportunity to improve the performance of numerical models by taking the most out of each different element. Therefore, the theory behind their formulation should be studied in order to already gain some insights into their expected behavior.
- To conduct standard behavior tests.
  - Due to the different element formulations, each element has its own strengths and limitations. Thus, the elements will be subjected to simple tests in order to obtain preliminary results before the roll forming simulations.
- To create roll forming models using alternative elements and to draw conclusions on the behavior of the different element types.
  - Based on the preliminary results from the simple element tests, the different elements should be tested in the roll forming context.
- To draw conclusions regarding the impact on the results of different model parameters.

  - Apart from using different elements, different results are also expected to be obtained when using different model parameters, such as in the definition of contact, or the number of integration layers.

The previously listed requirements are the minimum and mandatory requirements for a successful project. The present work also aims to meet the following complementary requirements:

- To find a viable alternative to the standard solid element model.
  - The hexahedral solid element has been the element of choice for COPRA® FEA RF models, yielding accurate results for most of the roll forming scenarios. However, the literature which will be presented in Subsection 4.3.2 shows evidence that there might be some alternative elements capable of yielding more efficient results.
- To assess coupling of different element types in the same model.
  - Based on the strengths and limitations of each element, coupling different element types in the same model can be a way of taking the most out of each element. Different elements could be used for different areas of the metal strip.
- List criterion and guidelines on when to use each element type.
  - In case one or more elements serve as viable alternatives to the solid element, guidelines for when to use these elements should be created. This is relevant as it is likely that the formulations of some of the elements may be advantageous for certain situations. Ideally, in case these guidelines can be expressed objectively and numerically, they could even be directly implemented in the meshing function of COPRA® FEA RF.

One of the requirements is that *"a viable alternative to the standard solid element model is found"*. In order for a model to be considered as a viable alternative to the standard solid element model, the following requirements must be met:

- The model converges.
  - The model needs to yield results for all the stations and for the cut-off at the end of the roll forming line.
- Faster simulations, with a shorter CPU time, are obtained.
  - As the focus of this work is on improving the efficiency of the roll forming models, computation time is of utmost importance.
- The final profile geometry is correctly represented.

  - The geometry of the final product is one of the most relevant results to be taken from a roll forming simulation. Therefore, the geometry of the final product, namely the angles of the bends on the cross-section, must be accurately represented by the alternative model.

- Defects and imperfections can be identified.

  - Some defects mentioned in Section 2.1.2 can be predicted by the numerical simulation of roll forming. Some specific stresses and strains must be accurately represented so that satisfactory conclusions can be drawn from the numerical models.

# Chapter 4

# State of art

This chapter presents a brief review of previous studies on the topic of roll forming and numerical simulation. Section 4.1 focuses on the currently available tools for roll forming simulation. Section 4.2 presents the framework of Marc/Mentat and the elements from its library which will be used in the numerical simulations. Lastly, Section 4.3.2 contains a review of previous studies on finite element analysis of roll forming, highlighting the literature gaps on which this project focuses.

## 4.1 Available roll forming simulation tools

There are several software packages that allow to conduct a finite element analysis of the roll forming process:

- ABAQUS and Ansys are examples of commercially available software packages suitable for finite element analysis, each with its own library, and can be used to create several different models and to simulate a wide range of processes.
- PROFIL is a roll forming design software. It allows to design the roll forming line and to export the model to be simulated in LS-DYNA. It uses both models with shell elements or with multiple layers of solid elements [UBECO GmbH (2021)].
- Metafor is a software package that, unlike the others in this list that use a classical Lagrangian formulation to analyze the flow of the material, uses the Arbitrary Lagrangian Eulerian (ALE) formulation to obtain the stationary solution of the roll forming process [Boman et al. (2005)]. The ALE formulation tries to solve some issues associated with the classical Lagrangian formulation, such as avoiding fatal issues when a pre-cut sheet has to enter each roll station or reducing computational costs by using less refined meshes in the areas between the stations [Crutzen et al. (2016)]. However, CPU time saving could not yet be achieved over the Lagrangian formulation, as the ALE formulation needs to simulate a sheet with a length bigger than the entire roll forming line length, whereas the classical Lagrange can simulate significantly smaller sheet lengths.

- COPRA® FEA RF is powered by Marc. The roll forming line is designed in COPRA® RF and the FEA model is automatically created using COPRA2FEA. What distinguishes COPRA's models is not only the simplicity in designing the roll forming line and in easily creating the numerical model, but also the good performance of the numerical models. It must be highlighted the especially good results that are obtained when using models with just one solid element through the thickness and the reliability of the numerical simulation of contact and friction in Marc.

The main problem common among all the available tools is the performance of their models and the time they take to create the model and fully simulate it, assuring a minimum accuracy of the results. Among all these available tools, this project will focus on the COPRA® FEA RF software package and on the elements in the Marc/Mentat library.

## 4.2 Marc/Mentat element library

This section presents the elements used during the simulations. There are currently 247 elements in the Marc element library, and thus it was necessary to select a smaller number of element types since it would be unrealistic to analyze and test all the existing elements.

For this purpose, the standard element used by COPRA® FEA RF, which is an eight-noded solid element, had to be studied. Shell elements were also selected based on literature evidence that these elements might improve the performance of roll forming models [Lindgren (2005)]. Reduced integration elements were also considered due to their computer efficiency [Li et al. (2011)]. Due to the hexahedral (cubic) shape of the standard solid element, all the selected elements are based on quadratic surfaces: the shell elements have four nodes, and the solid shell element also has a hexahedral shape.

### 4.2.1 Solid - Element 7

Element 7 consists of an eight-noded, isoparametric, three-dimensional brick element with trilinear interpolation, as seen in Figure 4.1. Its nodes have three degrees of freedom, which are the displacements, and the nodes do not account for rotations. As for the output variables, the element outputs six stresses and six strains - three normal and three shears [MARC (2021b)].

This is the standard element used by COPRA® FEA RF for the simulations, with only one element through the thickness being already enough to provide accurate results, which goes against several claims made in previous literature researches [Hellborg (2007)]. Due to the trilinear interpolation method, the strains tend to be constant through the element, and thus there is a nearly constant strain distribution through the element thickness, which is not representative of the reality of the roll forming process. This interpolation method may also yield poorer shear results when compared with an element with triquadratic interpolation, and locking phenomenona can arise [MARC (2021b)]. However, using the solid element with an assumed strain interpolation

to augment the deformation gradient, good results can be obtained with only one solid element through the thickness [Bengzon et al. (2018)].

The stiffness of the element is obtained through eight-point Gaussian integration. There are higher-order solid elements available, which could serve as an alternative to this element. Nonetheless, Element 7 normally performs better in contact analysis situations [MARC (2021b)].

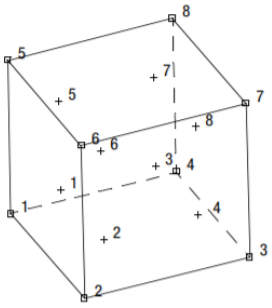



Figure 4.1: Visual representation of element 7 [MARC (2021b)]

### 4.2.2 Thick shell - Element 75

Element 75 consists of a four-noded, thick-shell element with bilinear interpolation. Its nodes have six degrees of freedom - three for the displacements and three for the rotations.

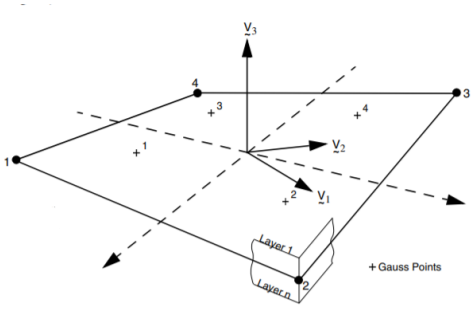



Figure 4.2: Visual representation of element 75 [MARC (2021b)]

Integration through the element thickness is numerically performed using the Simpson's rule. An odd number $(1+2i)$ of integration layers must be used in order to have 1 integration point in the mid surface where the centroid is located, and an additional $2i$ top and bottom layers. Using the Simpson's rule allows the top and bottom layers to be exactly $0.5t$ away from the mid-layer ($t$ corresponds to the element thickness). In other words, the top and bottom layers of the shell are coincident with the surfaces of a solid element of equivalent thickness [Mars et al. (2017)].

Stresses and strains are outputted in a local coordinate system, which by default considers direction 3 to be the thickness direction, as can be seen in Figure 4.2. The element outputs five stresses and five strains - three shear and two normal. The element does not output normal stresses and strains in the thickness direction.

Moreover, the thickness of the element has to be inputted as a geometric property and it can be either uniform through the element or node-based. During the simulation, bilinear thickness variation is allowed in the plane of the element, and the thickness output is stored for each node [MARC (2021b)].

### 4.2.3 Thick shell with reduced integration - Element 140

The element 140 is a variation of element 75 with reduced integration. It is also a four-noded, thick-shell element with bilinear interpolation and its nodes have six degrees of freedom. It outputs five stresses and five strains and does not output the normal stress and strain in the thickness direction. The element can be observed in Figure 4.4

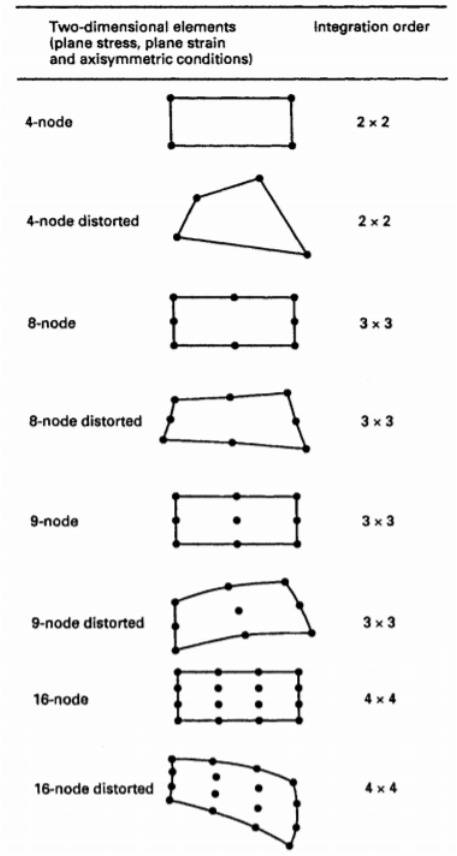



Figure 4.3: Recommended integration order for a two dimensional element [Bathe (2014)]

From the Figure 4.3, it can be verified that the recommended integration order for a 4-node two-dimensional element is 2x2. Considering Element 140 is a shell element, for integrations in the plane normal to the thickness direction a 2x2 group of Gaussian points, or in other words, 4 points would be required for a Full Gaussian integration. In case of a reduced integration, 1x1 integration order is used, in other words, a single Gauss integration point is used [Bathe (2014)]. This formulation allows the element to have a better computer efficiency when compared with

full integration elements, but the element is more prone to hourglassing due to the lower order integration of the stiffness matrix [Abaqus (2021)].

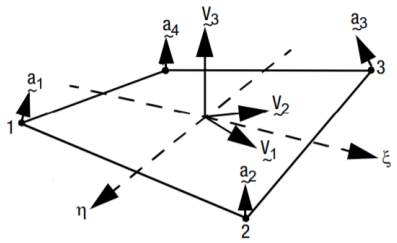



Figure 4.4: Visual representation of element 140 [MARC (2021b)]

### 4.2.4 Thin shell - Element 139

The element 139 is a thin shell variation of the thick shell element 75. It is also a four-noded element with bilinear interpolation and its nodes have six degrees of freedom. However, it only outputs three stresses and three strains, disregarding the normal stress and strain in the thickness direction, and only outputting shear stress and strain on the shell surface. Thus, this element has a pure plane strain behavior [MARC (2021b)]. It is represented in Figure 4.5.

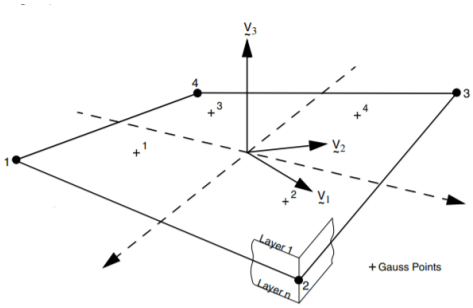



Figure 4.5: Visual representation of element 139 [MARC (2021b)]

The thin shell is usually used in simpler forming situations due to its high efficiency and low computational cost. By not representing the two components of shear in the thickness direction, it is prone to miss represent some thinning effects when under complex forming loads [Gál and Lukacs (2020)].

### 4.2.5 Solid shell - Element 185

Element 185 has some characteristics of both shell elements and solid elements. On the one hand, it has an eight-node brick topology and only has the nodal displacements as degrees of freedom. On the other hand, the element is integrated with multiple integration layers through the thickness but only one point per layer. Similar to what happens with the shell element with reduced integration, element 140, these integration points are always located in the centroid of

the integration layer and the number of integration layers is defined by the user [MARC (2021b)]. Element 185 is represented in Figure 4.6.

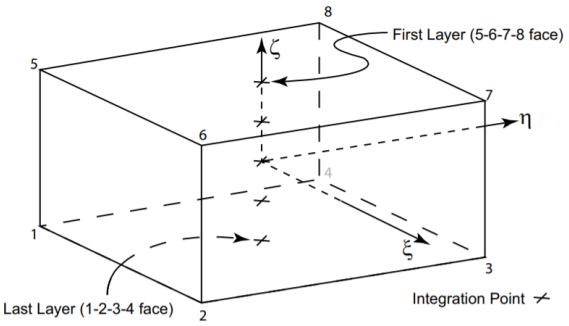



Figure 4.6: Visual representation of element 185 [MARC (2021b)]

The element outputs six stresses and six strains and is thus able to output the shear components using the assumed natural strain formulation and the normal component in the thickness direction using the enhanced assumed strain formulation. The assumed natural strain will reduce the polynomial order of interpolations, whereas the enhanced assumed strain will augment the strain field. These two formulations are often combined to derive efficient and reliable finite elements for continuum displacement-based shell formulations, mainly by solving locking issues [Bischoff and Ramm (1997)].

To sum up, the main characteristics of the five element types that will be further studied and used in the numerical simulations are summarized in Table 4.1.

Table 4.1: Summary of each element type

| | **Nodes** | **Nodal degrees of freedom** | **Through-thickness integration layers** | **Points per integration layer** | **Stress outputs** |
|---|---|---|---|---|---|
| **Solid - 7** | 8 | 3 | 2 | 4 | $\sigma_1, \sigma_2, \sigma_3, \tau_{12}, \tau_{23}, \tau_{31}$ |
| **Thick shell - 75** | 4 | 6 | User-defined | 4 | $\sigma_1, \sigma_2, \tau_{12}, \tau_{23}, \tau_{31}$ |
| **Thin shell - 139** | 4 | 6 | User-defined | 4 | $\sigma_1, \sigma_2, \tau_{12}$ |
| **Shell with reduced integration - 140** | 4 | 6 | User-defined | 1 | $\sigma_1, \sigma_2, \tau_{12}, \tau_{23}, \tau_{31}$ |
| **Solid shell - 185** | 8 | 3 | User-defined | 1 | $\sigma_1, \sigma_2, \sigma_3, \tau_{12}, \tau_{23}, \tau_{31}$ |

## 4.3 Finite element analysis of roll forming

As reported in Section 2.1.1, the sheet behavior in terms of stresses and strains can be quite challenging to predict using only analytical methods, mainly due to nonlinear relations between the applied forces and displacements. The stiffness matrix is not constant during the load application, due to nonlinear effects from geometrical, material, and contact nonlinearities [Plumbridge et al. (2003)]. It becomes even more critical when there is the need to accurately predict behaviors such as springback for complex profiles. The application of finite element methods (FEM) during the design process of roll forming has played an important role when it comes to improving the final product quality, reducing manufacturing costs, and studying the impact of process parameters [Martins (2018)]. Tests can be done using FEM software packages such as COPRA® FEA RF to validate designs and assumptions before actually setting up a physical roll forming line. However, even though data M strives to develop intuitive and user-friendly software packages, in order to simplify the creation of numerical models, roll forming knowledge and experience is indispensable to interpret simulation results and to detect problems even before they appear in real life [Ferreira (2016)].

Section 4.3.1 presents the relevant study parameters, which are important to conduct a meaningful analysis of the results of a roll forming numerical simulation. Section 4.3.2 contains a review of some of the existent literature in the field of numerical simulation of roll forming.

### 4.3.1 Relevant parameters and comparison criteria

There are several results that are obtained from the simulation of roll forming, in order to avoid product defects like the ones mentioned in Section 2.1.2.

As previously mentioned, springback plays a very important role in roll forming and must be accurately represented by the simulation [Zhang et al. (2016)]. It is usually studied by analyzing the bending angles before and after the elastic recovery of the material, making sure the desired bending angle is achieved, but it can also be studied by analyzing the final section width and height. The angles in the lead and tail of the profile after cut-off should also be analyzed to understand the magnitude of end flare resulting from the release of residual stresses [Moneke and Groche (2018)].

Some thickness reduction is also prone to occur in the bend lines, especially when conducting bends with small bending radii [Marciniak et al. (2002)]. Therefore, the minimum thickness in each bend must also be analyzed.

In order to control unwanted deformations and to better understand elastic recovery, the Equivalent von Mises stresses and Equivalent Strains can also be studied. These values of stresses and strains are a great tool to easily identify problems in the profile, as they depend on the stresses and strains from all the principal directions.

Equivalent von Mises stress ($\sigma_{VM}$) can be calculated as [Mises (1913)]:

$$\sigma_{VM} = \sqrt{\frac{1}{2}[(\sigma_1 - \sigma_2)^2 + (\sigma_2 - \sigma_3)^2 + (\sigma_3 - \sigma_1)^2] + 3(\tau_{12}^2 + \tau_{23}^2 + \tau_{31}^2)} \tag{4.1}$$

where:

- $\sigma_i$ corresponds to the normal stress in the direction $i$;
- $\tau_{ij}$ corresponds to the shear stress in the plane $ij$.

Equivalent strain ($\varepsilon_{eq}$) derives from Equation 4.1 and can be calculated as:

$$\varepsilon_{eq} = \frac{1}{\sqrt{2}(1+\nu')}\sqrt{[(\varepsilon_1-\varepsilon_2)^2+(\varepsilon_2-\varepsilon_3)^2+(\varepsilon_3-\varepsilon_1)^2+\frac{3}{2}(\gamma_{12}^2+\gamma_{23}^2+\gamma_{31}^2)]} \tag{4.2}$$

where:

- $\nu'$ corresponds to the effective Poisson's ratio;
- $\varepsilon_i$ corresponds to the normal strain in the direction $i$;
- $\gamma_{ij}$ corresponds to the shear strain in the plane $ij$.

To easily check when the plastic domain is achieved, the Equivalent Plastic strain can also be analyzed, which only considers the strains that occur in the plastic domain. If the value of the Equivalent Plastic strain is bigger than 0, the material plastified. The Total Equivalent Plastic Strain shows the cumulative value of Equivalent Plastic Strain and is the parameter that will be analyzed in the roll forming simulations.

Transverse stresses, longitudinal and transverse strains, and in-plane shear stresses can also be individually analyzed due to their direct link to some of the product defects.

Lastly, it is important to consider the roll loads, which will be calculated by analyzing the induced force on the contact surfaces of the rolls. These forces must be considered as they will be fundamental for an optimal design of the roll stands and smooth forming of the strip [Bhattacharyya et al. (1987)].

### 4.3.2 Previous studies

Research has been conducted in the field of finite element analysis of roll forming and different types of approaches and simulation models have already been studied.

Senanayake et al. (1994) successfully used the thick shell element 75 from the MARC/Mentat library, with 7 integration points, to study the strain distribution.

Heislitz et al. (1996) simulated a roll forming process using the explicit code PAM-STAMP. Friction was not considered. Both eight-node brick elements and four-node shell elements were compared. Four node shell elements managed to provided faster simulations; however, strains in the local longitudinal and lateral directions were not available on the PAM-STAMP package. Moreover, mesh refinement proved to be crucial to optimize simulation times when using shell elements.

Lindgren (2005) also used the thick shell element 75 from the MARC/Mentat library, with 3 integration points through the thickness, to study which process parameters influence peak membrane strain and the deformation length on the forming of a U-Channel profile. Friction was

considered. The results from the simulations agreed well with existing knowledge on the process. The simulation time was considered "acceptable for research but still too long for industrial use".

Hellborg (2007) optimized simulation models and their mesh, using the implicit and explicit methods, for the four-noded shell element with reduced integration (S4R) and the eight-node hexahedral brick element with reduced integration (C3D8R) from the ABAQUS library. Results regarding strain and springback accuracy were taken for the explicit method, but no solid and converging results were obtained for the implicit method.

Li et al. (2007) benchmarked solid shell elements in comparison to solid elements using an explicit solver.

Yan et al. (2015) achieved accurate springback and bend angle results using continuum and conventional shell elements, when comparing simulation results with experimental results.

Han et al. (2019) studied the plastic deformation mechanism on high-strength steel using an eight-node hexahedral brick element with reduced integration from the ABAQUS explicit library (C3D8R).

Most previous research has focused on analyzing the impact of different process parameters on the results of the simulation models. However, to the best of the author's knowledge, no studies have compared the performance of different variants of shell elements, in regards to processing time and results accuracy. In general, all the available solutions lack results in terms of the performance analysis of the numerical models, and most of the studies do not consider the computation time of the simulations.

There is a lack of good results for implicit methods, mainly due to problems with achieving stable results and overcoming converging issues when using software packages different from the COPRA® FEA RF. The standard thick shell and the solid shell have been studied, but, as far as the author knows, there is no research on the potential of using thin shells or shells with reduced integration in a roll forming context.

Product defects and their connection to each forming mode is a topic well covered by literature. Authors like Halmos (2006) covered the mechanical theory of this topic based on empirical results and authors like Moneke and Groche (2018) and Mohd Saffe et al. (2014) validated the results through numerical simulation. This project will add up to the current knowledge by pointing which element types can accurately represent each forming mechanism and each product defect.

To the best of the author's knowledge, there are no studies that combine different types of elements in the same roll forming model, even though shell-to-solid coupling can be used in ABAQUS, Ansys, and Marc/Mentat. As previously mentioned in Chapter 3, element coupling is an opportunity to make the most out of the advantages of each element. This thematic and possibility have not yet been studied, since there are few studies that highlight the strengths and weaknesses of each element in the roll forming context.

To sum up, the main literature gaps that this dissertation strives to fulfill are:

- The performance of different roll forming models;
- The use of new element formulations in roll forming models;

- The strength and weaknesses of each element type in the context of roll forming.

# Chapter 5

# Behavioral element tests

This chapter presents the results of five single element tests that were conducted in order to better understand the behavior and limitations of each different element type. Single element tests are a good way to test different element types, to assure material laws are well defined, and to adjust simulation parameters, assuring that the simulation successfully runs and converges [Barrett (2014)]. Moreover, these models are simpler and easier to model than multi-element models, and even though they might have their own limitations due to the poor discretization, simulating with one element allows to draw preliminary conclusions, before spending time in more complex models.

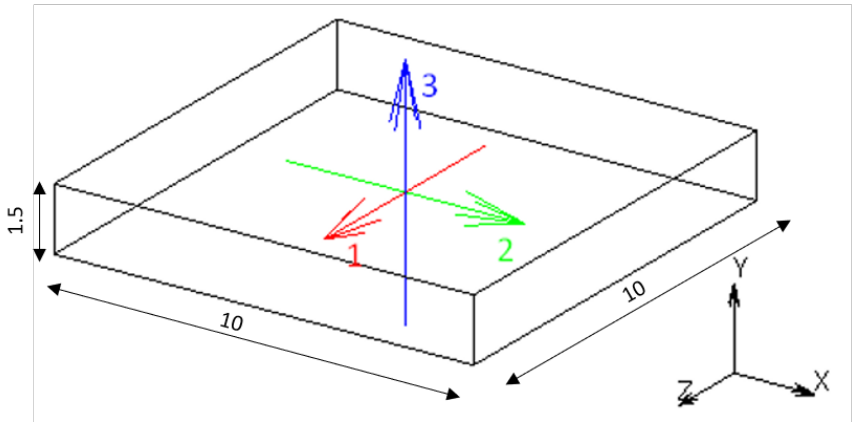



Figure 5.1: Single element specimen, with dimensions in mm. The coloured axes represent the normal coordinate system; the black axes on the right represent the global coordinate system.

The load cases and boundary conditions on the models were inspired in the literature on element formulation and were designed to mimic the different deformation modes involved in roll forming mentioned in Section 2.1.1. For all the single element tests, a single $10 \times 1.5 \times 10mm$ element was simulated. These dimensions were chosen to use an element roughly the size of the elements which are normally used in a roll forming simulation. The local and global coordinate

systems can be seen in Figure 5.1. It is also to mention that for the models with shell elements and with solid shell elements seven integration layers through the thickness were used, as it is at first the value recommended by MARC (2021a) in order to accurately represent bending.

Lastly, Section 5.6 presents the results of a multi-element air bending test, conducted in order to study the behavior of the elements when subjected to the main deformation mode involved in roll forming [Marciniak et al. (2002)].

## 5.1 Compression with double-sided contact test

Depending on the profile that is being formed, some stages of the roll forming process may induce double-sided contact on the sheet when it passes between two rolls [Halmos (2006)], phenomenon covered in Section 2.1.1.5 when mentioning the through-thickness compression the sheet may be subjected to. The double-sided contact is one of the main threats to the use of shell elements, as they are often not appropriate for the simulation of this phenomenon, due to the fact that each node establishes contact with only one body, and partly due to the plane-stress assumptions in their formulation, which consider $\sigma_3 = 0$ [Wang et al. (2017)] [Lia et al. (2010)]. As the shell elements are subjected to a displacement that produces zero strains and zero stresses in the Gaussian integration points, in other words, there are spurious zero-energy modes in the model, models with shell elements can have their mesh irregularly distorted [Abaqus (2021)][LS-DYNA (2021)]. This phenomenon is even more critical for reduced integration elements, as they only use one integration point [Belytschko et al. (1984)].

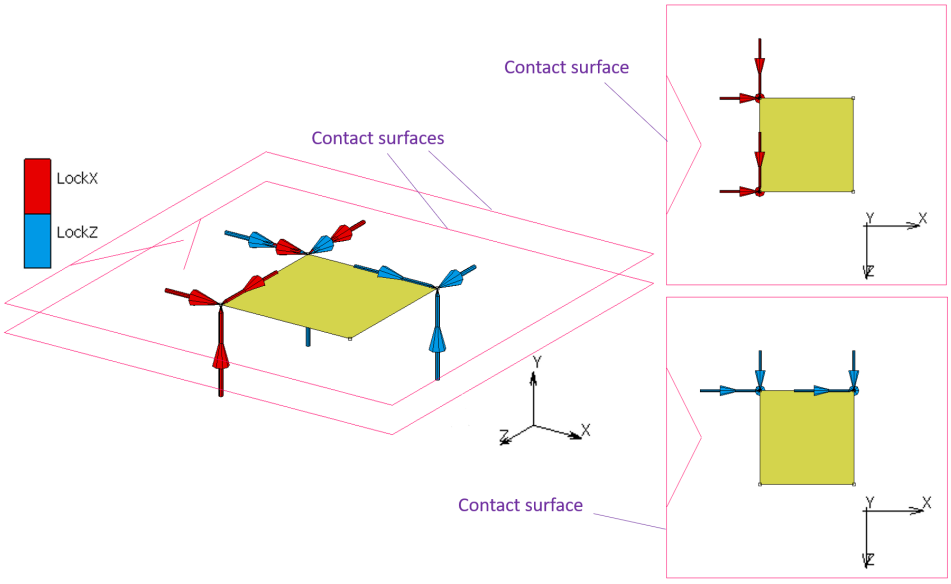



Figure 5.2: Model of the compression with double-sided contact test for the shell elements

In this model, a single $10 \times 1.5 \times 10mm$ element was modeled between two contact surfaces. The bottom surface is fixed and the top surface executes a -1.5mm displacement in the Y direction, at -1mm/s. When the displacement stops, the gap between the top and bottom surface is 0.55mm.

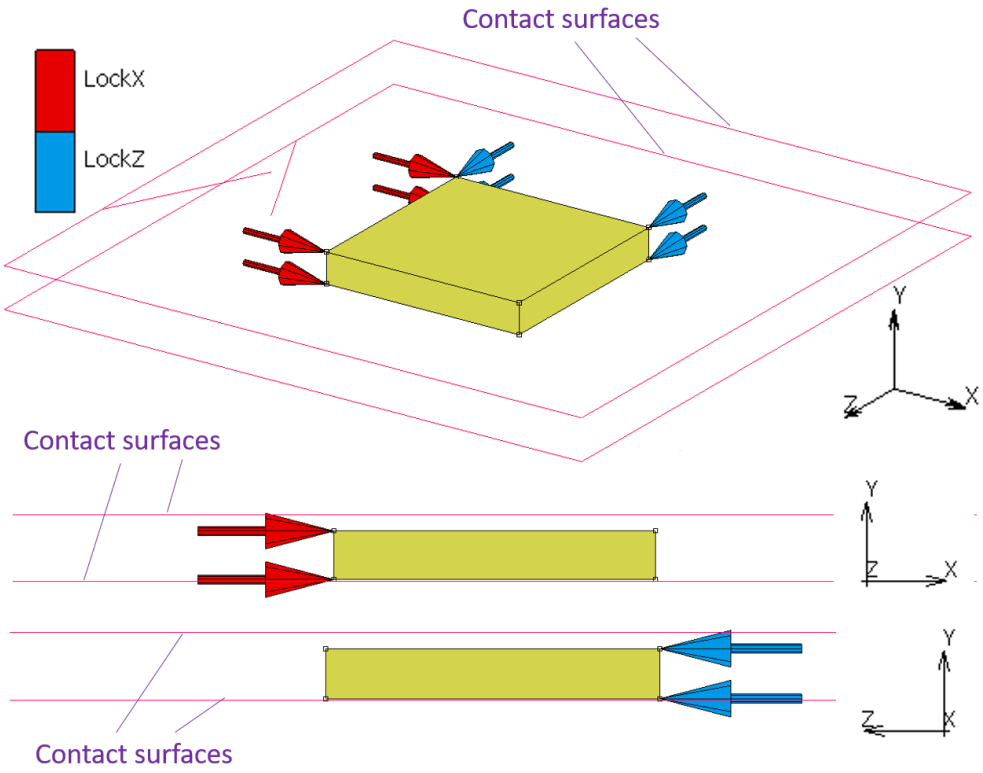



Figure 5.3: Model of the compression with double-sided contact test for the solid and solid shell elements

In order to avoid the sliding and rotation of the element, nodes in the relevant face or edge, for the solid and shell elements respectively, had their displacement restricted in the X and Z directions. Additionally, nodes in the models with shell elements had the relevant rotations related to the mentioned restricted displacements also equaled to 0. The boundary conditions for each model can be observed in Figure 5.2 and Figure 5.3.

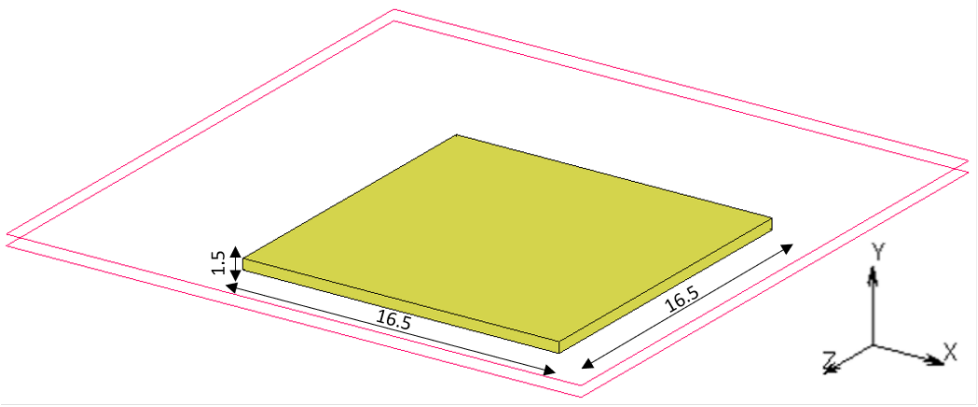



Figure 5.4: Stretched solid element after compression, with dimensions in mm

Analyzing the results of the solid element and of the solid shell element, it can be verified that both elements behave similarly. The thickness of the element is reduced, causing it to stretch in the X and Z directions. The final stretched brick dimensions in both solid and solid shell elements are $16.50 \times 0.55 \times 16.50$mm (Figure 5.4), respecting the conservation of the initial volume, $150\text{mm}^3$.

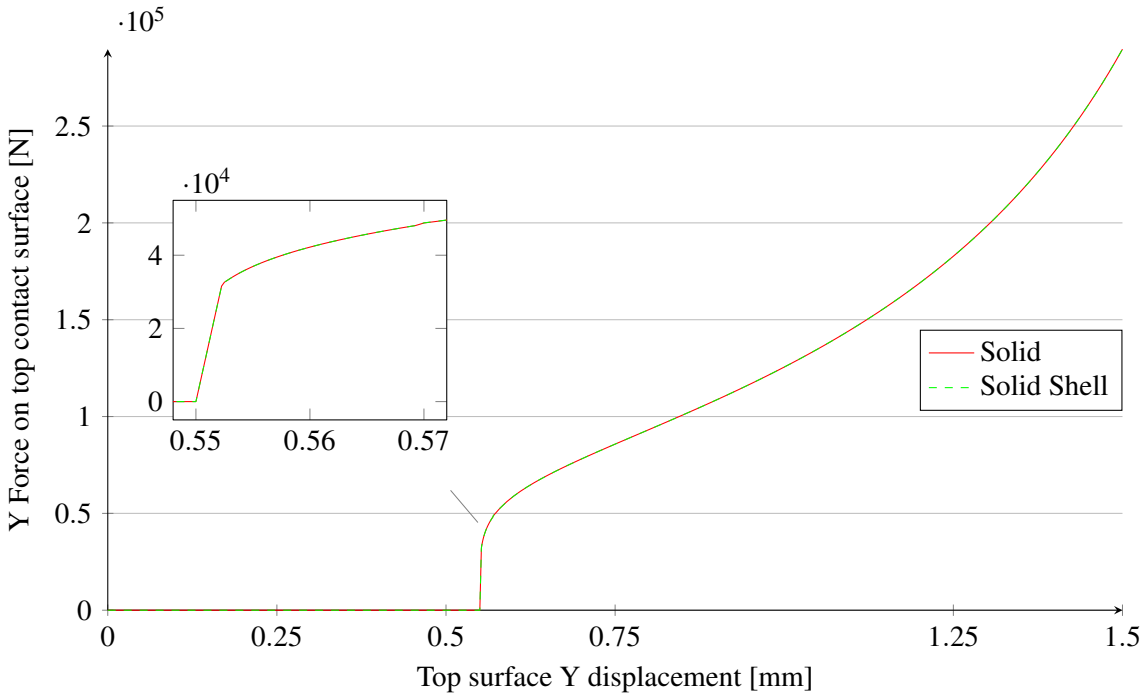



Figure 5.5: Plot of the Y Force on top contact surface for the solid and solid shell elements

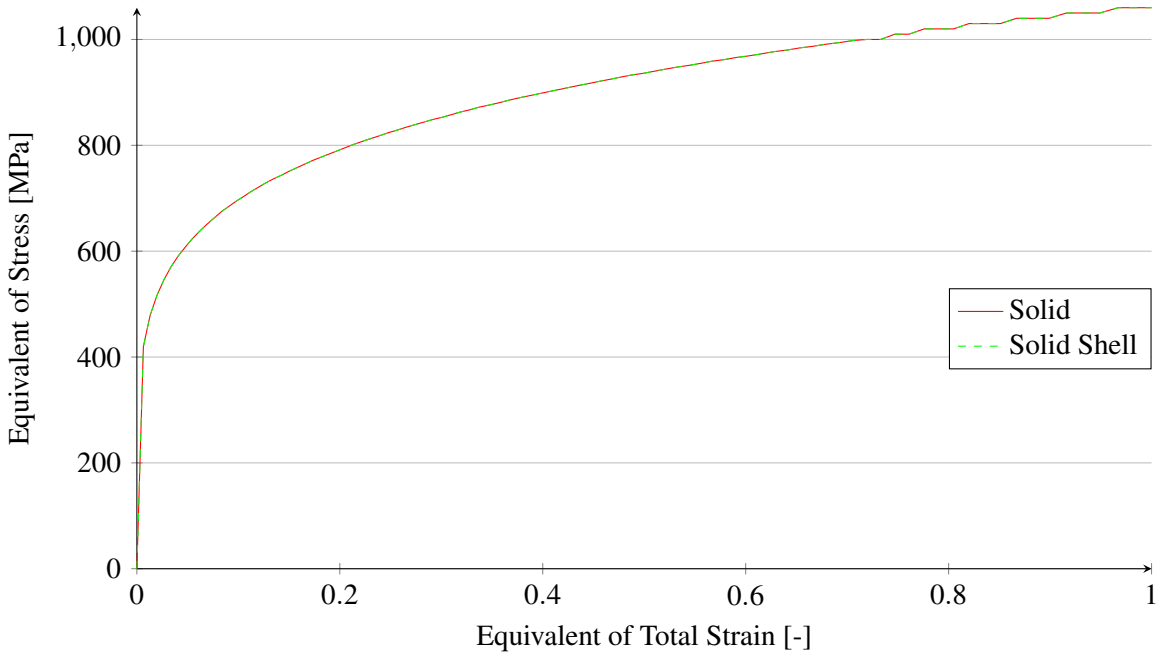


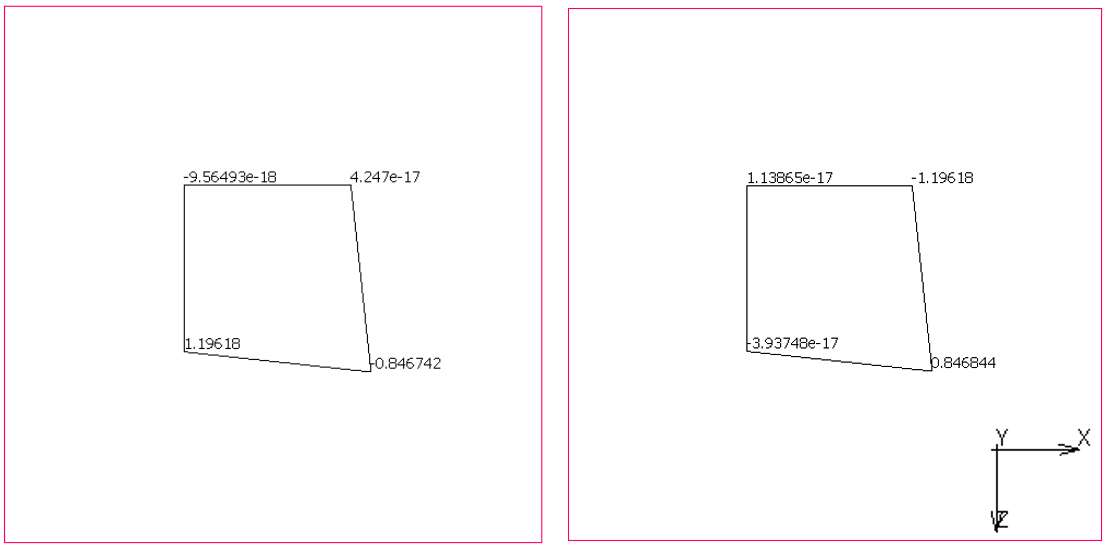

Figure 5.6: Stress-Strain curve of the compression test for the solid and solid shell elements

The reaction forces in the contact surfaces have a value of 289.7$kN$ in the Y direction for the last increment of both mentioned models and grow linearly during the elastic domain (Figure 5.5). Moreover, the stress-strain curves, which can be found in Figure 5.6, are in compliance with the material properties.

The compression of the solid and solid shell elements has high stresses, strains and displacements involved. On the other hand, the shell elements behave completely differently, having a numerically unstable behavior as it could already be expected.

During several simulations with shell elements, two different behaviors were observed.

In some simulations, in each increment, only contact with one surface at a time is established. As there is only a forced displacement in the Y direction, and as no stresses nor strains are calculated in the thickness direction, the stresses and strains in the nodes of the element remain equal to 0. Thus, there are no X and Z displacements for the entire simulation, no variation of the element thickness nodal quantity, and there is a Y displacement that assures the distances from the middle layer of the element to the top and bottom surface are equal. There are no contact forces as nodal quantities. However, forces are induced on the contact surfaces, with an order of magnitude of $10^6 kN$, a value much higher than the one observed for the solid and solid shell elements.




(a) X rotation nodal quantities [rad] (b) Z rotation nodal quantities [rad]

Figure 5.7: Top view of stretched element (bottom surface on the background in red) with corresponding nodal rotation quantities [rad]. 10× scale factor for X and Z displacements

In other simulations, there were nodes establishing contact with the top surface while the other nodes were establishing contact with the bottom surface. This contact state influences the behavior of the element, and by analyzing the displacement and rotational fields, big differences can be seen: there is a distortion of the element, with displacements in X and Z directions, and there are even nodal rotations (Figure 5.7). A first initial visual analysis might indicate an hourglass phenomenon, and after some calculations, the deformations of the element did have an influence on the centroid's position. Nonetheless, there is an appearance of shear stresses $\tau_{12}$ for the outer

integration layers; $\tau_{23}$ and $\tau_{31}$ for the middle layer (in the case of the models with the thick shell and with the shell with reduced integration). Moreover, the area of the element's surface decreases, and the element thickness nodal quantity in the four nodes increases to 1.5038mm. This thickness increase is of a small magnitude order ($10^{-2}mm$), and even though the elements always comply with the conservation of element volume, it is unrealistic for the thickness to increase with this type of load.

The results for the shell elements can be attributed to numerical instability, due to the fact that the exact same model can alternate between the two mentioned behaviors when simulating with different time steps. With a bigger time step, the simulation has fewer increments and the top contact surface is displaced a bigger amount per increment. In this case, there is no apparent logical relation or pattern between the different used time steps and the different results obtained.

To sum up, the solid and the solid shell give good, accurate, and realistic results, indicating these elements behave well in double-sided contact situations. The shell elements, as anticipated, do not provide reliable results and do not accurately represent the effects that the double-sided contact has on the element. Nonetheless, shell elements should not be completely discarded from simulating roll forming with double-sided contact situations, as the models with shell elements still manage to run the simulation and converge, and the von Mises Stress values are not higher than the ones obtained with models with solid and solid shell elements. The contribution of the double-sided contact compression to the roll forming process is small when compared to the contribution of the transverse bending mode, and even though the compressive mode will not be accurately considered, it may not affect or compromise the reliability of the results produced by the other deformation modes, since there was no overestimation of the von Mises stresses. The only result which must be cautiously analyzed is the contact force on the surfaces, in order words, the roll load, as it is expected to be drastically higher when simulating double-sided contact with shell elements.

## 5.2 Uniaxial tensile test

In this test, the elements were submitted to a state of uniaxial stress, allowing for a simple comparison between element formulations. One side of the element has an X displacement of 0, and the opposite side has its nodes gradually submitted to a 10mm displacement. Thus, the length of the element is expected to double by the end of the simulation. The Y displacements are also restricted. Since the thickness of the shell elements can vary, in order to have comparable results only the top nodes are locked in the Y direction in the case of the solid and solid shell elements, also allowing for a variation of the element thickness. This might create some differences in the way that the thickness of the different element types reduces, as having all the top nodes of the solid and solid shell elements locked in a Y direction ends up artificially creating a symmetry in the Y direction. Lastly, there is a lock in the displacements in the Z direction that will mimic symmetry. Additionally, all the relevant rotations are blocked for the shell elements, and the boundary conditions can be observed in Figure 5.8 and Figure 5.9.

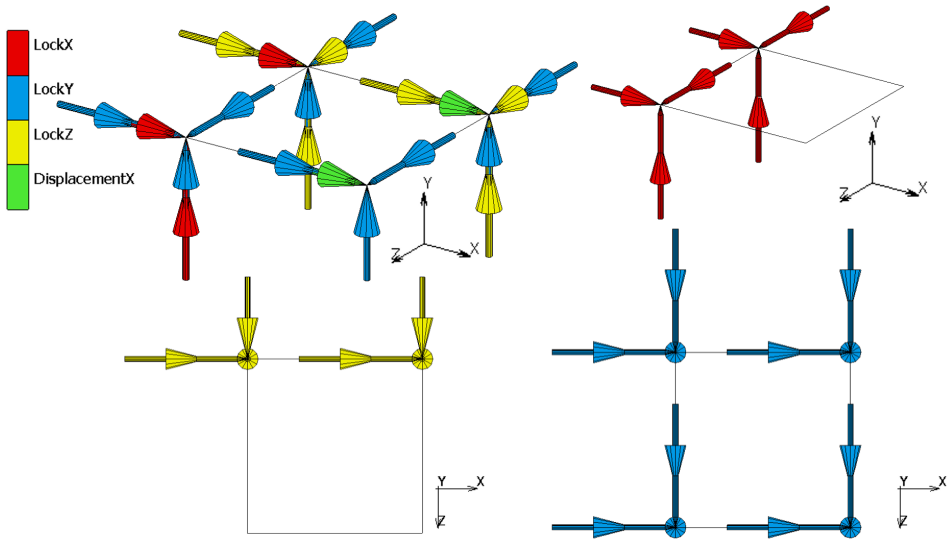



Figure 5.8: Model of the uniaxial tensile test for the shell elements

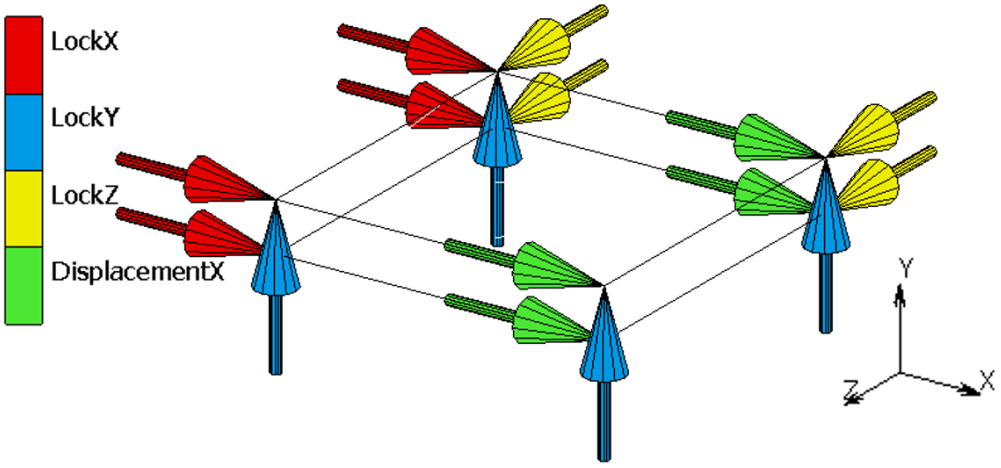



Figure 5.9: Model of the uniaxial tensile test for the solid and solid shell elements

The test achieves a stretched element (Figure 5.10) with a smaller thickness and width, but with a length twice as bigger as the one at the beginning of the simulation. The initial volume of the element is preserved. Analyzing the numerical results of stresses, strains, and displacements, present in Table 5.1, the models of the solid element and of the solid shell element have the same results, and all the models with shell elements have the same results among each other.

There are equal results for all the models with shell elements because there is not any shear stress, nor any stress or strain variation along the thickness direction. Thus, with an induced displacement in the transversal direction, there is no negative impact of having a thin or reduced integration shell formulation.

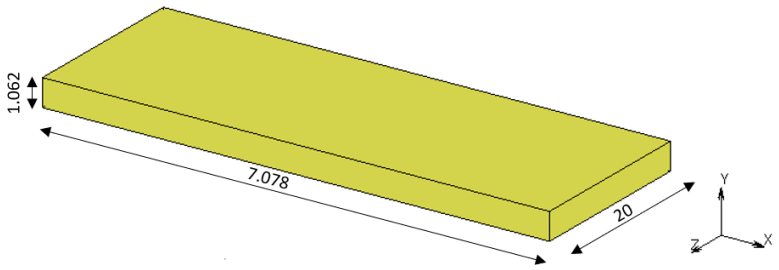



Figure 5.10: Stretched solid element after the uniaxial tensile test

It was also expected that the solid and solid shell elements would have the same results. Due to the direction of the induced displacement and to the degrees of freedom of the nodes, having seven layers of integration points (solid shell) instead of two layers (solid), or having one integration point per layer (solid shell) instead of four integration points (solid), has no influence on the results.

There is a small difference in the results between the solid elements and the shell elements. The final thickness and the transverse stresses $\sigma_2$ and $\sigma_1$ are different, being slightly smaller for the solid elements, as can be seen in Table 5.1. This is only due to the fact that shell elements do not account for stresses in the thickness direction $\sigma_3$, as the von Mises stress is the same across all the different element types.

Table 5.1: Uniaxial tensile test results: Z Displacement for the nodes not locked in the Z direction; stresses in the local coordinates and von Mises stresses (which, for one model, are the same for all the nodes)

| **Element type** | **Element thickness [mm]** | **Z Displacement [mm]** | $\sigma_1$ **[MPa]** | $\sigma_2$ **[MPa]** | $\sigma_3$ **[MPa]** | **von Mises** $\sigma$ **[MPa]** |
|---|---|---|---|---|---|---|
| **Solid** | 1.062 | -2.922 | -3.3 | 990.9 | -3.3 | 994.2 |
| **Solid Shell** | 1.062 | -2.922 | -3.3 | 990.9 | -3.3 | 994.2 |
| **Thick Shell** | 1.064 | -2.935 | -2.1 | 993.1 | 0 | 994.2 |
| **Thin Shell** | 1.064 | -2.935 | -2.1 | 993.1 | 0 | 994.2 |
| **Shell with reduced integration** | 1.064 | -2.935 | -2.1 | 993.1 | 0 | 994.2 |

To conclude, all elements are suitable for the simulation of a transversal uniaxial load case. The values from Table 5.1 will serve as a reference for some of the tests in the sections that follow.

## 5.3 Tensile test

This model aims to test the behavior of the elements when in the presence of in-plane shear, emulating the transverse deformation forming mechanism which can occur in roll forming due to the width reduction of the sheet between two stations, as mentioned in Section 2.1.1.3. The tensile test model is a variation of the previous uniaxial tensile test in Section 5.2. The main difference resides in the fact that half of the nodes subjected to the applied X displacement have their Z displacement blocked (Figure 5.11 and Figure 5.12), which is expected to induce in-plane shear in the element, breaking the uniaxial stress state. The previous uniaxial tensile test will serve as a comparison for the results of this new test.

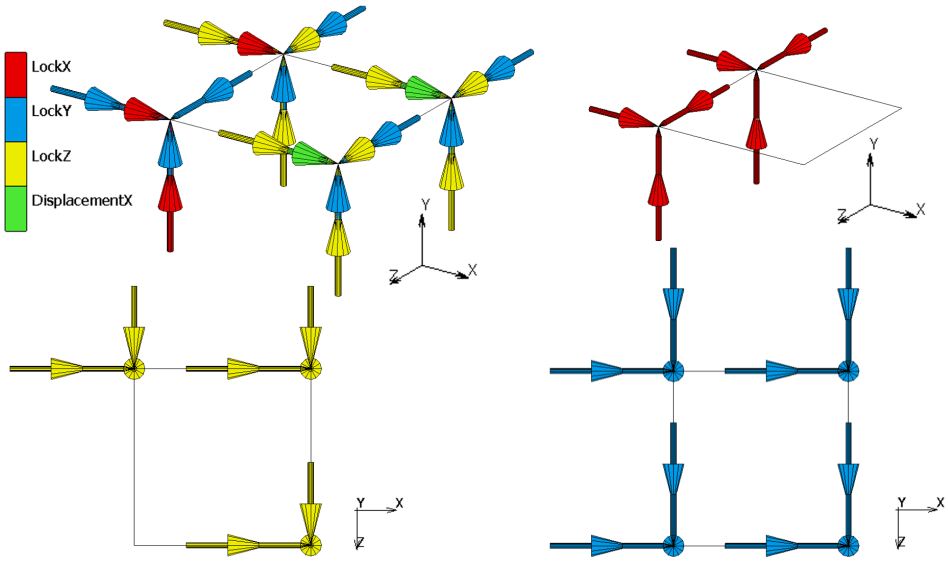



Figure 5.11: Model of the tensile test for the shell elements

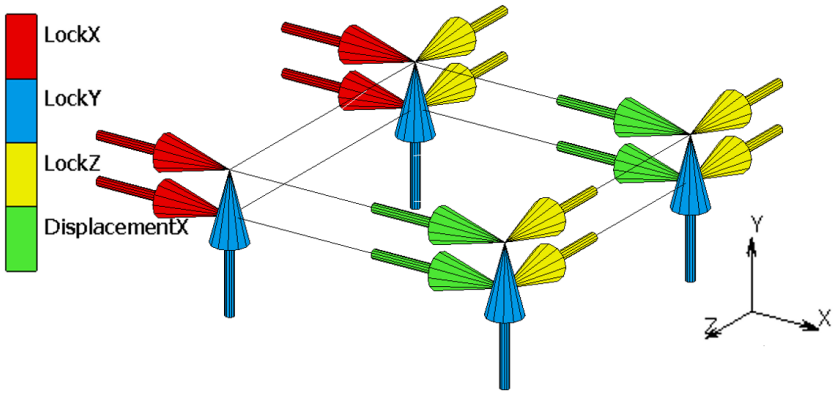
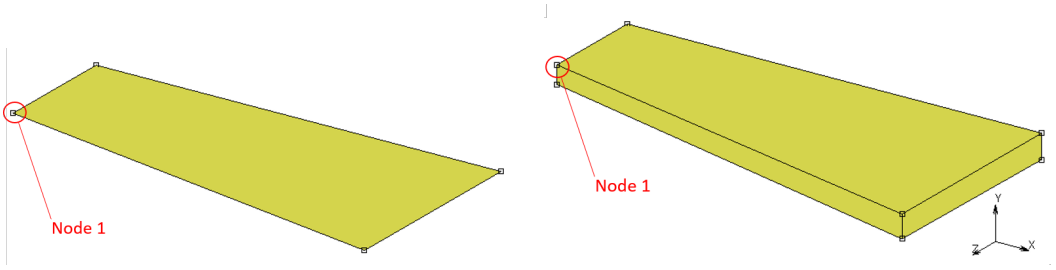



Figure 5.12: Model of the tensile test for the solid and solid shell elements

The tensile test is one of the standard element tests mostly used by authors, such as Betsch and Stein (1996), Li et al. (2015) and Pari et al. (2018). Apart from stresses and displacements, one relevant output variable to pay attention to is the reaction force resulting from the applied displacement. It is important to consider that Pari et al. (2018) simulate a 2D model, and Betsch and Stein (1996) and Li et al. (2015) conduct their simulations in a 3D model with a plane strain formulation. On the other hand, the models in this section were simulated in a 3D analysis, and it is expected that the solid and solid shell elements will not present a plane strain behavior, having some stresses and strains in the thickness direction. Moreover, Betsch and Stein (1996) constrain the thickness extensibility as a boundary condition, keeping it constant during the entire simulation, whereas the thicknesses of the models in the present work may vary.

Table 5.2: Tensile test results: element thickness for both sides; Z displacement and $\tau_{12}$ for Node 1 (Figure 5.13)

| **Element type** | **Element thickness (locked side) [mm]** | **Element thickness (displaced side) [mm]** | **Z Displacement [mm]** | $\tau_{12}$ **[MPa]** | **Reaction force $F_X$ [kN]** |
|---|---|---|---|---|---|
| **Solid** | 0.842 | 1.086 | -4.951 | -113.3 | 7.790 |
| **Solid Shell** | 0.769 | 0.769 | -0.422 | -0.9 | 8.807 |
| **Thick Shell** | 1.183 | 0.723 | -3.908 | -8.2 | 7.942 |
| **Thin Shell** | 1.170 | 0.725 | -3.828 | -17.2 | 7.953 |
| **Shell with reduced integration** | 0.756 | 0.756 | -0.059 | 1.1 | 8.864 |




(a) Model with thick shell element (b) Model with solid element

Figure 5.13: Stretched elements after the tensile test

At a first glance, the results in Table 5.2 show two different behaviors: fully integrated models have the width of the element significantly reduced in one of its sides; the elements with reduced integration only have a slight decrease in element width, which is smaller than the one during the uniaxial tensile test, contrarily to what should be expected, proving the inaccuracy of these elements when in the presence of shear. Furthermore, the thickness reduction is harsher on the elements with reduced integration and occurs with equal magnitude on both sides of the element, which complies with element volume conservation, because if fully integrated models have a bigger width reduction, they would be expected to have a smaller thickness reduction.

The uniform thickness reduction on the elements with reduced integration could be expected as they only have one integration point. However, a different result might be obtained when simulating this same test with more elements. Furthermore, similar reaction forces were obtained for the fully integrated methods, even though the shrinkage of the element in the Z and Y direction occurred differently for each element.

To sum up, it is not safe to conclude that all elements behave properly for this type of load, although there is some evidence that they might perform similarly during multi-element tests [Zienkiewicz et al. (2013)]. Lastly, it is evident the lack of accuracy for the reduced integrated elements when in the presence of shear for single element tests, and thus, attention should be put in the mesh discretization during multi-element tests, especially for these elements in specific.

## 5.4 Edge contact test

During the roll forming process, there is sometimes contact between the lateral rolls and the edge of the sheet, usually in the first stages [Halmos (2006)]. Concerns were raised in Section 2.2 for the use of shell elements in models with out-of-plane applied loads [DIANA FEA (2017)]. In order to assure the elements can correctly simulate this lateral contact, a model similar to the uniaxial tensile test in Section 5.2 was modeled. Instead of having an induced X displacement in some of the nodes which results in a tensile mode, an X displacement is induced in a contact surface, which results in a transverse compressive contact mode (Figure 5.14 and Figure 5.15). The main aim of the test is to analyze the behavior of the shell elements when edge contact is applied since contact is only established in two nodes, whereas for the solid model contact is established for four nodes.

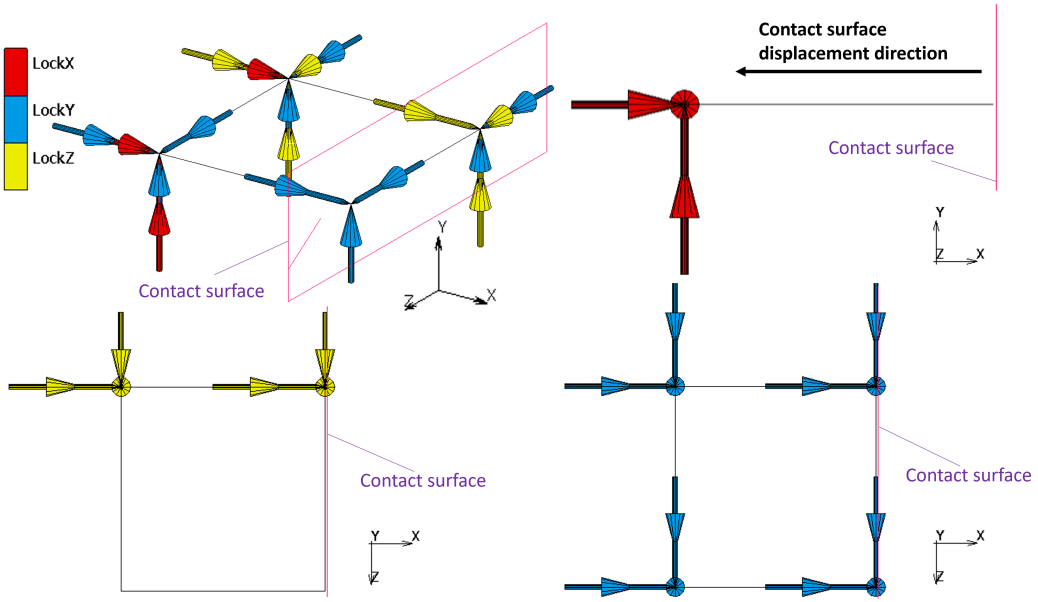



Figure 5.14: Model of the edge contact test for the shell elements

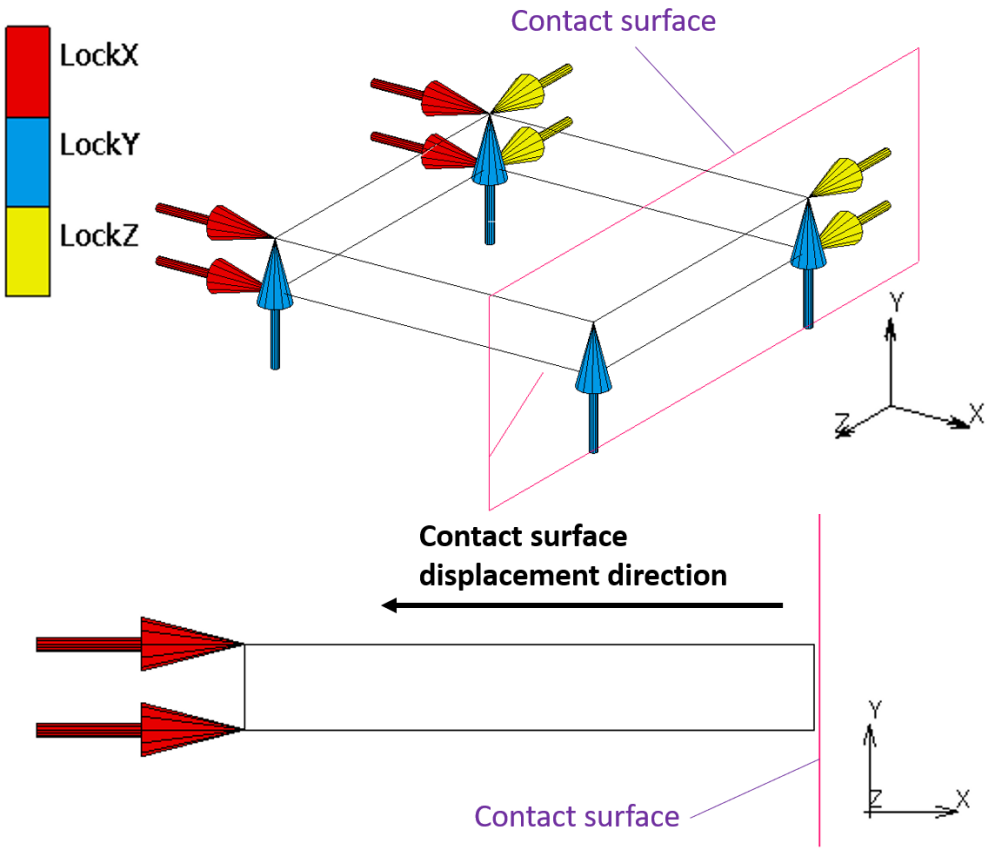



Figure 5.15: Model of the edge contact test for the solid and solid shell elements

Table 5.3: Edge contact tensile test results

| **Element type** | **Element thickness [mm]** | **Element width [mm]** | **von Mises $\sigma$ [MPa]** | **Surface reaction force $F_X$ [kN]** |
|---|---|---|---|---|
| **Solid** | 1.665 | 11.103 | 799.18 | 14.777 |
| **Solid Shell** | 1.665 | 11.103 | 799.18 | 14.777 |
| **Thick Shell** | 1.665 | 11.103 | 799.18 | 14.777 |
| **Thin Shell** | 1.665 | 11.103 | 799.18 | 14.777 |
| **Shell with reduced integration** | 1.665 | 11.103 | 799.18 | 14.777 |

Figure 5.16 shows the final state of the model with a solid element, which increases in width and thickness after an induced length reduction. As can be seen in Table 5.3, the results for this test, similarly to what happened during the uniaxial tensile test, are the same across all elements. The only difference resides in the fact that the solid and solid shell elements will have stresses and strains in the thickness direction. Moreover, the results were also the same when simulating the contact using segment to segment and node to segment contact detection [MARC (2021a)].

In this way, it can be concluded that all element types are suitable for the simulation of the lateral edge contact.

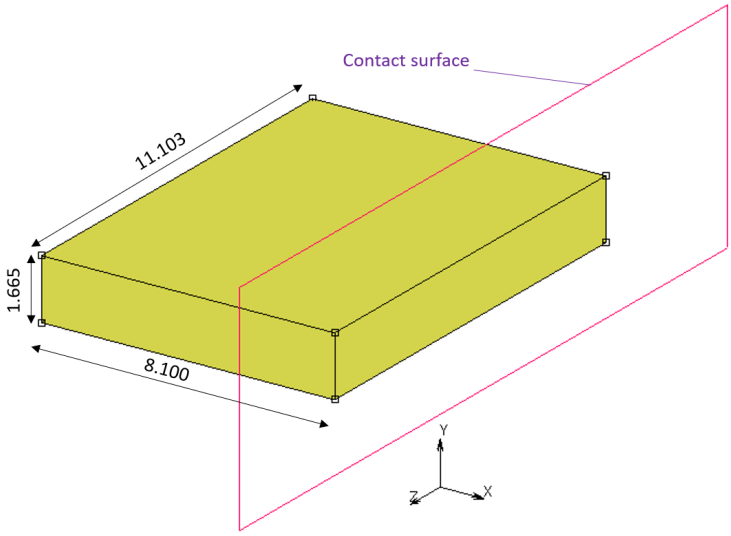



Figure 5.16: Deformed solid element after the edge contact test

## 5.5 Single element bending moment test

In this test, a bending moment is applied to one of the sides of the element, while the other side is encastered. As bending is the main deformation mode involved in roll forming [Marciniak et al. (2002)], as mentioned in Section 2.1.1.1, this test aims to analyze the behavior of the different elements when subjected to a bending moment, replicating the transverse bending forming mechanism.

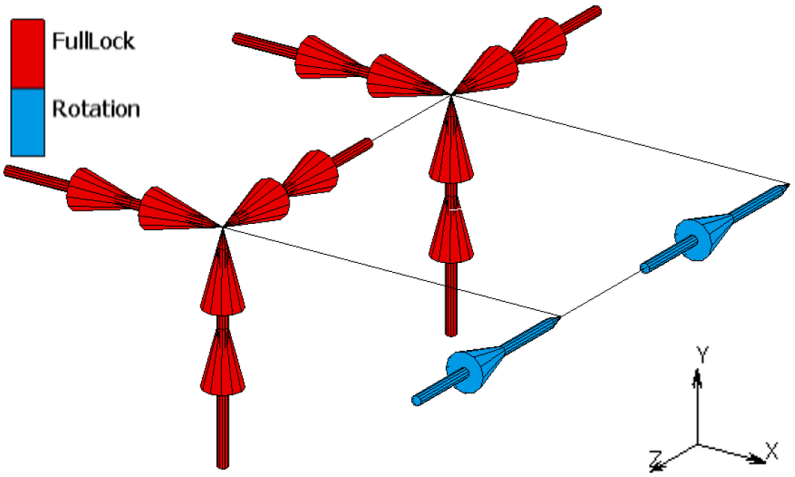



Figure 5.17: Model of the bending moment test for the shell elements

A bending moment can be replicated and directly applied to shell elements by defining a rotation in the boundary condition of the nodes. On the other hand, as the solid and solid shell

elements do not have rotations as degrees of freedom, the moment was replicated with the use of a contact surface with an induced rotation in the Z direction. The rotating surface is in contact with the nodes of the element, causing them to be displaced, and thus replicating the effects of a bending moment in the element. Figure 5.17 and Figure 5.18 show the boundary conditions of the models. Figure 5.19 shows the final state of the models with a thick shell element and with a solid element.

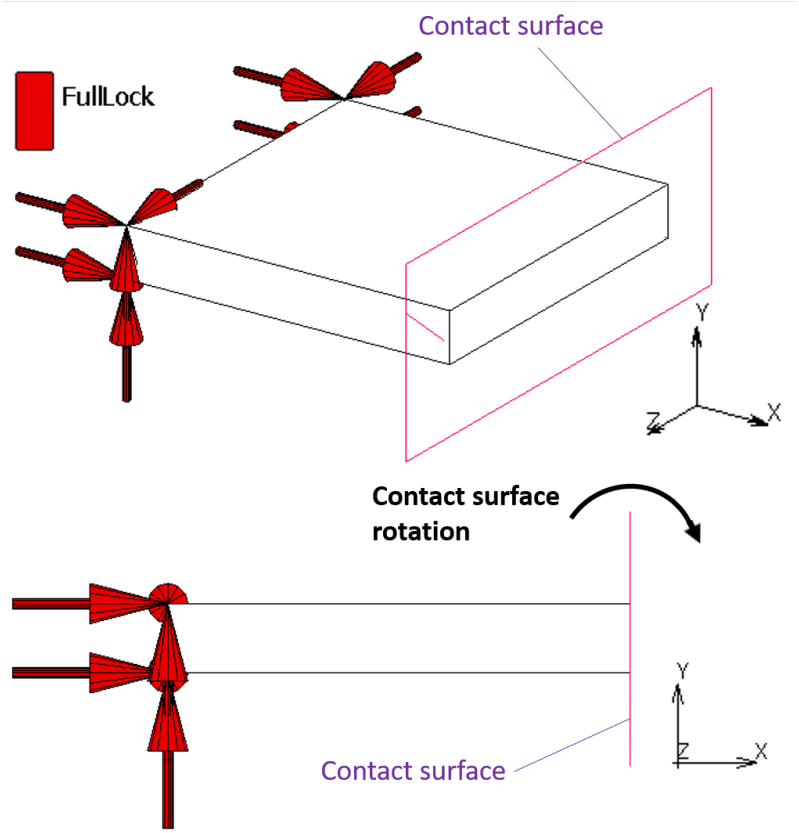
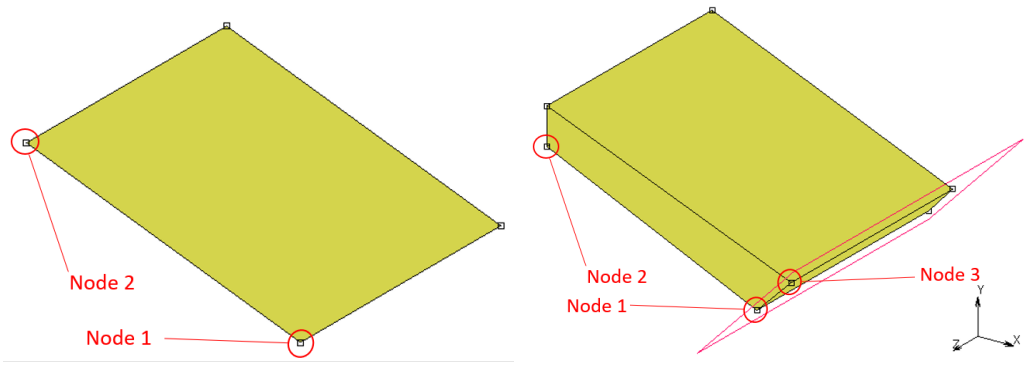



Figure 5.18: Model of the bending moment test for the solid and solid shell elements




(a) Model with a thick shell element (b) Model with a solid element

Figure 5.19: Deformed elements after the bending moment test

The results for the Y displacement presented in Table 5.4 were the first to be analyzed. As shell elements output the Y displacement for the middle layer, the displacement value for the solid and solid shell elements was obtained by calculating the midpoint between the top and bottom nodes. It can be seen that the thin shell presents a significantly smaller result when compared to the other elements.

Table 5.4: Results of the single element bending test: Displacement Y in Node 1 for the shells and average value between Node 1 and Node 3 for the solid and solid shell; von Mises $\sigma$, $\tau_{12}$, and $\tau_{23}$ for the bottom layer of Node 2 for the shells and in Node 2 for the solid and solid shell

| **Element type** | **Displacement Y [mm]** | **von Mises $\sigma$ [MPa]** | $\tau_{12}$ **[MPa]** | $\tau_{23}$ **[MPa]** |
|---|---|---|---|---|
| **Solid** | -3.913 | 703.44 | -3.14 | -156.152 |
| **Thick Shell** | -3.827 | 643.22 | 68.61 | 0 |
| **Thin Shell** | -3.201 | 573.31 | 113.75 | 0 |
| **Shell with reduced integration** | -3.827 | 643.15 | 0 | 0 |
| **Solid Shell** | -4.041 | 757.88 | 0 | -289.52 |

The thick and thin shells have similar formulations, only diverging on the fact that the thin shell does not consider transverse shear stresses and strains $\tau_{23}$, $\tau_{31}$, $\gamma_{23}$ and $\gamma_{31}$. Since for this simulation the thick shell element always outputted a value of 0 for these transverse shear stresses, the different behavior of the thin shell element could not be explained.

When analyzing the stresses, it can be seen that the solid and solid shell elements present significant values of $\tau_{23}$. This might be caused by transverse shear locking of the elements, which induces additional transverse shear. Euler-Bernouli beam theory neglects shear deformation and considers the transverse shear to be 0 for all the sections of the beam [Natal (2017)]. Higher-order beam theories presented by Öchsner (2014) do not disregard shear deformations, but still consider that for straight cross-sections which are normal to the beam axis before deformation, which in this case corresponds to the cross-section in the encastered side, there are no transverse shear stresses. Thus, $\tau_{23}$ stresses presented in Table 5.4 reflect a shear locking behavior of the solid and solid shell elements [Xia and Tang (1999)]. Timoshenko-Ehrenfest beam theory is of a higher order than the Euler-Bernouli beam theory and is normally used for these tests, but it is only valid for the elastic domain [Timoshenko (1953)].

In regards to the in-plane shear, as expected, the elements with reduced integration output a value of 0 for the $\tau_{12}$, because they only have one integration point in the centroid. These results are in compliance with the ones obtained for the tensile test in Section 5.3.

Even though the elements behaved differently in terms of stresses, the obtained element displacement was similar for all the elements (except for the thin shell). This is a first positive indication that these elements might successfully be used in the simulation of the bending modes involved in roll forming. The behavior of the thin shell could not be explained.

Lastly, the locking behavior of the solid and solid shell elements induces unexpected shear stresses, and thus higher von Mises Stresses. However, the solid and solid shell elements should not be discarded from being used in bending situations and in roll forming. This model represents the bending of a single element and was analyzed taking into consideration higher-order beam theories presented by Öchsner (2014), which consider $\tau_{23}$ and $\tau_{31}$ to be 0 for the center of the bend. On the other hand, in the transverse bending involved in roll forming, due to the plain-strain condition, $\tau_{12} = 0$ and $\tau_{31} = 0$, and thus, the behavior of the elements for that situation might be different [Marciniak et al. (2002)].

## 5.6 Air bending test

As mentioned in Section 2.1.1.1, bending is the main forming mechanism involved in the roll forming process, and the one responsible for the different shapes in the profile cross-sections [Marciniak et al. (2002)]. In order to further analyze the behavior of the different elements when subjected to bending, due to the importance of this forming mechanism, a multi-element bending test was modeled. This will also allow the clarification of some assumptions regarding elements' limitations, such as the use of only one element through the thickness for the solid element and its prominence to locking, and the hourglassing phenomenona associated with the reduced integration elements [MARC (2021b)] [Brunet and Ronel (1994)].

There are several bending tests available, such as U-bending, coining, and air bending [Velling (2019)]. An air bending test setup was chosen, with the aim of obtaining 90°bending angles for different bending radius. DP600 sheets with 1.5mm of thickness were used as specimens.

Roll forming has big flexibility in terms of possible bending radii that can be obtained. A small bending radius has the advantage of minimizing springback, whereas a bigger bending radius is used as a less harsh option for the material in terms of stresses avoiding possible cracks in the outside layer of the material [Hickey (2020)]. Thus, two different air bending tests were conducted aiming to achieve two different bending radii: $1.5mm$ with $r/t = 1$ and $15mm$ with $r/t = 10$, with $r$ corresponding to the bending radius and $t$ corresponding to the thickness of the sheet.

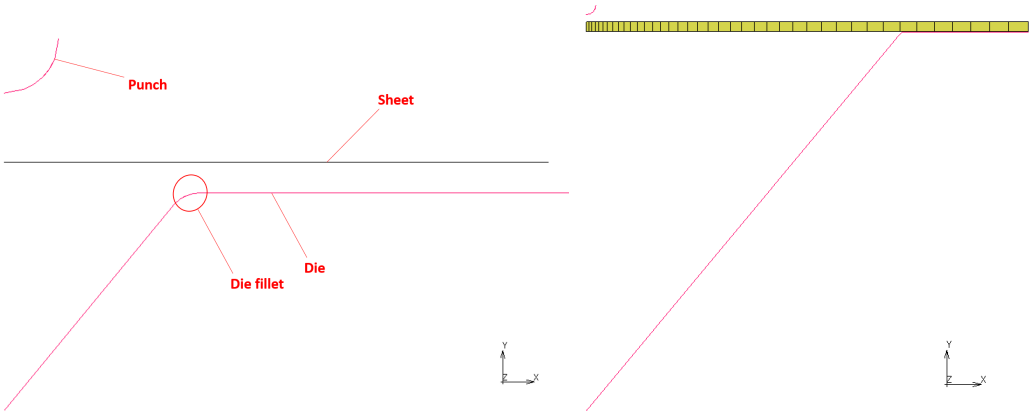
In an air bending test, the bending radius will depend on the die width and the punch radius. An equal punch radius of 1.5mm for both simulations was chosen to achieve easily comparable results. The chosen die width $V$ to achieve each desired inside bending radius $r_i$ was calculated using the empirical "rule of thumb" [Benson (2015a)], which states that for cold-rolled steel as the DP600:

$$r_i = 0.15 \times V \tag{5.1}$$

where:

- $V$ corresponds to the die width;
- $r_i$ corresponds to the inside bending radius.

Using this rule, die widths of 10mm and of 100mm were chosen. The support points' edges, also referred to as die fillets, have a radius of 1mm. The models of the air bending test can be viewed in Figure 5.20.




(a) Model with a thick shell element and a die width of 10mm

(b) Model with a solid element and a die width of 100mm

Figure 5.20: Air bending test models

Furthermore, to make sure a 90°bend is obtained, the stroke depth was calculated as:

$$y = \frac{V}{2 \times tan(\frac{\alpha}{2})} - (r_i + t + R_d) \times \frac{1 - sin(\frac{\alpha}{2})}{sin(\frac{\alpha}{2})} \tag{5.2}$$

where:

- $y$ corresponds to the stroke depth;
- $V$ corresponds to the die width;
- $\alpha$ corresponds to the desired bending angle
- $r_i$ corresponds to the inside bending radius;
- $t$ corresponds to the thickness of the sheet;
- $R_d$ corresponds to the radius of the fillet in the die.

Based on Equation 5.2 the punch will have an induced displacement of -3.75mm and -43.20mm for the 1.5mm and 15mm bending radius respectively, which will allow to obtain a 90°bend when the punch finishes its descending movement.

In order to assure these stroke depths were yielding the expected internal bending radius, a least-squares fitting algorithm was used, which determines the center coordinates and the radius of a circle that fits a set of given points [Chernov and Lesort (2005)]. The bending radius averaged 1.65mm and 11.40mm for the 15mm and 150mm die width respectively.

As this model represents bending along a straight line of a continuous sheet with its thickness significantly smaller than its width and length, the strain parallel to the bend line is considered to

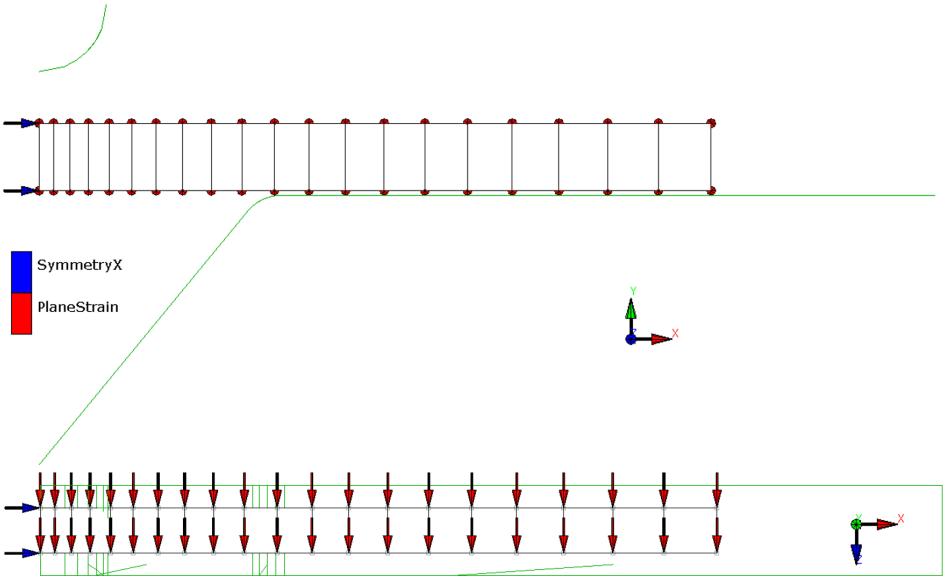



Figure 5.21: Boundary conditions of the air bending test for the solid and solid shell elements

be zero and a plane strain model can be considered [Marciniak et al. (2002)]. Therefore, a sheet with a unitary width value was simulated, and the Z displacement was restricted for all the nodes, in order to fulfill the plane strain condition (Figure 5.21). Moreover, due to the symmetry of the test, only half of the sheet was modeled. Additional boundary conditions were attributed to the nodes in the bend line in order to fulfill the symmetry in the X direction.

In order to analyze the springback behavior of the different elements, an additional step was added. Contact with the die and punch is no longer established, and two nodes in the bend line have their displacements and rotations completely restricted in order to stabilize the model. The rest of the nodes are free to move, representing the elastic recovery of the material.

A tuning of some model parameters was conducted. The tuning in this test is extremely relevant as it allows to draw some conclusions in a simple and fast-to-simulate model, which can then be applied to the complex and slower-to-simulate roll forming model. As expected, contact parameters played an important role in the efficiency and accuracy of the model. Shell elements did not converge for the default value of 1 for the contact tolerance bias factor, a parameter responsible for the position of the contact tolerance zones (Figure 5.22), in other words, the position of the boundaries that define if contact is established or if the node penetrated the contact surface [Gu (2021)]. A reduction of this parameter can help to achieve convergence but may increase the wall time of the simulation [MARC (2021a)]. A value of 0.9 was used for the rest of the simulations, and if in future roll forming simulations convergence is not achieved, this value can be decreased even further.

Furthermore, it was found that enabling the smooth boundary condition of the meshed sheet contact body allows for a more uniform and accurate contact. With a smooth boundary condition, there is an analytical description of the segments that connect each node, allowing for a better

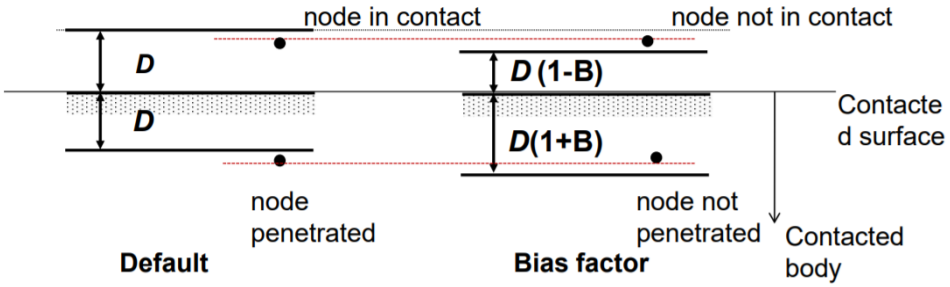



Figure 5.22: Distance tolerance (D) and bias factor (B) [Gu (2021)]

representation of contact especially with curved surfaces and for coarse meshes [Yu et al. (2009)] [MARC (2021a)].

Lastly, the contact control method also played an important role in the results. For solid elements node to segment is undoubtedly the best option, especially when simulating small bend radii, as using segment to segment often resulted in an excessive and abnormal thickness reduction near the bend line. For shell elements, the results were similar for both contact methods, with the node to segment contact method yielding slightly faster simulations [MARC (2021a)]. Thus, node to segment was the contact method chosen for all the simulations. However, it is important to consider the limitations of the node to segment contact method when it comes to the simulation of double-sided contact, which did not occur in this model but may occur in the roll forming models [MARC (2021b)].

Table 5.5: Air bending test results for a die width of 10mm before springback

| **Element Type** | $\sigma_2$ **[MPa]** | | | **Thickness [mm]** |
|---|---|---|---|---|
| | **Top Layer** | **Mid Layer** | **Bottom Layer** | |
| **Reference - 4 Solid elements through thickness** | -1275.74 | 624.32 | 1005.39 | 1.417 |
| **Solid** | -643.98 | - | 813.61 | 1.316 |
| **Thick Shell** | -1058.58 | -239.03 | 1077.12 | 1.507 |
| **Thin Shell** | -1042.41 | -179.62 | 1041.17 | 1.502 |
| **Shell with reduced integration** | -1096.94 | -227.42 | 1093.02 | 1.507 |
| **Solid Shell** | -1312.97 | 223.57 | 1094.54 | 1.465 |

Analyzing the results in Table 5.5, a thickness reduction can be seen for the solid element during the small radius bending. In small radius bends, the through-thickness stress cannot be assumed to be zero [Marciniak et al. (2002)]. If the bend radius is too small and too sharp, and the forming force is too high, the punch nose may penetrate the material and crease the center of the bend [Benson (2015b)], as it is seen in Figure 5.23. Therefore, sharp bend might be occurring in this situation, a phenomenon that is represented by the solid and solid shell elements, as seen in

Figure 5.24, which yield a thickness reduction in the bend line. This sharp bend is not represented by the shell elements, as they do not account for the stresses in the thickness direction $\sigma_3$, and their thickness remains close to 1.5mm (it even increases by a residual amount).

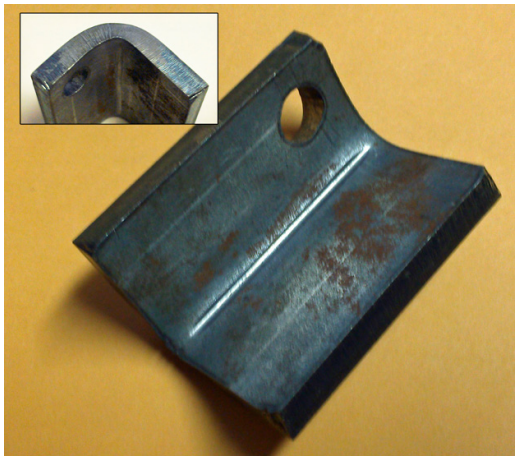


Figure 5.23: Representation of a sharp bend. The material was stamped in the middle of the bend, leading to a thickness reduction [Benson (2015b)].

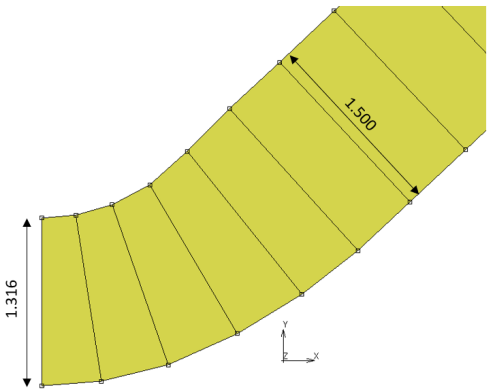



Figure 5.24: Sharp bend phenomenon for the model with solid elements and die width of 10mm. There is a local thickness reduction in the bend line

It was also expected that the fibers in the inner side of the bend would be subjected to compression, whereas the ones on the outer side of the bend would be subjected to traction. All the different elements managed to represent this correctly, having a negative value of $\sigma_2$ for the top layer/nodes and a positive value of $\sigma_2$ for the bottom layer/nodes, near the bending zone. Moreover, for a small bending radius and when in the presence of thinning of the sheet (Figure 5.25), the neutral axis gets closer to the inner layer of the sheet [Benson (2018)] [Marciniak et al. (2002)]. Therefore, the neutral axis stops being coincident with the mid-layer of the shell and solid shell elements, and thus $\sigma_2$ in the mid-layer should be positive. This is only verified for the solid shell elements.

It is also important to know the forces induced in the punch, and in the rolls in case of roll forming, to design the machine accordingly. The force in the punch $F_q$ can be analytically predicted based on the thickness of the sheet t, the width of the die $V$, the ultimate tensile strength of the material $\sigma_r$ and the width of the sheet used $l$, as indicated by the following equations:

$$F_q = k \times \frac{\sigma_r \times l \times t^2}{V} \tag{5.3}$$

$$k = 1 + \frac{4 \times t}{V} \tag{5.4}$$

Lastly, an important value to analyze is the geometry accuracy and the springback. This can be analyzed by looking at the bending angle both when the punch finishes its descending movement

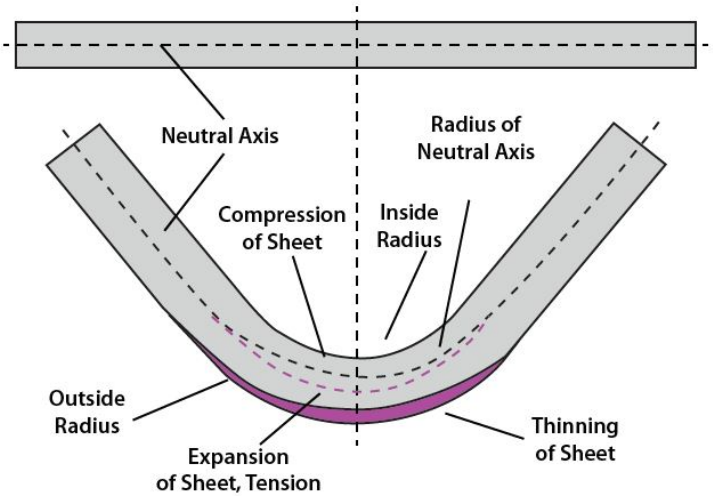



Figure 5.25: Shifting of the neutral axis towards the inside radius [Benson (2018)]

and after the punch is no longer in contact with the sheet. The results for the bending angles, spring back, and punch force are synthesized in Table 5.6 and Table 5.7.

Table 5.6: Springback and punch force results for a die width of 10mm

| **Element Type** | **Bending angle** | | | | **Peak punch force [N]** |
|---|---|---|---|---|---|
| | **Before elastic recovery [°]** | **After elastic recovery [°]** | **Value of elastic recovery [°]** | **Difference to reference [%]** | |
| **Reference - Solid with 4 elements through thickness** | 89.77 | 92.63 | 2.86 | 0.00 | 117.89 |
| **Solid** | 93.12 | 95.51 | 2.38 | -16.73 | 107.84 |
| **Thick Shell** | 91.13 | 93.97 | 2.84 | -0.85 | 101.26 |
| **Thin Shell** | 90.58 | 93.46 | 2.88 | 0.76 | 111.11 |
| **Shell with reduced integration** | 91.14 | 93.99 | 2.85 | -0.34 | 101.26 |
| **Solid shell** | 91.42 | 94.24 | 2.81 | -1.59 | 108.23 |
| **Theory** | - | - | - | - | 105.06 |

For the smaller bending radius, all elements accurately measured the force induced in the punch. For a bigger bending radius, due to some spikes, the solid element overestimates the punch force. This might be attributed to shear locking, which makes the element stiffer and more resistant to induced displacements [Brunet and Ronel (1994)], as there is the presence of shear stress $\tau_{23}$.

The stiff behavior of the model with online one layer of solid elements is also seen in the results for the bending angle before springback. All elements yield values close to the reference, except for the solid element, which yields a bigger bending angle.

Table 5.7: Springback and punch force results for a die width of 100mm

| **Element Type** | **Bending angle** | | | | **Peak punch force [N]** |
|---|---|---|---|---|---|
| | **Before elastic recovery [°]** | **After elastic recovery [°]** | **Value of elastic recovery [°]** | **Difference to reference [%]** | |
| **Reference - Solid with 4 elements through thickness** | 82.91 | 105.87 | 22.96 | 0.00 | 10.01 |
| **Solid** | 85.09 | 102.35 | 17.27 | -24.81 | 24.35 |
| **Thick Shell** | 82.88 | 103.99 | 21.11 | -8.08 | 7.43 |
| **Thin Shell** | 83.10 | 103.99 | 20.89 | -9.01 | 7.54 |
| **Shell with reduced integration** | 83.23 | 103.91 | 20.68 | -9.95 | 7.43 |
| **Solid shell** | 83.20 | 100.27 | 17.07 | -25.67 | 7.77 |
| **Theory** | - | - | - | | 7.69 |

Regarding the springback, for a small bending radius, only the solid element has a significant deviation from what is expected, underestimating the springback. This could be expected just by looking at the stresses in Table 5.5, as it is known that the smaller the stress difference between the top and bottom layers of the blank, or in other words the smaller the through-thickness stress gradient along the formed part, the lower the level of springback [Wang et al. (2017)]. For the bigger bending radius, there is some locking of the solid element which results in a bigger bending angle after the punch reaches the desirable stroke depth. Moreover, both the solid shell and solid elements underestimate the elastic recovery. It is important to note that the results were not compared with empirical or analytical results, but instead with the reference model with 4 solid elements through the thickness.

To sum up, it can be seen that all the element formulations have their own advantages and disadvantages. Firstly, it was seen that all three shell elements yielded similar results. Thus, between the three, the shell with reduced integration would be the most interesting element, as it is expected to have a smaller computation time. On one hand, for a smaller bending radius, the solid shell seems to be a very good option, as it not only correctly represents the thinning phenomenon of the sheet and the through-thickness stress distribution, but it also has a relatively accurate representation of the springback. It must also be mentioned that all the elements yielded the punch force correctly. On the other hand, for a bigger bending radius where no thinning phenomenon occurs, the shell elements seem to be the best option due to the correct representation of the punch force and of the springback.

Hasty conclusions should not be drawn, especially since some of the results taken in this subsection conflict with results taken from other authors, that claim that shell elements do not yield accurate springback results for small $r/t$ ratio and that models with several solid elements through

the thickness, or with a single element through the thickness but with an assumed strain formulation, are usually the most reliable option [Xia and Tang (1999)] [Lia et al. (2010)]. Therefore, all previous conclusions still require to be validated in a roll forming simulation.

## 5.7 Conclusions

The behavioral element tests were important not only to better understand the element formulations but also to tune some simulation parameters. Table 5.8 presents a summary of the conclusions drawn in these tests.

The shell elements appear to be a viable alternative to the solid elements, but their behavior in the presence of double-sided contact is yet to be tested in the context of roll forming. When subjected to bending, shell elements appear to accurately yield changes in the geometry, especially for smaller bending radius. The elements with reduced integration yielded poor in-plane shear results for a single element test, but their behavior with multiple elements is yet to be tested. To sum up, insights on the strengths and weaknesses of each element were gained. As each element type has characteristics that distinguished it from the others, every element type will still be considered and analyzed on the roll forming tests.

Table 5.8: Summary of conclusions for the behavioral tests

| Test | Conclusions |
|---|---|
| **Double-sided contact** | • Solid and solid shell elements provide accurate results;<br>• Numerical instability for the shell elements, which are still able to converge. |
| **Uniaxial tensile test** | • Every element type can simulate simple uniaxial tensile stress states. |
| **Tensile test** | • Elements with reduced integration neglect in-plane shear stress when using a coarse mesh. |
| **Edge contact test** | • Lateral edge contact can be established by every element type;<br>• Both segment to segment and node to segment contact methods can be used. |
| **Single element bending** | • The thin shell element is prone to have smaller displacements when subjected to bending;<br>• The solid and solid shell elements are prone to present an over stiffing behavior when subjected to bending;<br>• Elements with reduced integration neglect in-plane shear stress when using a coarse mesh. |
| **Air bending test** | • Reducing the contact tolerance bias factor can be used to solve convergence issues for the shell elements;<br>• Smooth boundary condition of the meshed sheet contact body allow for a more uniform and accurate contact;<br>• Node to segment contact method yields more accurate results for the solid elements;<br>• Node to segment contact method yields more efficient results for the shell elements;<br>• Shell elements do not represent thinning for small bending radius;<br>• The solid and solid shell elements are prone to present an over stiffing behavior for bigger bending radius;<br>• Shell elements accurately represent elastic recovery, especially for small bending radius. |

# Chapter 6

# Roll forming tests

This chapter presents the numerical simulation of a C-Profile produced by roll forming. The FEA models were created using the COPRA® FEA RF software package. The material model, the boundary conditions, and other assumptions which make the creation of the model possible are also mentioned. The main goal of this chapter is to test the different element types in a roll forming context and to assess if the different models accurately represent the sheet behavior and the forming mechanisms involved in the process. This chapter also verifies if the assumptions and conclusions drawn during the simple element tests are still valid for a roll forming model.

## 6.1 Model definition

### 6.1.1 Geometry and flower

With the definition of the desired final cross-section, the flower and the roll design were developed using COPRA® RF, and the simulation models were automatically prepared for COPRA® FEA RF.

The product aimed to be obtained was a symmetrical C-shaped profile with 220mm of length. The dimensions of the profile can be seen in Figure 6.1 and Figure 6.2. The distance between stations was also 220mm. A sheet of 506mm ($220mm \times 2.3$) was simulated, in order to assure that the sheet is always in contact with the rolls in at least 2 stations. This rule comes from the experience of data M with the numerical simulation of roll forming and was proven to give additional stability to the simulation and to better replicate the production of a profile from a sheet coil. For the same meshing definition, simulating a sheet with a bigger length would lead to higher computational costs. Due to the symmetry of the cross-section, only half of the sheet was simulated.

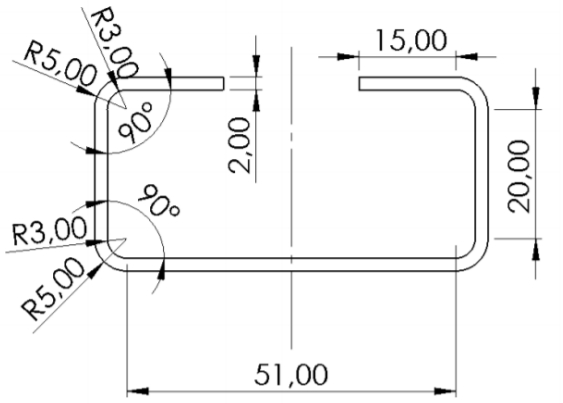



Figure 6.1: Cross-section of the C-shaped profile

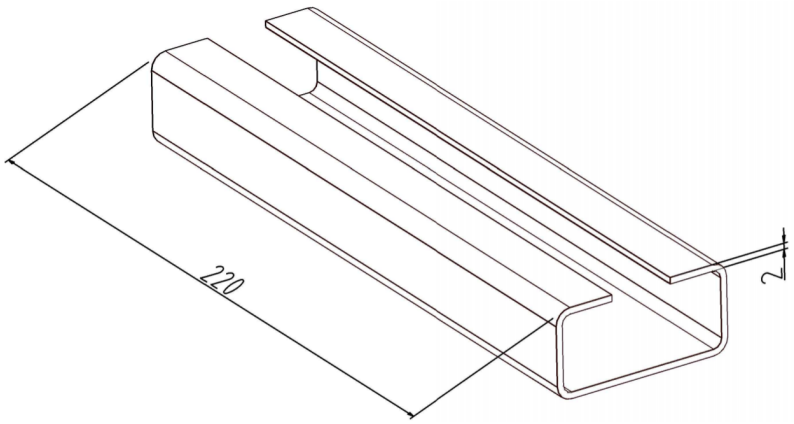



Figure 6.2: Isometric view of the C-shaped profile

The flower diagram of the profile is shown in Figure 6.3, evidencing the stages of the forming of the cross-section.

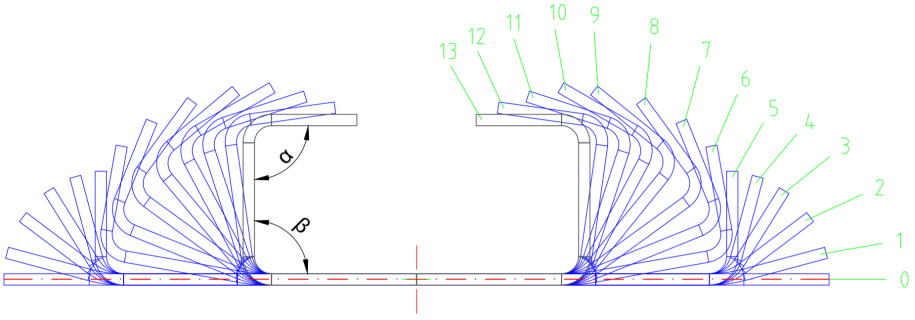



Figure 6.3: Flower diagram with the forming sequence of the C-Profile, and the expected cross-section in each station;

For all the simulations, the global coordinate system, which can be seen in Figure 6.4, was:

- $x$ for the width direction when the sheet is flat;

- $y$ for the thickness direction when the sheet is flat;
- $z$ for the forming direction, and direction of the travel of the rolls in relation to the sheet.

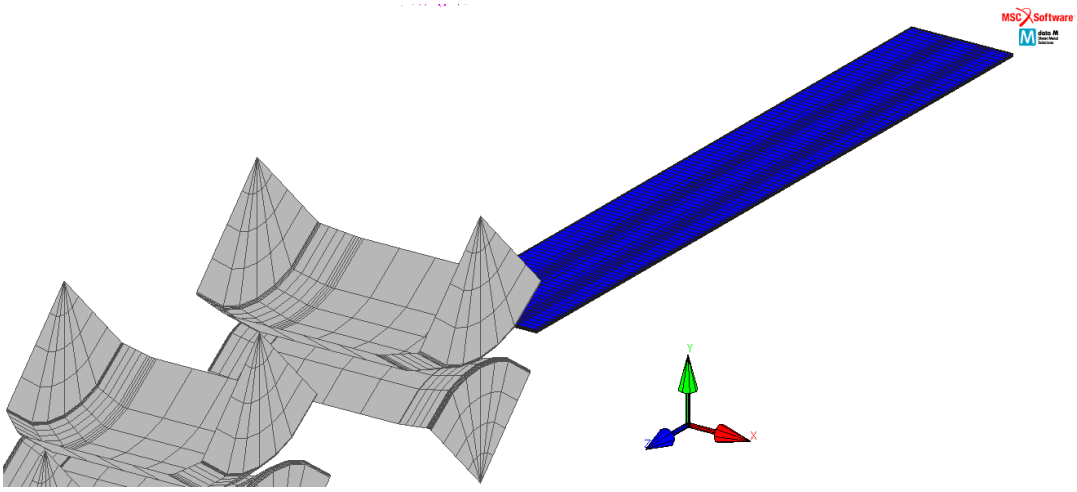


Figure 6.4: Global coordinate system of the roll forming simulation. $x$ axis is red; $y$ axis is green; $z$ axis is blue

Concerning the local coordinate systems, shown in Figure 6.5, these follow the elements as they are deformed. Concerning the local coordinate systems:

- 1 is parallel to $z$ at the beginning of the simulation. It corresponds to the longitudinal direction of the elements;
- 2 is parallel to $x$ at the beginning of the simulation. It corresponds to the width direction of the elements;
- 3 is parallel to $y$ at the beginning of the simulation. It corresponds to the thickness direction of the elements.

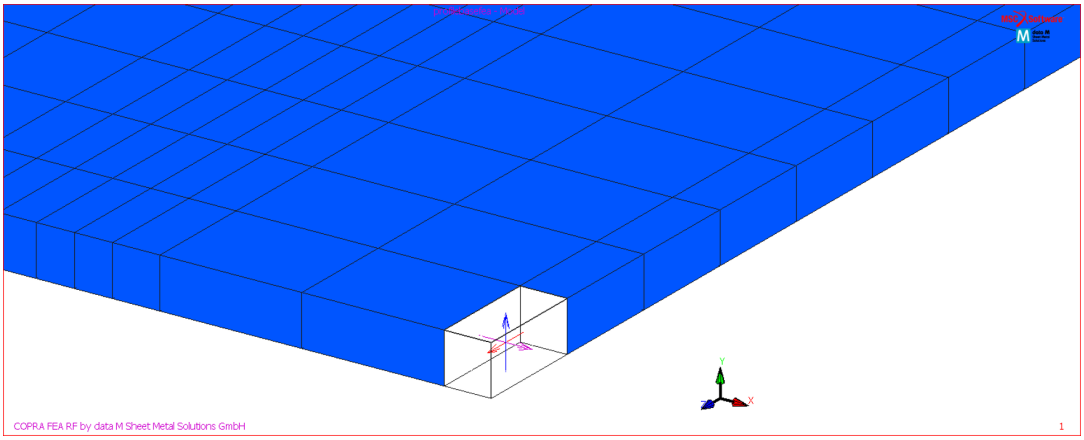



Figure 6.5: Local coordinate system of solid elements in the beginning of a roll forming simulation. Direction 1 direction is red; direction 2 is magenta; direction 3 is blue

### 6.1.2 Geometry modeling

The roll forming models are composed of two different parts: the rolls and the sheet.

The rolls are modeled as rigid bodies, which move through space without changing their shape. Each rigid body is composed of a group of analytical NURBS Surfaces, and the motion of this rigid body is defined by specifying the position of its center of rotation as a function of time [MARC (2021a)]. Modeling the rolls as a rigid body does not allow to study the deformation of the rolls, which is generally not relevant for roll forming, but brings advantages in terms of computational efficiency [Dassault Systèmes Simulia Corp (2011)][Halmos (2006)]. Using an analytical description for the surfaces of the rigid bodies is advantageous as it leads to greater accuracy in the representation of the geometry, and a more accurate calculation of the surface normal, which translates to a better yielding of contact results [MARC (2021a)].

Concerning the metal sheet, it is modeled as a deformable body, an arbitrarily shaped part that can be meshed and deformed under load.

### 6.1.3 Mesh definition

As defined by MARC (2021a), *"mesh definition is the process of converting a physical problem into discrete geometric entities for the purpose of analysis. Before a body can undergo finite element analysis, it must be modeled into discrete physical elements"*.

The mesh definition can be easily conducted using COPRA2FEA pre-processing tool, which allows for fast mesh refinement, done by interacting with the window in Figure 6.6. There is also flexibility in terms of applying different mesh definitions for different areas of the strip. The mesh definition was based on the experience of roll forming simulations at data M. A higher density of elements leads to better results but worse computation times. The mesh of the sheet can be previewed, as Figure 6.7 shows.

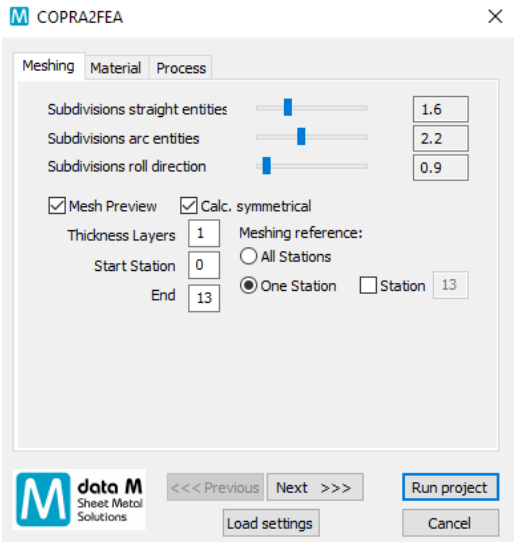



Figure 6.6: Mesh refining tab in COPRA2FEA

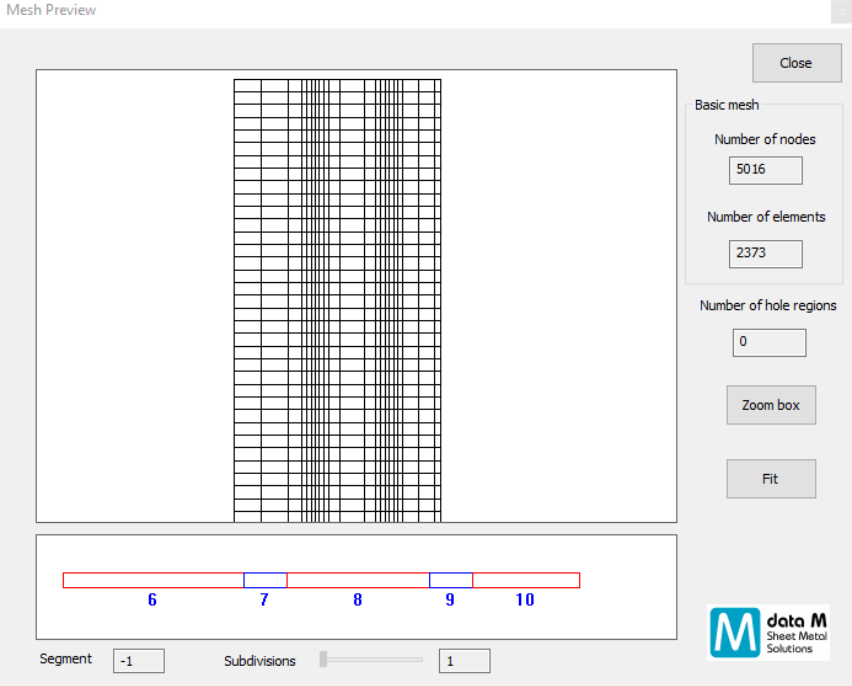



Figure 6.7: Preview of the mesh

The number of element layers through the thickness can also be defined. By default, this value is set to 1, which might be enough to accurately represent the bending behavior in certain situations. However, a model with four layers of solid elements will be used as a reference in the result analysis that will follow, as it is better suited to avoid locking phenomenona and to depict the behavior of the sheet fibers and the through-thickness stress gradient involved in bending [Autodesk (2018)] [Xia and Tang (1999)].

### 6.1.4 Material model

The material of the sheet was modeled as an elastic-plastic material with isotropic hardening, using the Swift's law [Swift (1952)]:

$$\bar{\sigma}_p = K(\varepsilon_0 + \bar{\varepsilon}_p)^n \tag{6.1}$$

where:

- $\bar{\sigma}_p$ corresponds to the equivalent stress;
- $\bar{\varepsilon}_p$ corresponds to the equivalent plastic strain;
- $K$, $n$, and $\varepsilon_0$ are material constants that can be determined by using points of the stress-strain curve when conducting a uniaxial tensile test [Fernandes et al. (1998)].

The material used was the DP600, a cold rolled dual phase steel with good formability, commonly used in automotive applications [SSAB (2018)]. Due to its formability, DP600 is considered

to have a very good performance for both roll forming and deep drawing [Tata Steel (2016)]. The material properties considered were the ones provided by SSAB (2018), which can be found in Table 6.1:

Table 6.1: Mechanical properties of DP600

| **Young's modulus [GPa]** | **Poisson's ratio** | **Yield Strength $R_{p0.2}$ [MPa]** | **Ultimate Tensile Strength [MPa]** | **Elongation $A_{80}$ [%]** |
|---|---|---|---|---|
| 210 | 0.3 | 320 | 650 | 20 |

With these values for mechanical properties, COPRA2FEA calculates the constants of the Swift Law present in Table 6.2.

Table 6.2: Swift Law constants for the DP600

| $K$ **[MPa]** | $\varepsilon_0$ | $n$ |
|---|---|---|
| 1063.799 | 0.00139 | 0.1823 |

The values of the constants of the Swift Law obtained are in line with existing literature that also studied the work hardening behavior of the DP600, such as Stoughton et al. (2013).

### 6.1.5 Boundary conditions

Since only half of the sheet was simulated, in order to reduce the computation time, a $x$-direction boundary condition (seen in Figure 6.8) was applied to all the nodes in the symmetry line. This prevents these nodes from moving in the $x$ direction.

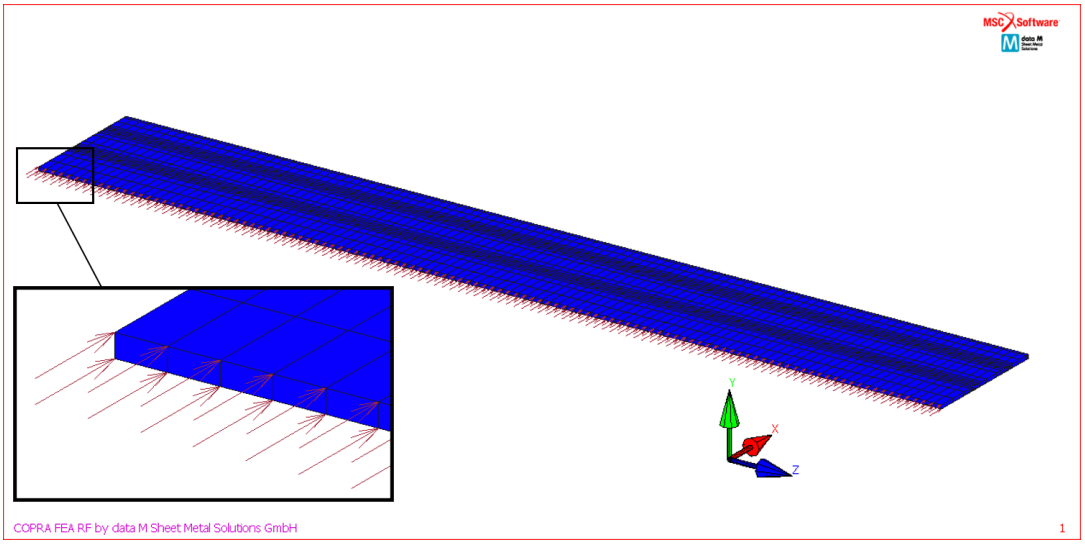



Figure 6.8: $x$-direction boundary condition

Moreover, on the tail of the profile, three nodes in the symmetry line had their movement in the $y$ direction restricted. This boundary condition was used in order to prevent a rigid body

motion of the strip, giving more stability to the simulation [Batchu (2015)]. The nodes that were restricted are the ones in Figure 6.9, as a result of several experiments conducted by data M, which concluded these were the nodes with the least influence in the roll forming process. It is also important to mention that this part of the sheet containing these nodes will be cut-off in the final stage of the simulation, reducing even further the possibilities of an undesirable effect of this boundary condition on the final product.

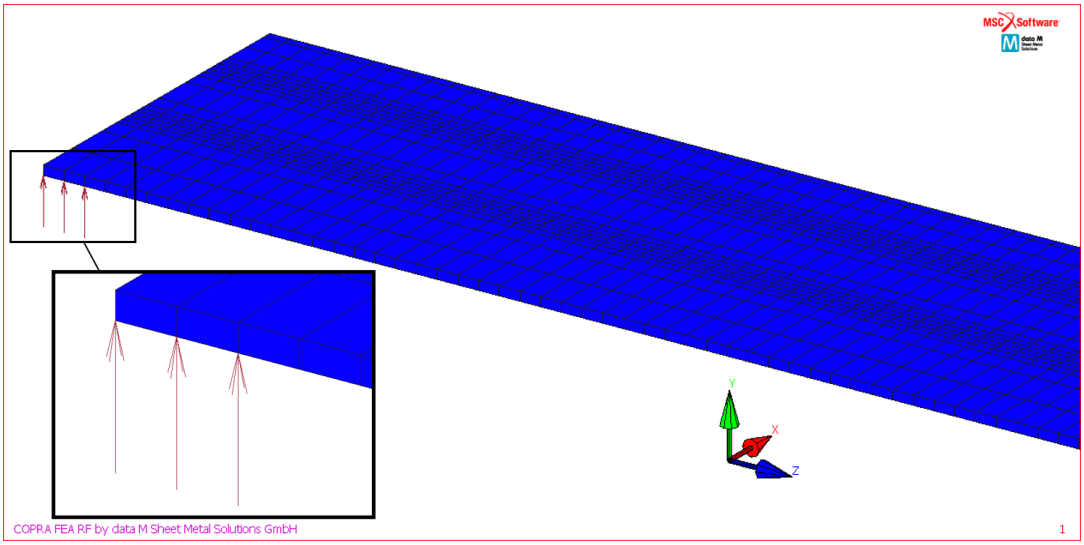



Figure 6.9: $y$-direction boundary condition

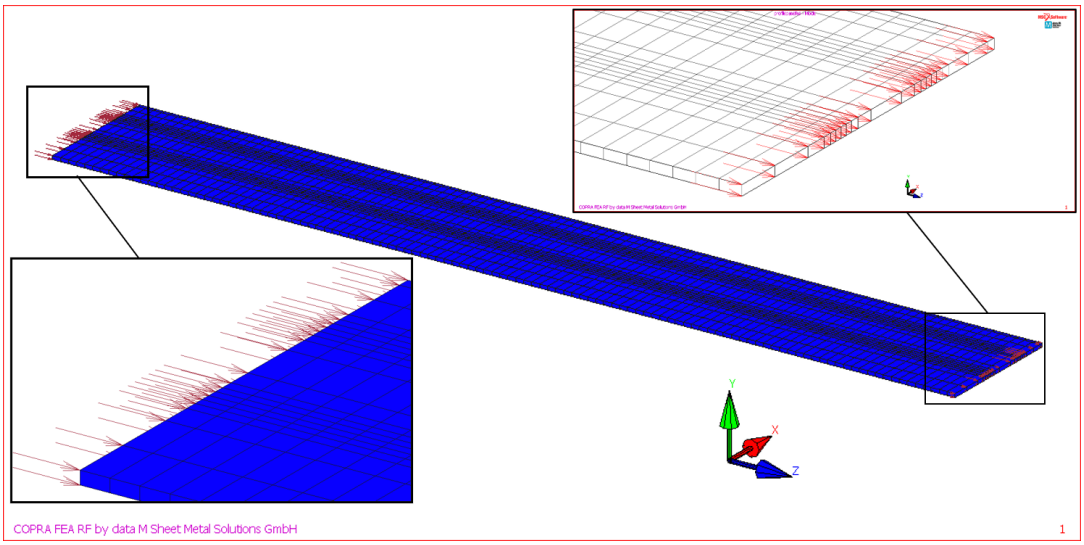



Figure 6.10: $z$-direction boundary condition

Concerning the $z$-direction boundary condition, this will simulate the continuous existence of strip, replicating a sheet coil being used, and is thus applied on the nodes in the extremities of the sheet, as shown in Figure 6.10. With this boundary condition, the strip will not move in the $z$ direction and will keep its length constant. In a real roll forming scenario, the rolls are static and

the sheet is the one that moves from station to station. In the numerical simulations conducted in this thesis, the sheet is static in the $z$ direction, and the rolls have an induced displacement, assuring a relative displacement between the rolls and the sheet.

Lastly, an additional boundary condition was applied during the increments corresponding to the free cut, as seen in Figure 6.11. Nodes in both the front and tail of the sheet were locked in all directions. The element right before the region where the sheet will be cut-off is also locked, in order to avoid rigid body motion after the cut.

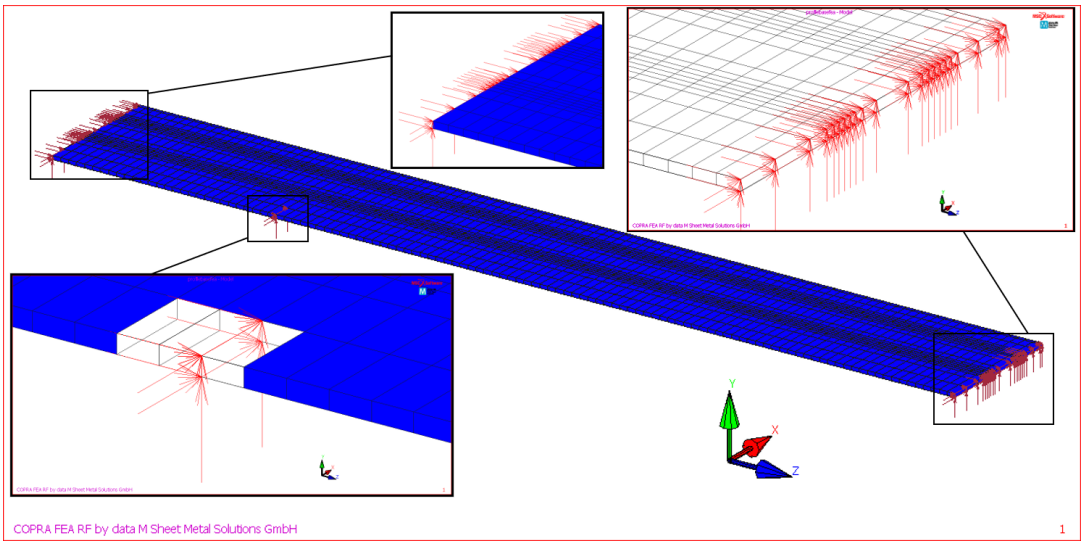



Figure 6.11: Additional boundary condition for the cut-off

These boundary conditions need to be adapted for the models with shell elements. When an entire face has its nodes restricted in a specific direction for the models with solid elements and that face is represented by an edge in the models with shell elements, there is the need to restrict the rotations of the nodes in that sheet edge in a way that:

- When the restriction is in the $x$ displacement, the $y$ and $z$ rotations should also be restricted (Figure 6.12);
- When the restriction is in the $y$ displacement, the $x$ and $z$ rotations should also be restricted;
- When the restriction is in the $z$ displacement, the $x$ and $y$ rotations should also be restricted;

Figure 6.12 represents the x-direction boundary condition as an example of the changes that must be done when using shell elements.

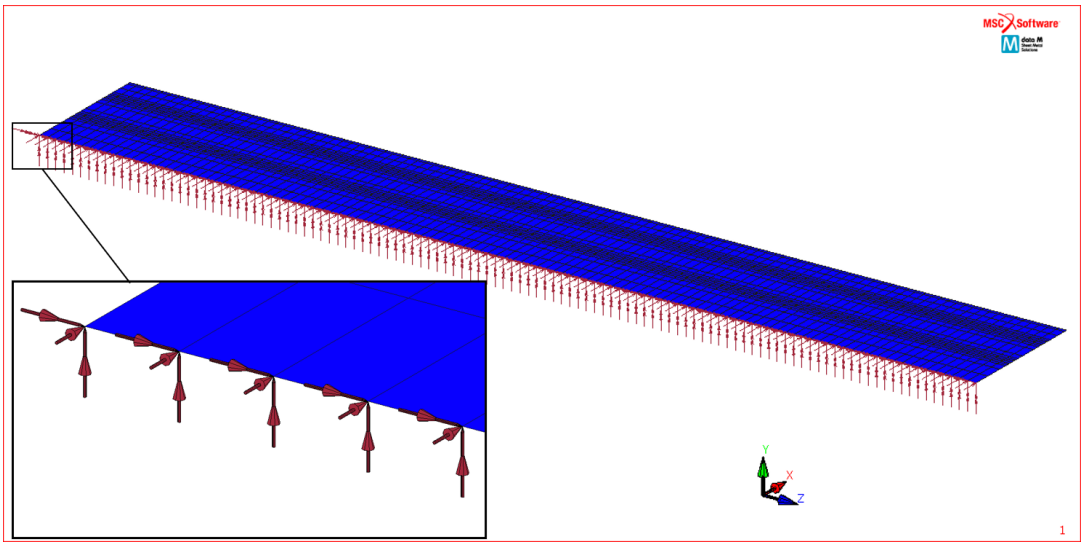



Figure 6.12: x-direction boundary condition for the models with shell elements

### 6.1.6 Contact definition

Friction is the resistant force to a relative motion of surfaces in contact sliding against each other [Wang et al. (2018)]. For this simulation, friction between the rolls and the sheet was disregarded. Thus, the rolls are not driven and act as rigid static bodies. A null friction condition was chosen, as it is an acceptable approximation for this roll forming model and it decreases the computation times [Safdarian and Moslemi Naeini (2015)].

Based on results from Section 5.6, the node to segment contact method was used with a 0.9 contact bias factor and a smooth boundary condition of the meshed sheet.

## 6.2 Results and discussion

In order to assess the quality of the results yielded by each element, several different parameters were analyzed. Most of them have been mentioned in Section 4.3.1. The analysis was planned to cover the limitations of the different element formulations, the different forming mechanisms, and the defects that can occur in the product.

The reasoning behind each conducted analysis, as well as the methodology used to collect results, are summarized in Table 6.3.

Table 6.3: Parameters analyzed during the study of the numerical simulation of a roll forming process

| Study | Why is it relevant? | Methodology |
|---|---|---|
| **Double-sided contact** | Double-sided contact is believed to be a threat to the use of shell elements | The roll gaps were modified in order to induce double-sided contact. The contact status, contact forces, thickness reduction and computation time were analyzed for the model with one layer of solid elements and for the model with thick shell elements with 5 integration layers |
| **Lateral edge contact** | The out-of-plane forces involved in lateral edge contact can be a threat to shell elements | The contact status and contact force was analyzed for an increment with lateral edge contact, for the models with 1 and 4 layers of solid elements and for the model with thick shell elements with 5 integration layers |
| **In-plane shear stress** | In-plane shear stresses are prone to appear in the sheet when there is a harsh width reduction between two stations | Top view snapshots of the in-plane shear stresses contour bands were taken for all the models in Station 3 |
| **Bending angles and springback** | Elastic recovery of the material influences the final angles of the bends | The angles of the two bends of the profile were measured in the last station in a cross-section exactly after the plane of the last roll and in a stationary area after cut-off |
| **End flare** | The release of residual stresses can have a geometrical impact in the cut-off ends of the profile, originating end flare | The end flare was calculated by measuring the angles after cut off at the ends of the sheet and at a stationary zone. Residual stresses were studied in order to understand their influence in end flare |
| **Total Equivalent Plastic Strain** | The Total Equivalent Plastic Strain is a good indicator of the material's plastic yielding, which generally occurs in the areas of the bends | The Total Equivalent Plastic Strain values were collected in the center of the two bends for the top, bottom and middle layer of the sheet. |
| **Edge wave** | Edge wave can be caused by high longitudinal strains in the edge of the sheet, induced by longitudinal bending of the profile and different flow lengths of the material. | The critical station was determined by analyzing the peak values of the longitudinal strain distribution over time, for the edge of the sheet. |
| **Thickness** | Thinning of the sheet can occur on the bend lines, altering the geometry of the cross-section | The results of the models with shell elements were mapped to a model with one layer of solid elements, so that the cross-section views of the thickness contour-bands could be analyzed. The snapshots of the cross-sections were taken in a stationary zone before cut-off. |
| **Computation time** | In an industrial context there is the need to obtain simulation results as fast as possible | The computation time was analyzed for the different models |

### 6.2.1 Double-sided contact

As previously mentioned in Section 2.1.1.5, through-thickness compression is prone to occur in some areas of the roll forming process, which can induce double-sided contact. Due to the unstable results obtained for the shell elements during the single element test in Section 5.1, the double-sided contact had to be tested in the context of roll forming. Only two models were simulated. One used thick shell elements with 5 integration layers to validate the results for all the shell elements. The other used one solid element through the thickness to serve as a reference.

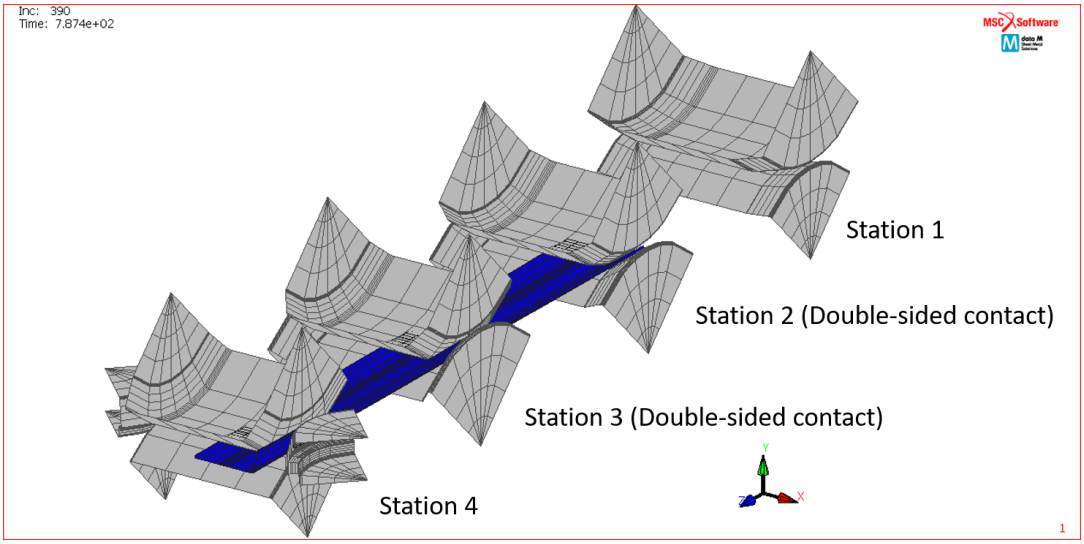



Figure 6.13: Isometric view of the first stations for the roll forming model with induced double-sided contact

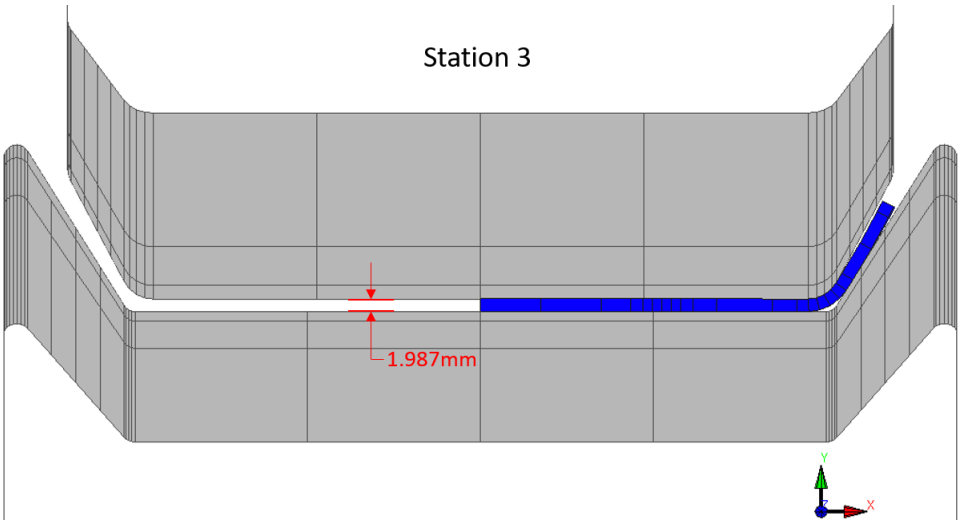
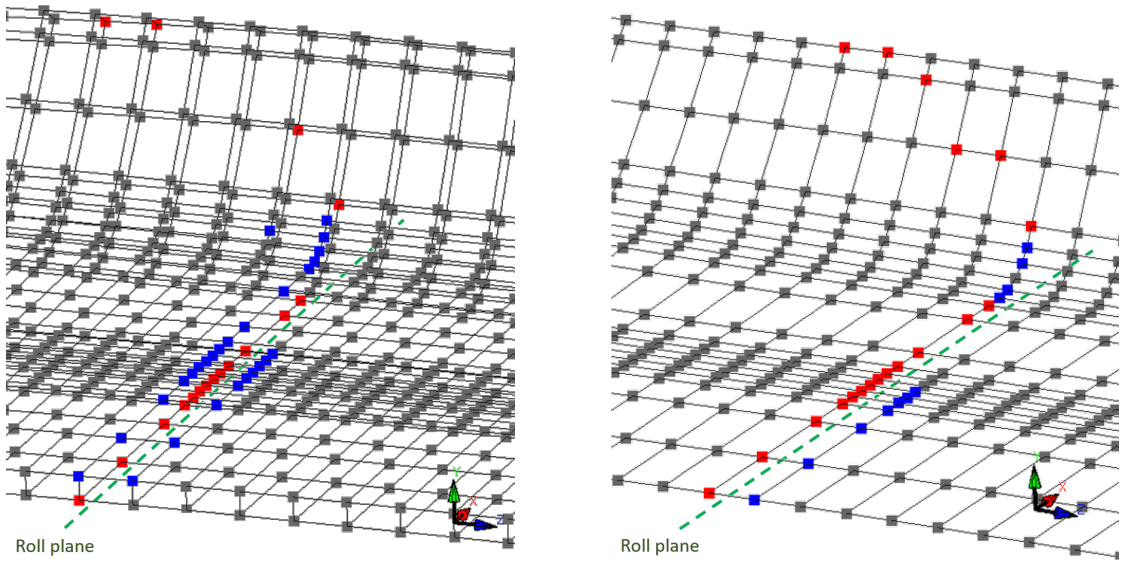



Figure 6.14: Cross-section view of the sheet in Station 3 evidencing a roll gap of 1.987*mm*, which is 0.013*mm* smaller than the sheet thickness of 2.000*mm*

Since double-sided contact did not occur for the standard model of the C-shaped profile, for

this section, the model was slightly modified in order to better study this phenomenon. Therefore, Station 2 and Station 3 (Figure 6.13) have a roll gap of $1.987mm$, which is $0.013mm$ smaller than the sheet thickness (Figure 6.14). The smaller roll gap in Station 2 and Station 3 will force double-sided contact, inducing a slight thickness reduction in the sheet.

Figure 6.15 shows the phenomenon of double-sided contact in Station 3, where each node outputs a value for the contact touched body nodal quantity indicating which roll they are in contact with. The position of the nodes in relation to the roll plane is evidenced in Figure



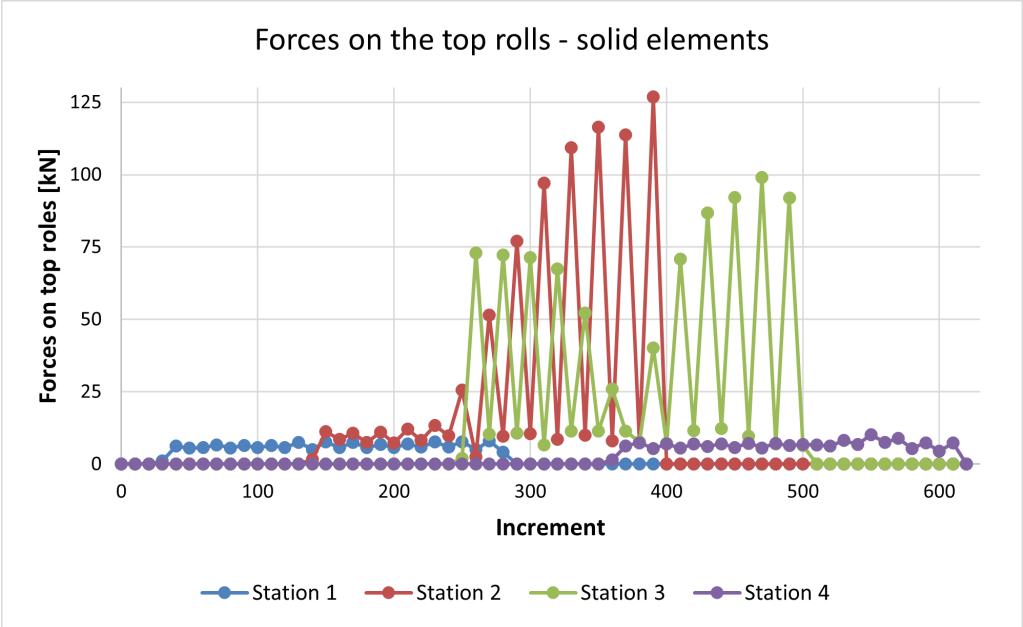

(a) Solid - 1 element through the thickness

(b) Thick shell - 5 integration layers

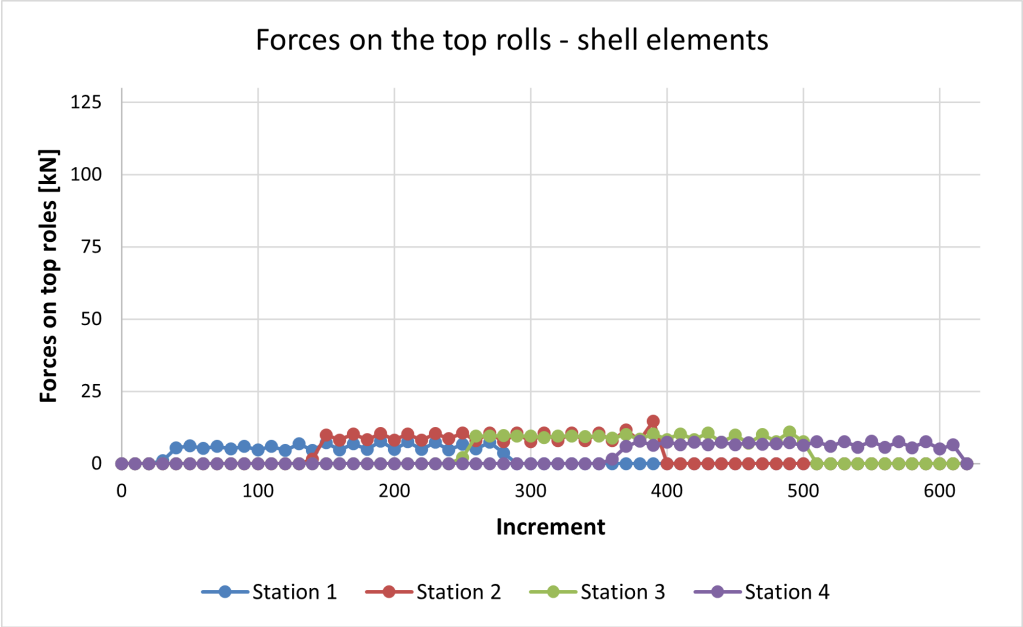
Figure 6.15: Output of Contact Touched Body via coloured symbols in Station 3 (roll gap smaller than sheet thickness). Nodes in blue are in contact with the top roll; nodes in red are in contact with the bottom roll.

It can be observed that, for the solid element, some of the top nodes are in contact with the top roll, whereas some of the bottom nodes are in contact with the bottom roll. On the other hand, the contact on the shell model shows that its nodes will alternate contact between the top and bottom roll, with no apparent pattern. This reflects one of the behaviors observed during the single element test of the double-sided contact, as it is verified that the same element can have some nodes in contact with a top surface and some nodes in contact with a bottom surface.

The forces in the top rolls for the first four stations are present in Figure 6.16, obtained by outputting the forces in the corresponding contact bodies. Only the first four stations were analyzed as they provide good insights on the representation of forces for two stations with double-sided contact and two stations without double-sided contact. Table 6.4 summarizes the peak values of the forces on the top rolls.




(a) Model with solid elements - 1 element through the thickness




(b) Model with thick shell elements - 5 integration layers

Figure 6.16: Forces on the top rolls for the first four stations. In Station 1 and Station 4 double-sided contact does not occur; in Station 2 and Station 3 double-sided contact occurs

When there is no double-sided contact, the shell element accurately reflects the forming forces involved. On the stations with double-sided contact, the model with shell elements considers some additional forces when compared to the stations without double-sided contact. However, the shell element still underestimates the high forces involved in this contact situation, which are expected to exist when there is a forced thickness reduction of the sheet resulting from a compressive mode in the thickness direction. On the other hand, the solid element yields significantly higher forces

when in the presence of double-sided contact.

Table 6.4: Peak value of the forces on the top roll [$kN$]. Station 1 and Station 4 have a roll gap bigger than the sheet thickness; Station 2 and Station 3 have a roll gap smaller than the sheet thickness, which induces double-sided contact

| | **Station 1** | **Station 2** | **Station 3** | **Station 4** |
|---|---|---|---|---|
| **Solid - 1 element through the thickness** | 8.083 | 126.982 | 98.987 | 10.094 |
| **Thick shell - 5 integration layers** | 7.702 | 14.640 | 10.897 | 7.702 |

It is also important to mention the oscillating behavior of the forces in the rolls, which is even more noticeable for the model with solid elements. This is due to the fact that with the movement of the nodes, and since the data for the forces is only collected every ten increments, the nodes are never exactly on the roll plane, as seen in Figure 6.17. This could be solved by either refining the mesh along the length of the sheet or by collecting data for the forces for every increment. Both suggested solutions would increase computational costs.

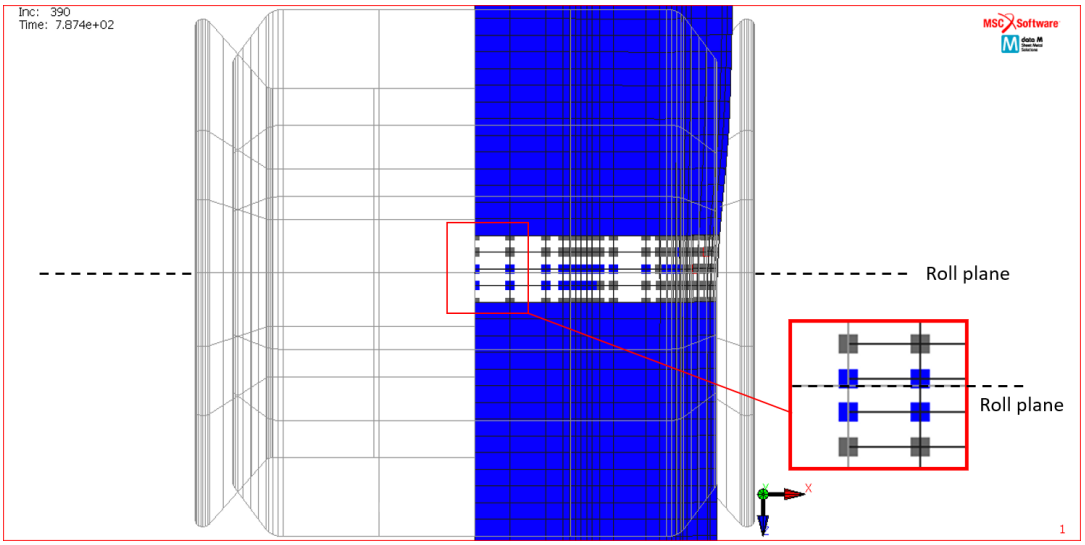



Figure 6.17: Position of the roll plane in relation to the nodes in contact for the model with solid elements in Station 3

Concerning the results of the thickness reduction, which was expected to occur due to the fact that the roll gap is 0.0130$mm$ smaller than the sheet thickness, these are summarized in Table 6.5. The values were collected in increment 390 (as seen in Figure 6.13) where the sheet is in contact with Station 2, Station 3, and Station 4, to guarantee a steady-state of the sheet Mahajan et al. (2018). The location of the thickness measurements was a flat zone of the profile, which corresponds to Zone A in Figure 6.18, during and after double-sided contact in Station 3.

Table 6.5: Thickness reduction [*mm*] of the sheet on Zone A (Figure 6.18). Results collected for increment 390 in Station 3, which has double-sided contact.

| | **Thickness reduction during contact [mm]** | **Thickness reduction after contact [mm]** |
|---|---|---|
| **Solid - 1 element through the thickness** | 0.0070 | 0.0050 |
| **Thick shell - 5 integration layers** | 0.0001 | 0.0001 |

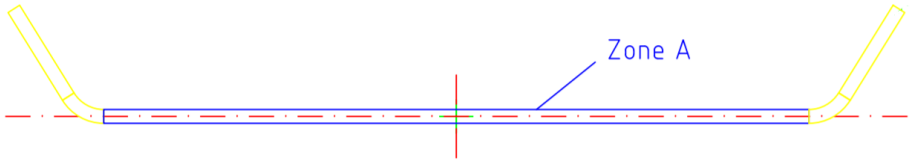



Figure 6.18: Expected profile cross-section in Station 3, where the values of thickness reduction were taken

In line with what was seen during the single element tests, the shell element disregards the thickness reduction induced by a compressive mode in the thickness direction. For the solid element, during contact, a thickness reduction of 0.0070*mm* was measured, a value 54% smaller than the 0.0130*mm* that could be expected. This is explained by the fact that the nodes in which the value of thickness was collected are not exactly on the roll plane, but slightly after the roll plane. Therefore, in these nodes, a portion of the elastic return of the material has already occurred.

Lastly, the computation time was analyzed and can be seen in Table 6.6. The existence of double-sided contact in just 2 of the 13 stations of the roll forming line induces a 7.5% increase in the computation time of the model with solid elements. This impact would be harsher if even more stations had double-sided contact. In turn, the model with shell elements does not see a significant increase in CPU time.

Table 6.6: Computation time for the simulation of the models with and without double-sided contact

| | **CPU Time [s]** | **CPU Time [min]** |
|---|---|---|
| **Solid - 1 element through the thickness - without double-sided contact** | 3854 | 64.2 |
| **Thick shell - 5 integration layers - without double-sided contact** | 3501 | 58.4 |
| **Solid - 1 element through the thickness - with double-sided contact** | 4166 | 69.4 |
| **Thick shell - 5 integration layers - with double-sided contact** | 3528 | 58.8 |

To sum up, the elements have different behaviors when in the presence of double-sided contact. The model with solid elements has an increase in computation time when in the presence of

double-sided contact. Even though the model with shell elements manages to converge, the model cannot reproduce the induced thickness reduction and underestimates the forces in the rolls, disregarding the compressive stresses in the thickness direction. Therefore, shell elements are not a viable alternative for the simulation of double-sided contact and through-thickness compression, present in additional processes that can be integrated into the roll forming line such as coining and grooving.

### 6.2.2 Lateral edge contact

In section 5.4, it was concluded that the shell elements were not expected to have issues yielding lateral edge contact, even with the concerns of DIANA FEA (2017) that shell elements were not suitable for the simulation of out-of-plane loads. In order to confirm the result in a roll forming context, the model with thick shell elements with 5 integration layers was analyzed.

In the simulation of the C-profile, lateral edge contact is prone to occur in some areas of the roll forming line, more specifically in Station 11.

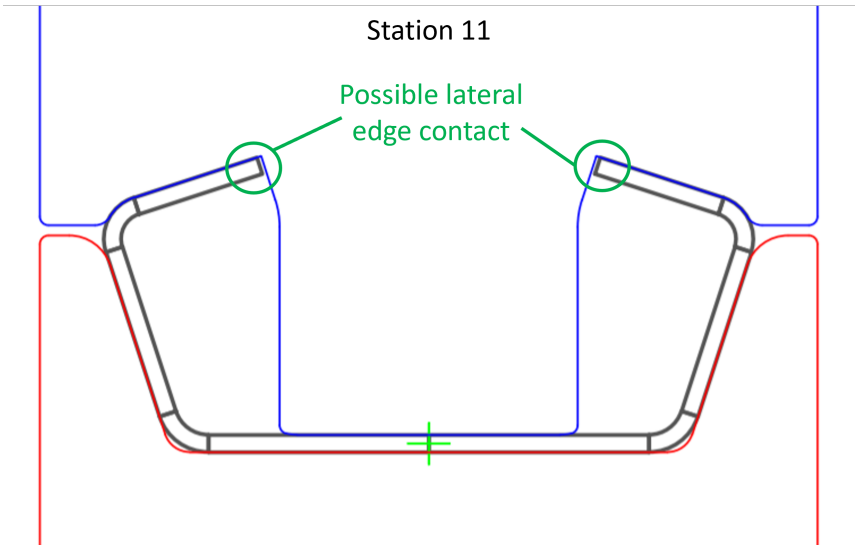



Figure 6.19: Profile and rolls in Station 11. Profile in black, top roll in blue, bottom roll in red

As it can be seen in Figure 6.19, some contact between the edge of the sheet and the top roll might occur in case of an overbending of the profile. Figure 6.20 shows the contact status of the nodes, where the red zones indicate that a node is establishing contact with a roll and indeed a situation in which one node of a shell element is subjected to lateral edge contact can be detected.

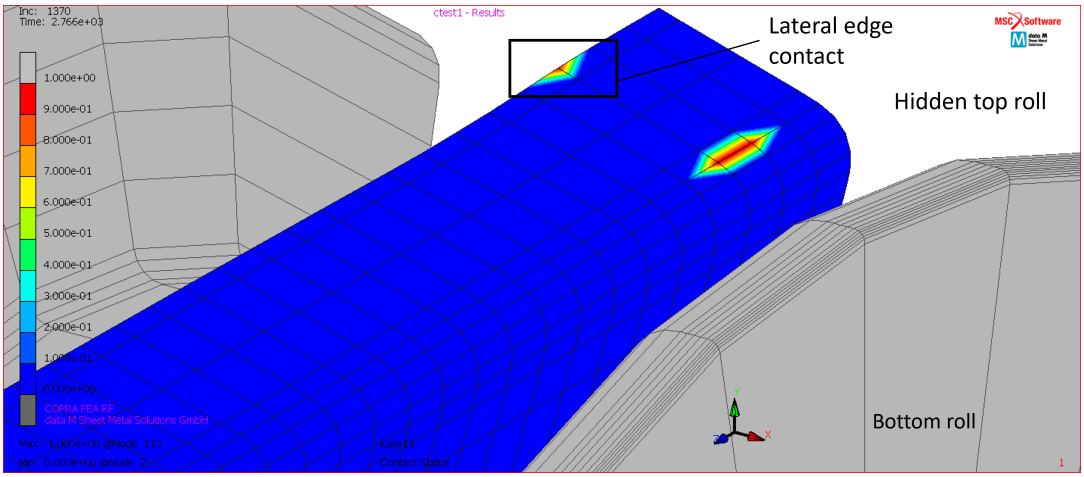



Figure 6.20: Situation of edge contact on a shell element in station 11. Contour bands highlight the nodes in contact

Similarly to the single element test in Section 5.4, the node is subjected to a lateral contact force, with a direction perpendicular to the sheet edge and parallel to the shell plane, as Figure 6.21 shows. The magnitude of the contact force $F_c$ was calculated as:

$$F_c = \sqrt{F_{cX}^2 + F_{cY}^2 + F_{cZ}^2} \tag{6.2}$$

where $F_{cX}$, $F_{cY}$, and $F_{cZ}$ correspond to nodal quantities of the contact normal force in the X, Y and Z directions respectively.

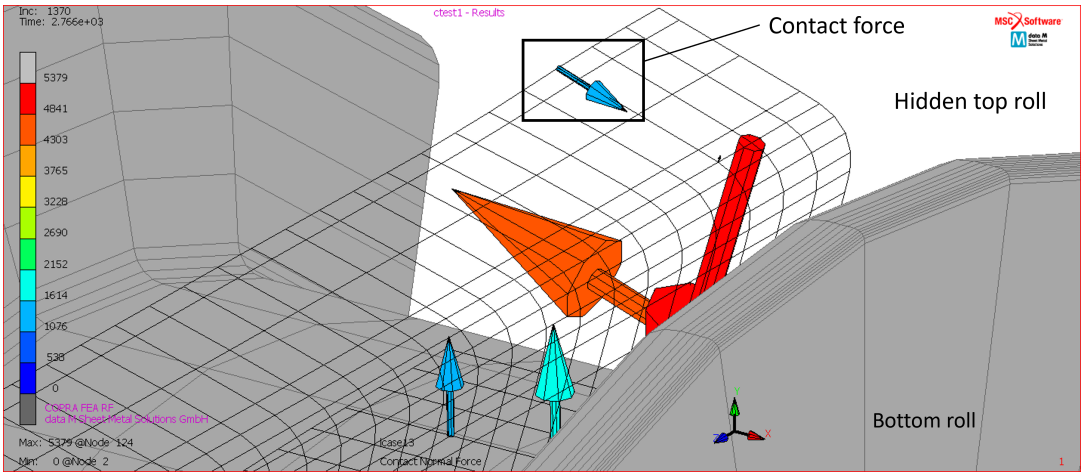



Figure 6.21: Situation of edge contact on a shell element. Vectors indicate the contact forces in each node

For the model with thick shell elements with 5 integration layers, the magnitude of the contact force in the node is $1.268kN$, smaller than the value of $1.495kN$ measured for the same node in the reference model (model with 4 layers of solid elements), but higher than the value of $1.182kN$ for the model with 1 layer of solid elements. Considering the results for the edge contact test in

Section 5.4, these differences are most likely associated with geometrical differences in the profile and are not a reflex of a limitation in the element formulation to establish out-of-plane contact. It is also important to mention that this contact occurred in the tail portion of the sheet which is discarded at the end of the simulation through the cut-off, as it does not reflect the steady-state behavior of the roll forming process [Mahajan et al. (2018)].

To sum up, models with both shell and solid elements can establish contact on the edge of the sheet. Some differences can arise in the magnitude of the contact force.

### 6.2.3 In-plane shear stress

As explained in Section 2.1.1.3, in-plane shear stresses $\tau_{12}$ are prone to appear in the profile, especially when there is a harsh width reduction between two stations. During the single element uniaxial test in Section 5.3, with only one element, the shell with reduced integration and the solid shell did not yield in-plane shear. It was hypothesized that, for coarse meshes, there is the possibility of an underestimation of $\tau_{12}$ for elements with reduced integration.

In order to confirm the mentioned hypothesis and to validate it in the roll forming context, a snapshot of the in-plane shear stresses was taken. By the means of contour bands visualization, the magnitude and distribution of in-plane shear in the top layer of the sheet can be analyzed. These snapshots were taken in Station 3, as the first stations are often the most critical in terms of high in-plane shear stresses [Mohd Saffe et al. (2014)]. Similar to when measuring the forces in Section 6.2.1, the snapshot was taken in increment 390 to guarantee steady-state properties.

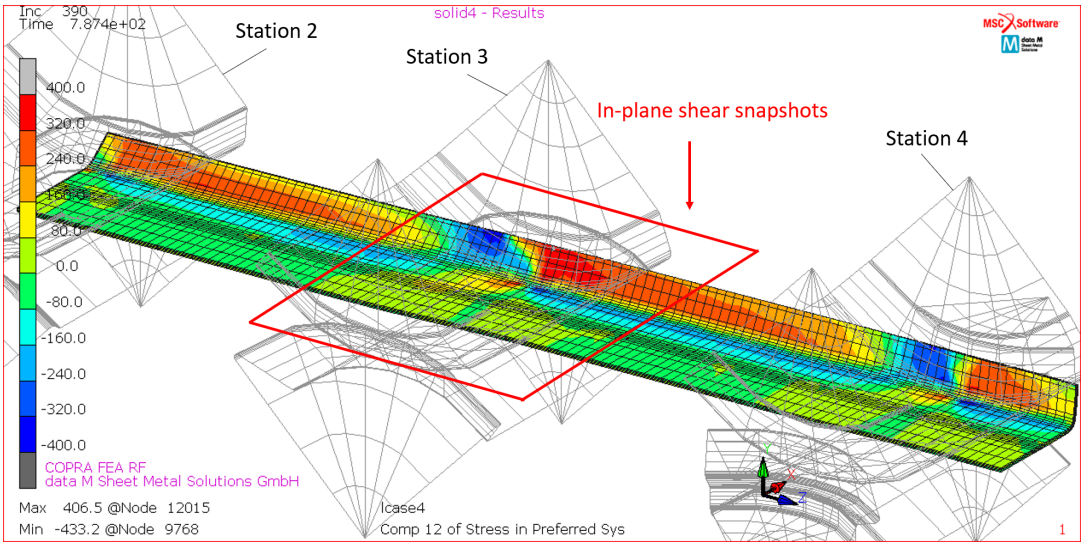



Figure 6.22: Isometric view of the in-plane shear in the model with 4 layers of solid elements. Sheet is in contact with rolls in 3 stations: Station 2, Station 3 and Station 4

Figure 6.22 and Figure 6.23 show the in-plane shear for the model with 4 layers of solid elements, when the sheet is between Station 2 and Station 4. The deformation and width reduction of the sheet when it enters Station 3, which is responsible for the induced $\tau_{12}$, can be visualized in Figure 6.23.

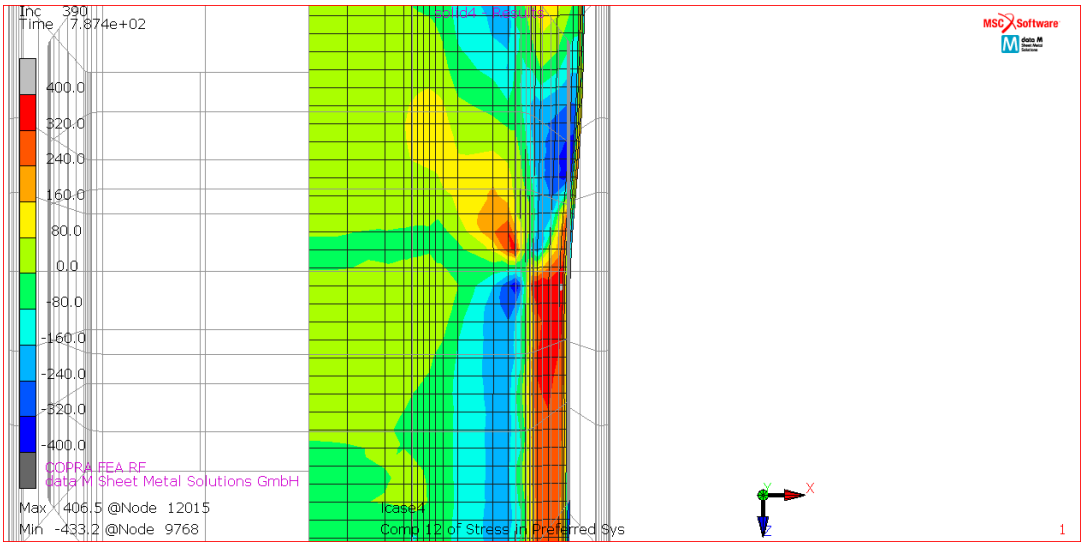



Figure 6.23: Station 3 top view of the in-plane shear in the model with 4 layers of solid elements. Results presented in a deformed mesh

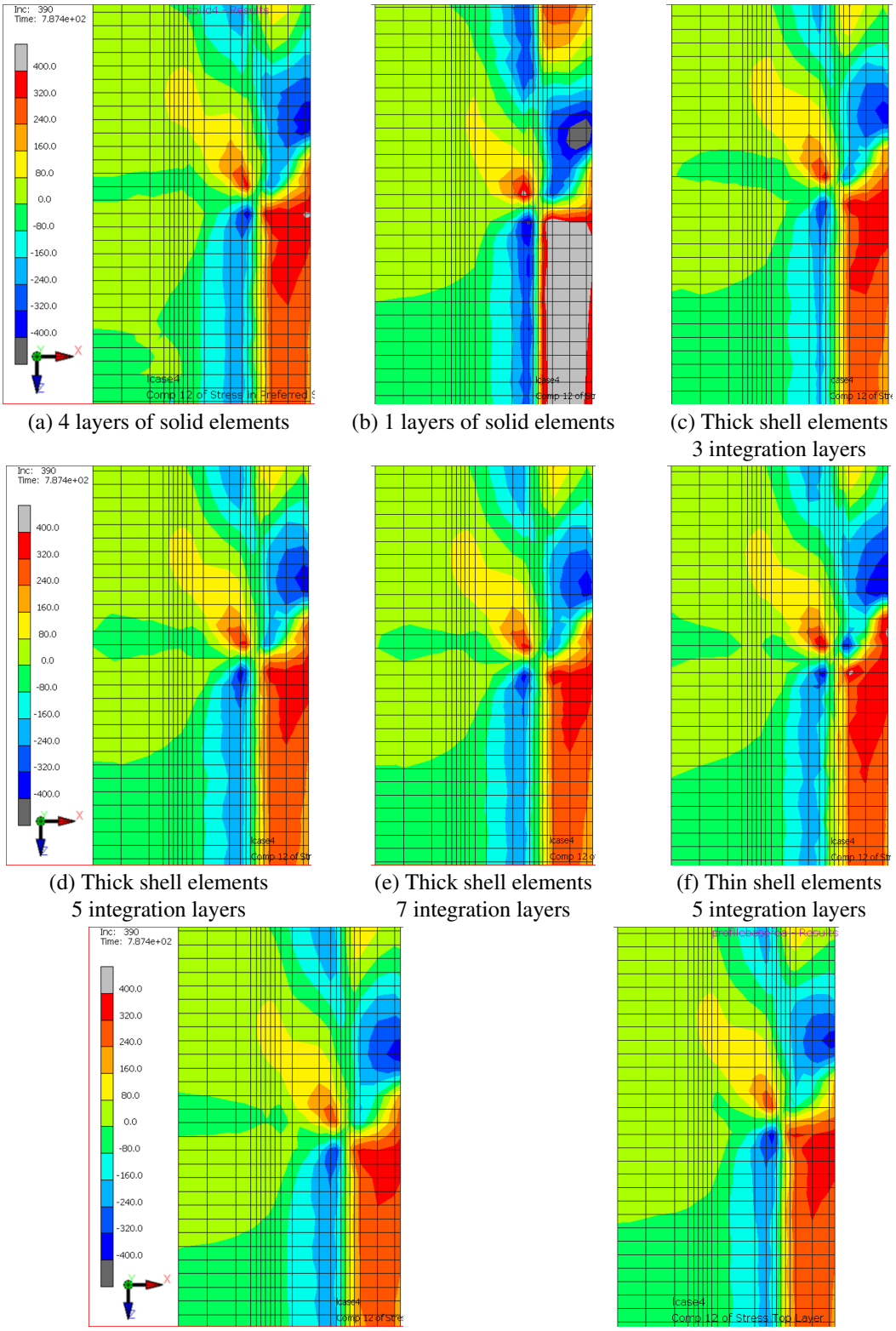
A top view snapshot was taken for all the models. The results of the in-plane shear were visualized in the original undeformed sheet, in order to allow an easier comparison of the contour bands.

Analyzing the different models in Figure 6.24, it can be verified that the model with only 1 layer of solid elements demonstrates an over stiffing behavior, yielding in-plane shear values approximately 30% higher when compared with the reference model, which is evidenced by the black and grey areas of the contour bands.

Moreover, it is important to mention a slight underestimation of the in-plane shear for the solid shell and for the shell with reduced integration. The elements present in-plane shear peak values around 10% lower than the peak values of the reference model. The slight underestimation of $\tau_{12}$ for the elements with reduced integration is in line with the results and hypothesis taken from the single element test in Section 5.3. The use of an even more refined mesh is expected to bring the in-plane shear results of the elements with reduced integration even closer to the reference results.

To sum up, it can be concluded that:

- One solid element through the thickness overestimates in-plane shear;
- Reduced integrated elements slightly underestimate in-plane shear. The coarser the mesh, the bigger the impact of this underestimation;
- In-plane shear is, indeed, higher in the edge portions of the sheet, which agrees with Halmos (2006);




(a) 4 layers of solid elements

(b) 1 layers of solid elements

(c) Thick shell elements
3 integration layers

(d) Thick shell elements
5 integration layers

(e) Thick shell elements
7 integration layers

(f) Thin shell elements
5 integration layers

(g) Shell elements with reduced integration
5 integration layers

(h) Solid shell elements
5 integration layers

Figure 6.24: In-plane shear on the top layer of the sheet for the different models in Station 3. Results presented in a undeformed mesh

### 6.2.4 Bending angles and springback

In order to analyze the geometric accuracy of each of the models, the angles of the bends were measured. The results of the angles and springback taken in Section 5.6 for the air bending test had to be validated in the roll forming context since roll forming has more forming mechanisms than just transversal bending.

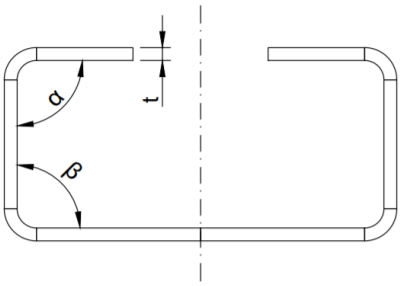



Figure 6.25: C-Profile cross-section indicating measured angles $\alpha$ and $\beta$

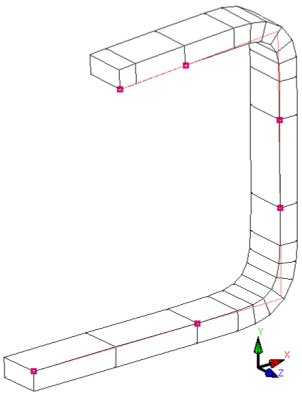


Figure 6.26: Auxiliary lines for angle measurement

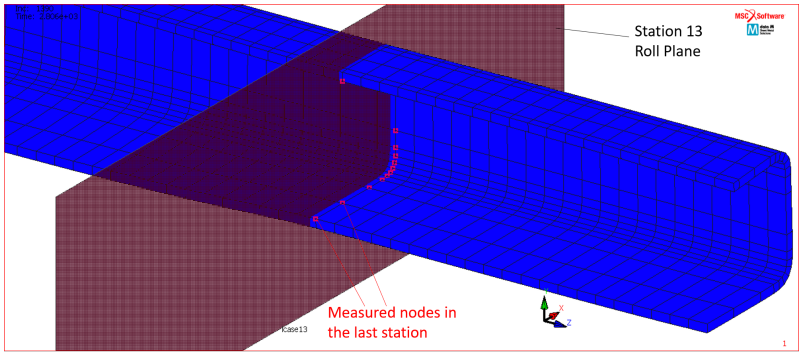



Figure 6.27: Angle measurement in the last station

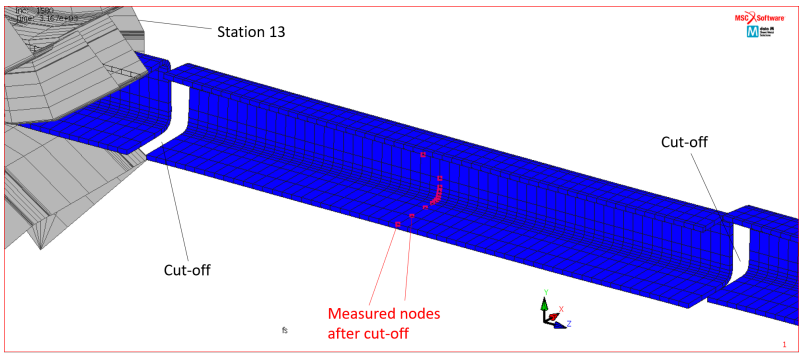



Figure 6.28: Angle measurement after cut-off

The measured angles can be seen in Figure 6.25. The angles were measured in two different situations: in the last station, in a cross-section exactly after the plane of the last roll (Figure 6.27); and after the cut-off, in a stationary area in the middle of the final product, so that the angles would not be influenced by end flare phenomenona (Figure 6.28). In order to measure the angles, straight lines were created between the highlighted nodes in Figure 6.26, and the lines were then extended in order to intersect each other, allowing the angle to be measured directly in Marc.

Table 6.7 comprises the results of the measured angles in the two mentioned situations, and the resulting value of springback. The springback was calculated as:

$$Springback = \theta_f - \theta_i \tag{6.3}$$

- $\theta_f$ is the angle after cut-off measured in a stationary zone
- $\theta_i$ is the angle in the last station

Table 6.7: Results of the measured angles $\alpha$ and $\beta$, for the different models with different element types. Springback calculated using the difference between the angles after cut-off and in the last station. Model with 4 layers of solid elements used as reference

| | In the last station | | | | After cut-off (stationary zone) | | | | | |
|---|---|---|---|---|---|---|---|---|---|---|
| | Alfa [°] | Beta [°] | Alfa difference to reference [°] | Beta difference to reference [°] | Alfa [°] | Beta [°] | Alfa difference to reference [°] | Beta difference to reference [°] | Springback Alfa [°] | Springback Beta [°] |
| Solid - 4 Layers of elements | 87.190 | 89.847 | 0.000 | 0.000 | 88.903 | 90.118 | 0.000 | 0.000 | 1.713 | 0.271 |
| Solid - 1 Layer of elements | 89.312 | 89.783 | 2.121 | -0.063 | 90.038 | 90.382 | 1.135 | 0.264 | 0.726 | 0.598 |
| Thick Shell - 3 Integration Layers | 88.050 | 89.721 | 0.860 | -0.125 | 88.434 | 89.195 | -0.470 | -0.923 | 0.384 | -0.526 |
| Thick shell - 5 Integration Layers | 87.235 | 89.798 | 0.045 | -0.049 | 89.557 | 90.766 | 0.653 | 0.648 | 2.322 | 0.968 |
| Thick shell - 7 Integration Layers | 87.505 | 89.814 | 0.315 | -0.032 | 89.897 | 90.445 | 0.994 | 0.327 | 2.392 | 0.631 |
| Thin Shell - 5 Integration Layers | 88.575 | 89.860 | 1.385 | 0.013 | 90.678 | 91.207 | 1.775 | 1.090 | 2.103 | 1.348 |
| Shell with reduced Integration - 5 Integration Layers | 87.210 | 89.597 | 0.020 | -0.250 | 89.288 | 90.773 | 0.385 | 0.655 | 2.078 | 1.176 |
| SolidShell - 5 Integration Layers | 85.973 | 89.606 | -1.217 | -0.241 | 88.084 | 89.911 | -0.819 | -0.207 | 2.111 | 0.305 |

From a first analysis, one can verify that it is easier to obtain geometry accuracy for the angle $\beta$ than for the angle $\alpha$, with all the models yielding results close to the reference. These can be explained by analyzing the forming sequence in Figure 6.29.

The fact that the $\alpha$ bent is done in two different moments and that this bend is inactive for four stations (from Station 6 to Station 9) makes errors more prone to propagate in the model, mainly due to the in-plane shear stresses which are induced and released from the profile [Panton et al. (1994)]. Being located at the edge of the sheet also makes this bent more prone to additional forming mechanisms besides the desired transversal bending. All these factors will contribute to dispersion in the measured values of the angle $\alpha$. The resistance to displacements of the model with only one solid element through the thickness, which shows a bigger bending angle, agrees with the over-stiffing behavior detected in Section 6.2.3. The thin shell and the solid shell also fail to accurately represent this bend. In general, the models with thick shells (including the model with shells with reduced integration) show good reliability for this particular bend.

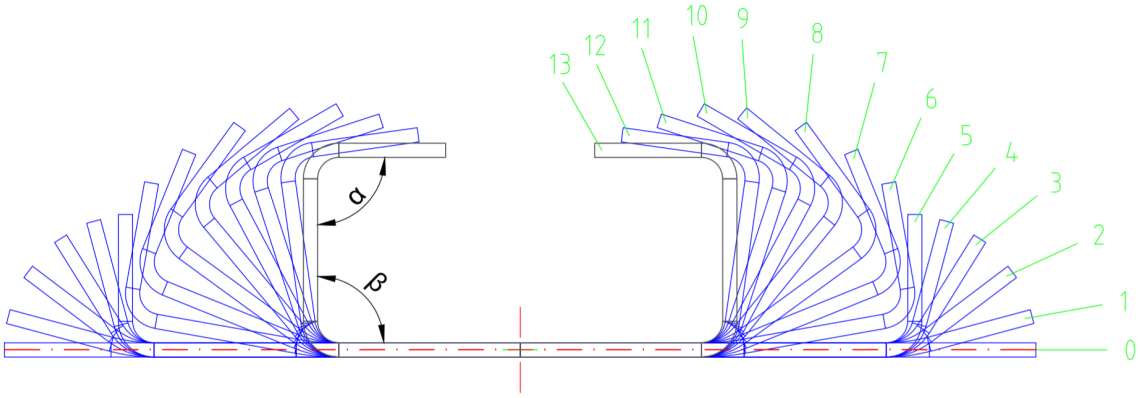



Figure 6.29: Flower diagram with the forming sequence of the C-Profile. $\alpha$ is formed until station 5, and is over bent between stations 10 and 13. $\beta$ is formed from station 6 until the end of the roll forming line.

On the other hand, $\beta$ is formed along eight different stations and is located near the center of the sheet, making it less prone to numerical errors derived from residual stresses. All the models represent this angle correctly before the cut-off.

After the cut-off, the material undergoes elastic recovery, and the angles are expected to increase. The model with thick shells with 3 integration layers presents a negative spring back value for $\beta$ and an extremely small value of springback for $\alpha$ when compared to the reference. This comes to show the need for at least 5 layers of integration when using shell elements in order to achieve an acceptable bending behavior. It is also notable the worse and bigger values of springback in angle $\beta$ for the models with shell elements when compared with the models with solid and solid shell elements.

The models, each with different element types, present different bending behaviors. The quality and accuracy of the results are different from model to model and also when analyzing different bends. It can be concluded that:

- The model with only one layer of solid elements has an over-stiffing behavior for the bend near the sheet edge;
- Using shell elements with only 3 integration layers gives a poor representation of springback, underestimating this phenomenon;
- For the bend near the sheet edge, thick shells and shells with reduced integration using 5 or more integration layers are a good option;
- For the bend near the center of the sheet, models with solid and solid shell elements are the best option. Thick shells, especially with 7 integration layers, can also be considered.

### 6.2.5 End flare

End flare is associated with the release of residual stresses during the cut-off and can have a geometrical impact in the cut-off ends of the profile in terms of bending angles, as mentioned in

Section 2.1.2.3. The end flare was studied by measuring the angles after the cut-off at the sheet lead and tail, areas that undergo additional deformation, and at a stationary zone in the center of the cut profile that does not undergo additional deformation (Figure 6.32). The end flare was calculated as:

$$End\,flare = \theta_{lead/tail} - \theta_{stationary} \tag{6.4}$$

with $\theta$ corresponding to the measured angle.

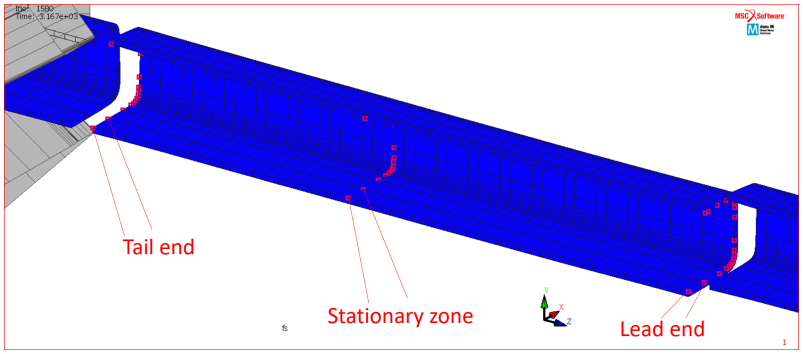



Figure 6.30: Locations where the angles were measured in order to calculate end flare

A positive value of end flare indicates flaring out in one of the bends, whereas a negative indicates flaring in.

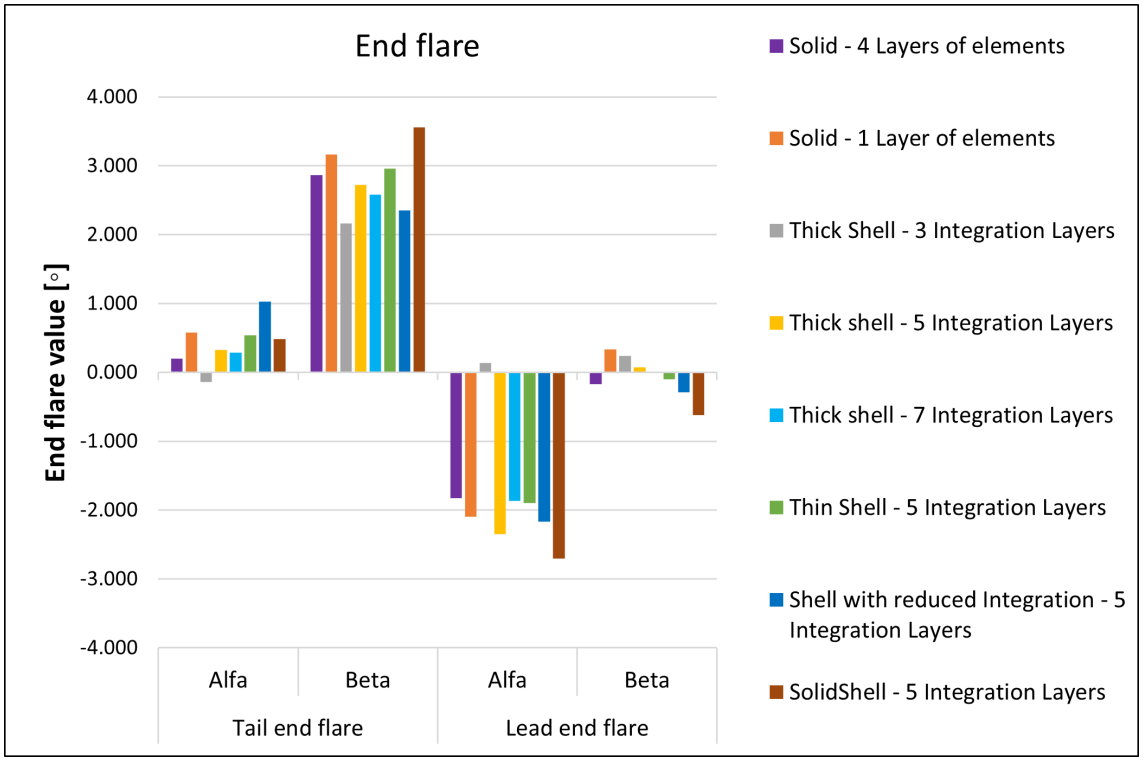



Figure 6.31: End flare values [°] for $\alpha$ and $\beta$ angles, at the tail and lead of the profile

Figure 6.31 shows that the $\alpha$ bend flares in at the lead end, and that the $\beta$ bend flares out at the lead end. As the end flare is associated with the release of residual stresses, mainly longitudinal stresses $\sigma_1$ and in-plane shear stresses $\tau_{12}$ [Moneke and Groche (2018)], the values of stresses in the profile before cut-off were also analyzed and can be seen in Figure 6.33 and Figure 6.34. The values of residual stresses were taken in a row of nodes in the top layer of the sheet in a stationary zone but before cut-off (Figure 6.32).

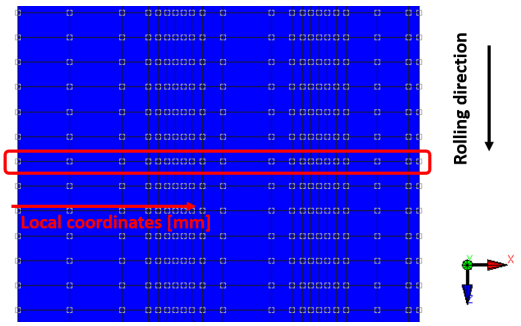



Figure 6.32: Row of nodes and corresponding local coordinates considered for Figure 6.33 and Figure 6.34

Based on the study of Moneke and Groche (2018), the general flare in of $\alpha$ at the lead is due to the positive values of in-plane shear stress $\tau_{12}$ in that region. The flare in overestimation of 0.88° for the model with solid shell elements could not be explained. The different behavior of the model with shell elements with just 3 integration layers can be explained by its small values of in-plane shear stress $\tau_{12}$ and by the positive values of longitudinal stress $\sigma_1$ which induce in the bend a tendency to flare out.

The general flare out of $\beta$ at the tail is mainly due to the negative values of longitudinal stress $\sigma_1$ in that region. The tendency of the model with solid shell elements to overestimate flare out of $\beta$ at the tail by 0.7° can be explained by the high magnitude of the negative longitudinal stress $\sigma_1$ in the area of the $\beta$ bend. Still at the tail, most of the models have residual values of flare out for the $\alpha$ bend. However, the model with shell elements with reduced integration present a flare out of 1.1°, behavior which could not be explained based on the stress distributions.

Lastly, the fully integrated models excluding the thick shell with 3 integration layers deviated only slightly from the reference model with 4 layers of solid elements, with deviations never larger than 0.5°. It should be highlighted that the model with thin shell elements, even if not accounting for transverse shear stresses $\tau_{23}$ and $\tau_{31}$, does not yield poor results proving that, indeed, the residual stresses $\sigma_1$ and $\tau_{12}$ have the biggest impact on end flare.

To sum up:

- Models with thick shell and thin shell elements with more than 5 integration layers, and with solid elements, correctly represent end flare;
- Models with elements with reduced integration correctly represent the direction of the end flare, but fail to accurately represent its magnitude;

- Models with shell elements using only 3 layers of integration cannot represent the end flare phenomenon and the release of residual stresses.

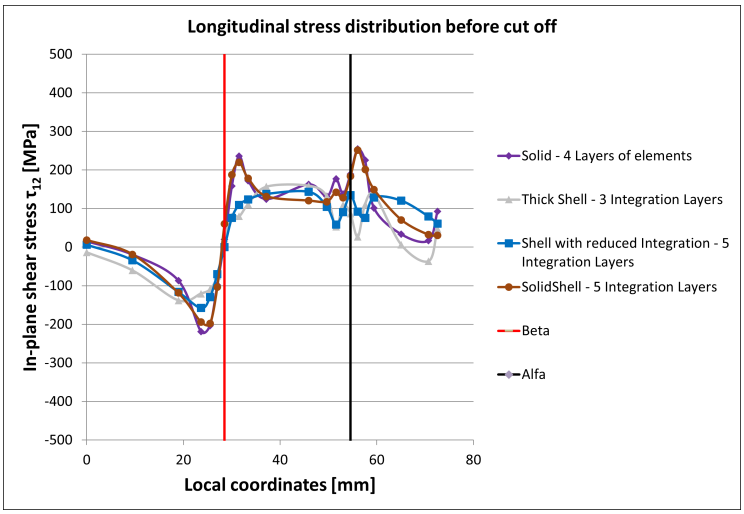



Figure 6.33: In-plane shear stress distribution before cut-off. Black and red lines signalize the center of $\alpha$ and $\beta$ bends

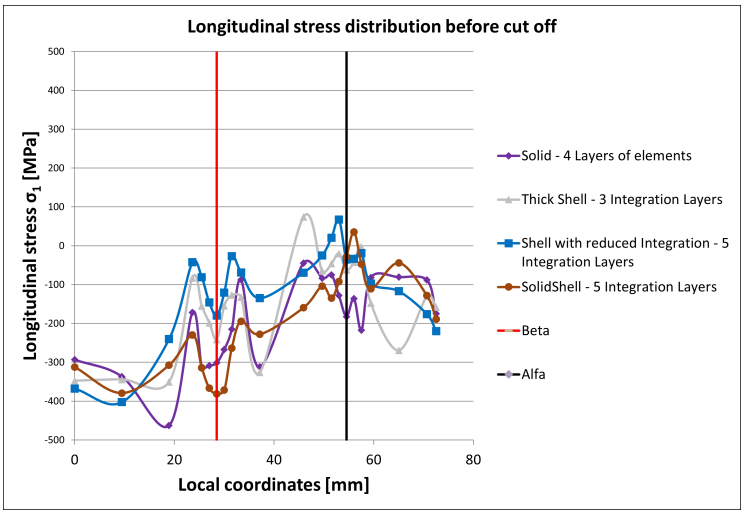



Figure 6.34: Longitudinal stress distribution before cut-off. Black and red lines signalize the center of $\alpha$ and $\beta$ bends

Due to the poor results when using shell elements with only 3 integration layers for all the parameters analyzed so far, and since the usage of this number of integration layers is not recommended by MARC (2021b), only 5 and 7 integration layers were studied for the parameters analyzed in the following sections.

### 6.2.6 Total Equivalent Plastic Strain

The Total Equivalent Plastic Strain shows the cumulative value of Equivalent Plastic Strain and will be analyzed at the end of the simulation in a stationary zone right before cut-off (Figure 6.35). As a scalar value that represents the magnitude of the accumulated plastic strain to which the material was subjected, considering strain in all the directions, this value is a good indicator of the material's plastic yielding.

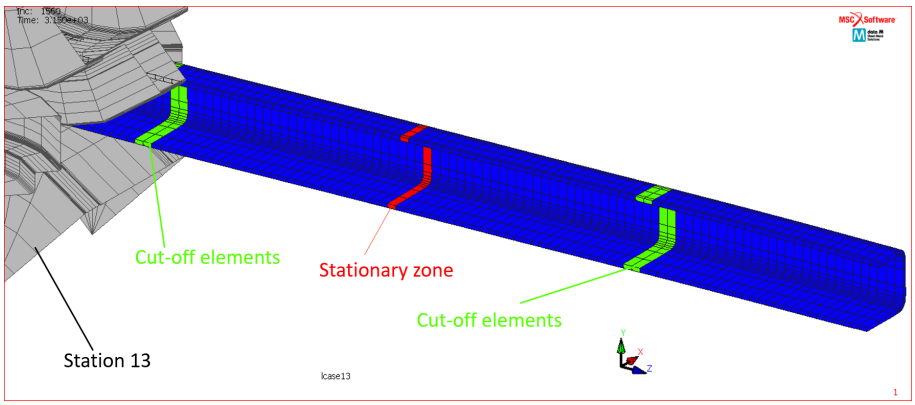



Figure 6.35: Sheet in the last increment before cut-off

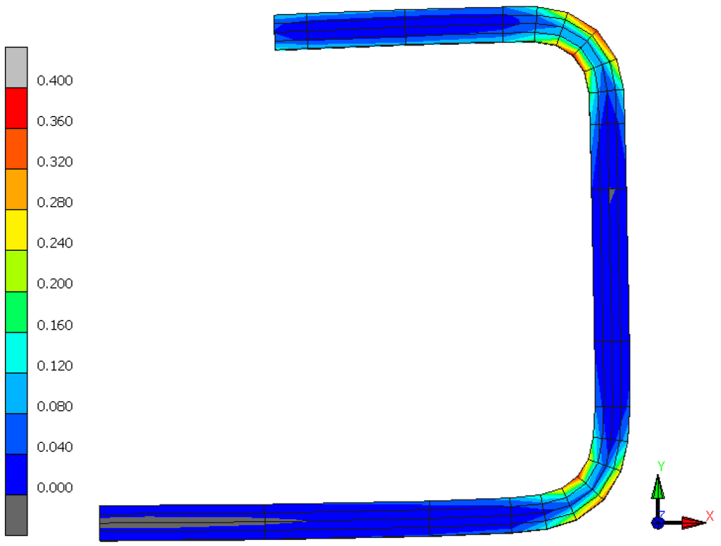



Figure 6.36: Cross-section view of the Total Equivalent Plastic Strain [-] for the model with four layers of solid elements

Analyzing the reference model in Figure 6.36, it can be seen that the Total Equivalent Plastic Strain is higher in the bending areas. The model with four layers of solid elements outputs higher values of Total Equivalent Plastic Strain in the outer layers around the bending areas, evidencing the existence of a neutral layer approximately in the middle layer of the sheet where the Total Equivalent Plastic Strain is significantly smaller and close to 0.

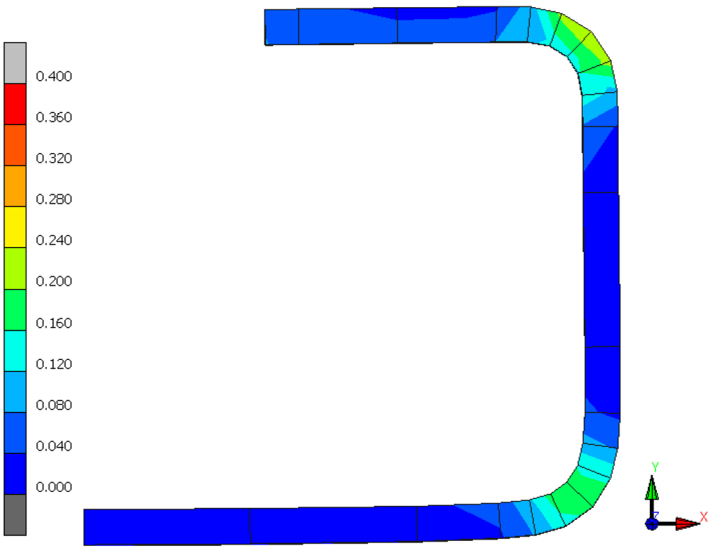



Figure 6.37: Cross-section view of the Total Equivalent Plastic Strain [-] for the model with one layer of solid elements

The neutral layer phenomenon was also studied in Section 5.6, and the model with one layer of solid elements was not able to correctly represent it due to the trilinear interpolation formulation of the solid element and to only having 2 integration layers across the thickness. Figure 6.37 shows a cross-section view of the Total Equivalent Plastic Strain for this model, and it is clearly visible that not only is the neutral layer phenomenon not represent, but there is also an underestimation of the Total Equivalent Plastic Strain.

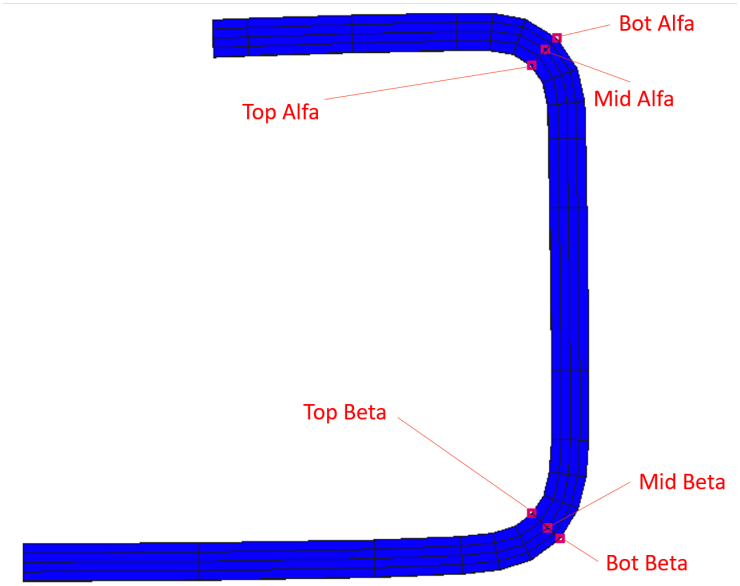



Figure 6.38: Cross-section view of the model with four layers of solid elements, signalizing the locations where the values of Total Equivalent Plastic Strain were collected for Table 6.8

Table 6.8 contains the values of Total Equivalent Plastic Strain for the top, middle and bottom layers in the center of the two bends $\alpha$ and $\beta$, as represented in Figure 6.38.

Table 6.8: Values of Total Equivalent Plastic Strain [-] for the top, middle and bottom layers in the center of the two bends $\alpha$ and $\beta$, as seen in Figure 6.38

| | Alfa | | | Beta | | |
|---|---|---|---|---|---|---|
| | Top | Middle | Bottom | Top | Middle | Bottom |
| Solid - 4 Layers of elements | 0.389 | 0.089 | 0.365 | 0.380 | 0.069 | 0.334 |
| Solid - 1 Layer of elements | 0.140 | - | 0.243 | 0.191 | - | 0.172 |
| Thick shell - 5 Integration Layers | 0.334 | 0.099 | 0.373 | 0.313 | 0.092 | 0.327 |
| Thick shell - 7 Integration Layers | 0.324 | 0.034 | 0.350 | 0.325 | 0.047 | 0.328 |
| Thin Shell - 5 Integration Layers | 0.355 | 0.040 | 0.358 | 0.361 | 0.056 | 0.339 |
| Shell with reduced Integration - 5 Integration Layers | 0.332 | 0.053 | 0.371 | 0.330 | 0.084 | 0.319 |
| SolidShell - 5 Integration Layers | 0.336 | 0.069 | 0.350 | 0.330 | 0.055 | 0.328 |

All the models with shell elements and the model with solid shell elements have similar results, managing to evidence the existence of the neutral layer where the Total Equivalent Plastic Strain is close to 0. These models yield accurate results for the bottom layer, with deviations not larger than 5%. For the bottom layers, these models underestimate the value of Total Equivalent Plastic Strain, with deviations of more than 10%.

To sum up:

- When using only one layer of solid elements, the neutral layer cannot be represented and the magnitude of plasticity in the bends is underestimated;
- Models with shell elements and with solid shell elements can represent the neutral layer and can correctly represent the through-thickness distribution of the Total Equivalent Plastic Strain. These models, however, slightly underestimate the plasticity in the top layer of the bends.

### 6.2.7 Edge wave

Elastoplastic buckling of the material near the sheet edge may lead to edge wave, an undesirable product defect [Halmos (2006)]. This phenomenon is mostly associated with high magnitudes of longitudinal strains, which are prone to appear in the profile, mainly due to longitudinal bending and to the different flow lengths of the material, as mentioned in Section 2.1.1.2 and Section 2.1.1.4. Therefore, the values of the longitudinal strain were analyzed for the nodes signalized in Figure 6.39.

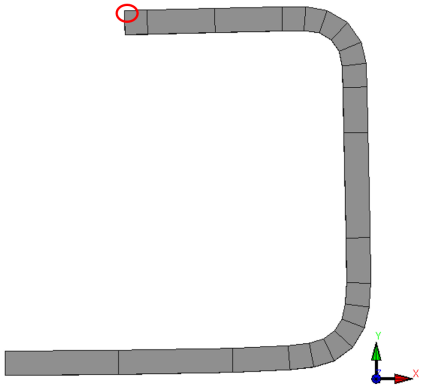


Figure 6.39: Cross-section of the profile indicating the row of nodes where the longitudinal strain was measured.

The history of the longitudinal strain allows to understand the evolution of longitudinal strain along the rolling direction and to detect the critical stations, in other words, the stations with a higher magnitude of the longitudinal strain and which are more likely to induce waviness. As seen in Figure 6.40, Station 2 and Station 5 are the critical stations for the model with 4 layers of solid elements.

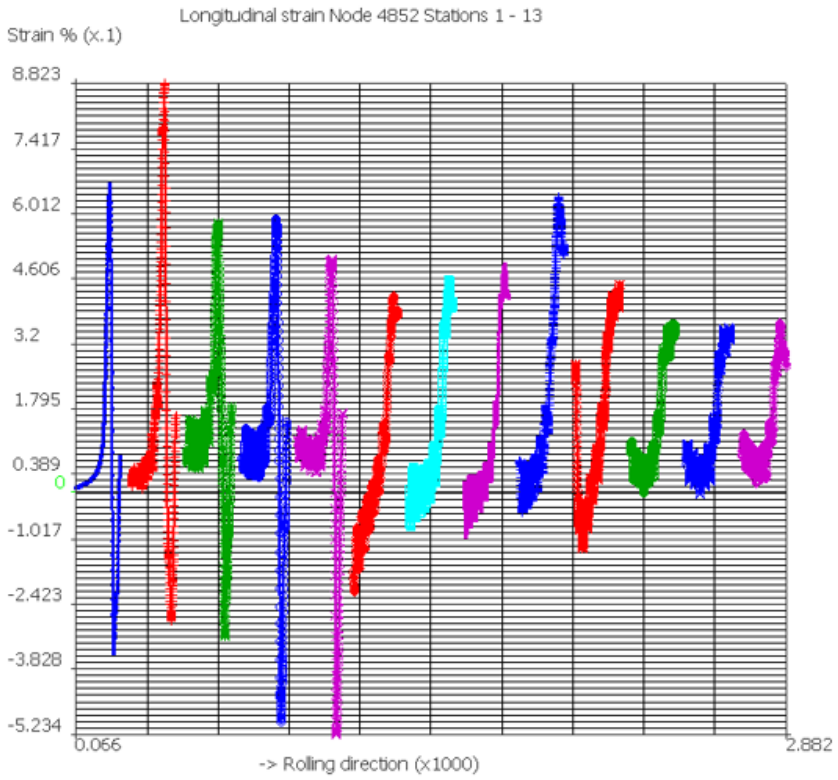



Figure 6.40: History of the longitudinal strain for a row of nodes in the bottom layer of the sheet edge, in the model with 4 layer of solid elements

As depicted in Figure 6.40, a high peak of longitudinal strain is reached in every station and

is followed by a sudden drop. This is caused by the longitudinal bending phenomenon mentioned in Section 2.1.1.4, and can be detected in Figure 6.41. The sheet is first bent when entering the station and the bottom layer will undergo high tensile stresses. When the sheet is bent back after some millimeters in the longitudinal direction down the roll forming line, this bottom layer will undergo compressive stresses and hence the sudden drop in the value of longitudinal stress.

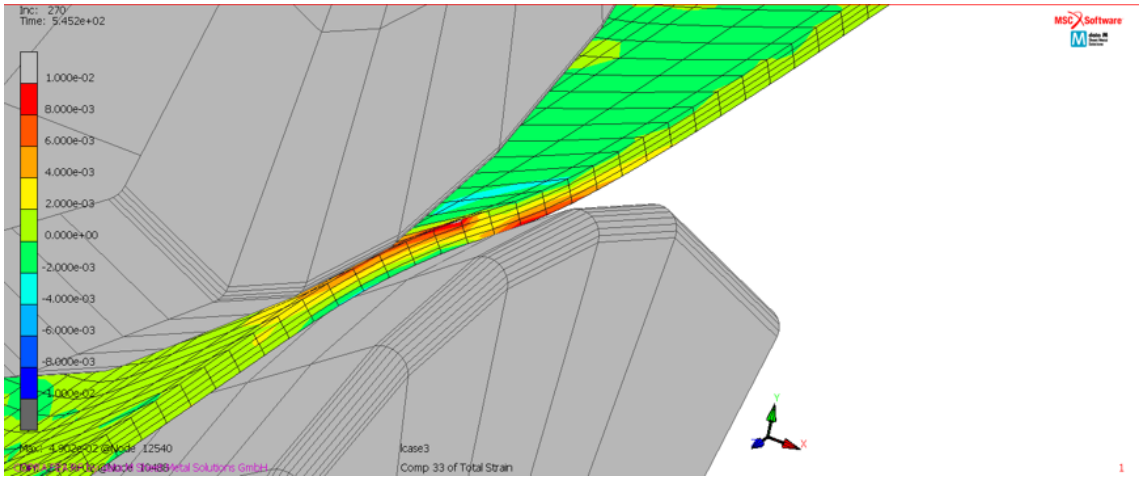



Figure 6.41: Longitudinal strain in station 2 for the model with 4 layers of solid element. The sheet undergoes longitudinal bending when entering the rolls

In order to study the peak values of longitudinal strain for all the elements, the values of longitudinal strain for a row of nodes (as seen in Figure 6.42) were collected. It is important to collect the values for more than one node to make sure the sudden increases and drops in longitudinal strain are captured. The peak values of longitudinal strain are summarized in Table 6.9, together with the corresponding station in which the peak occurs.

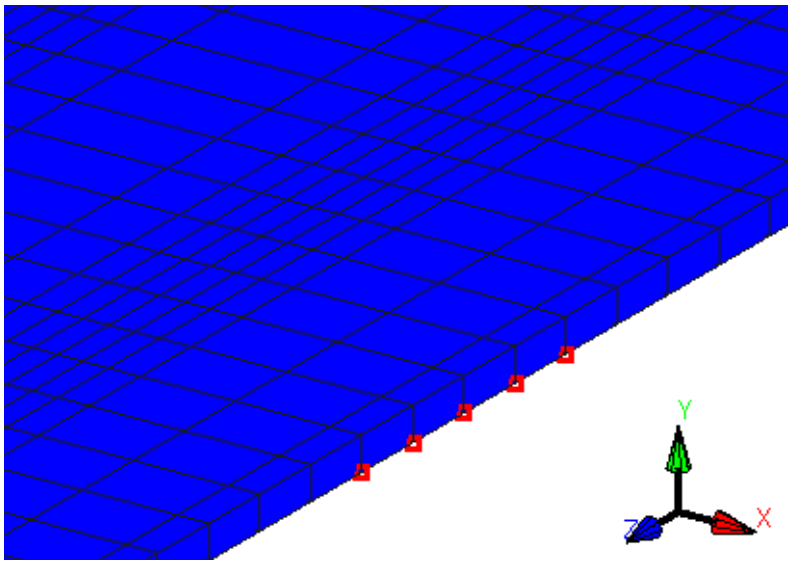


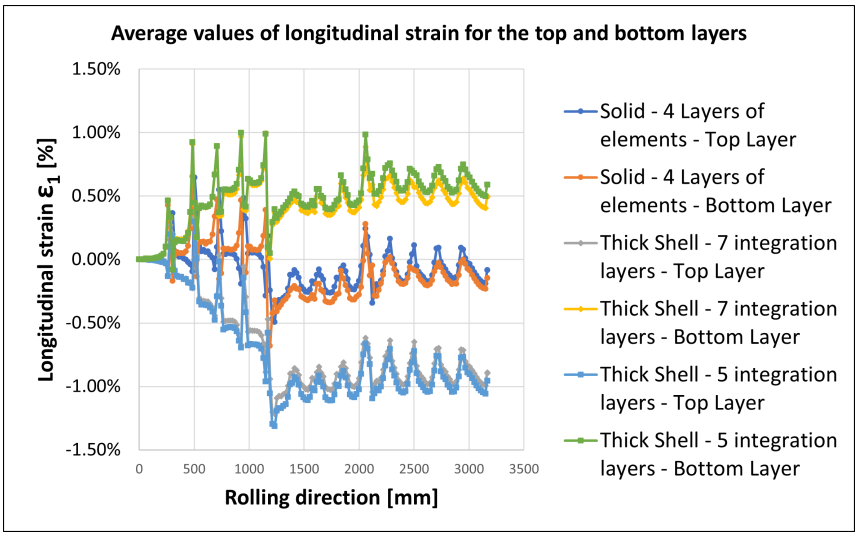

Figure 6.42: Row of nodes in the bottom layer where the longitudinal strain was collected

Table 6.9: Peak values of longitudinal strain and corresponding critical station

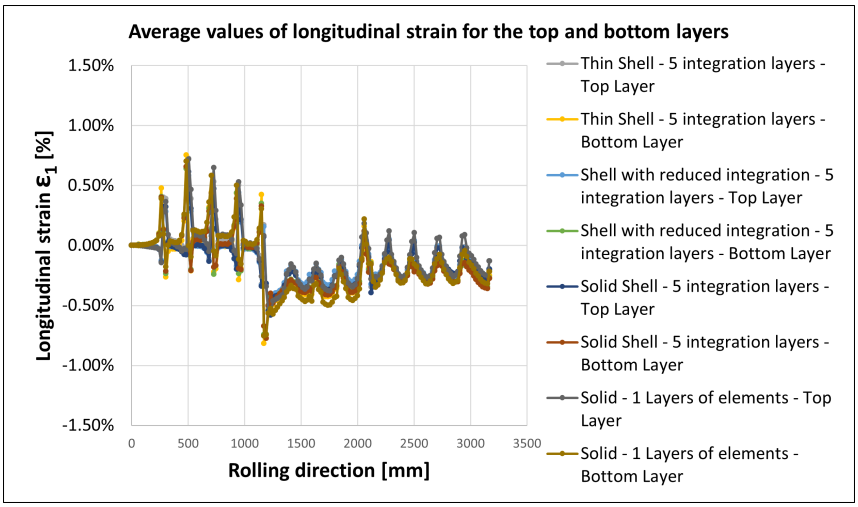
| | Peak negative longitudinal strain (%) | Station | Peak positive longitudinal strain(%) | Station |
|---|---|---|---|---|
| **Solid - 4 Layers of elements** | -1.29% | 5 | 0.90% | 2 |
| **Solid - 1 Layer of elements** | -1.29% | 5 | 0.94% | 2 |
| **Thick shell - 5 Integration Layers** | -0.47% | 5 | 1.15% | 9 |
| **Thick shell - 7 Integration Layers** | -0.54% | 5 | 1.14% | 5 |
| **Thin Shell - 5 Integration Layers** | -1.31% | 5 | 1.08% | 2 |
| **Shell with reduced Integration - 5 Integration Layers** | -1.38% | 5 | 0.77% | 2 |
| **SolidShell - 5 Integration Layers** | -1.23% | 5 | 0.84% | 2 |

The results for the thick shell elements are different than the results of the other models. For the positive peak of longitudinal strain, the two models with thick shell elements identify Station 5 and Station 9 as the critical stations. They still consider high strain values for the station which the other models considered as critical, Station 2, with the model with 5 integration layers reaching 1.13% longitudinal strain and the model with 7 integration layers reaching 0.84%. As for the negative peak value of longitudinal strain, the models with thick shell elements yield significantly smaller values of longitudinal strain for the bottom layer of the sheet, even though they still identify the same critical station. These values were not expected, especially since the models with other shell elements yield results similar to the reference model.

A more in-depth analysis was conducted to better understand the differences in the results. The values of longitudinal strain were collected for a row of nodes, from which an average curve was drawn. However, this time, both the bottom and top layers of the sheet edge were studied. The history of longitudinal strain for the bottom and top layers can be seen in Figure 6.43.



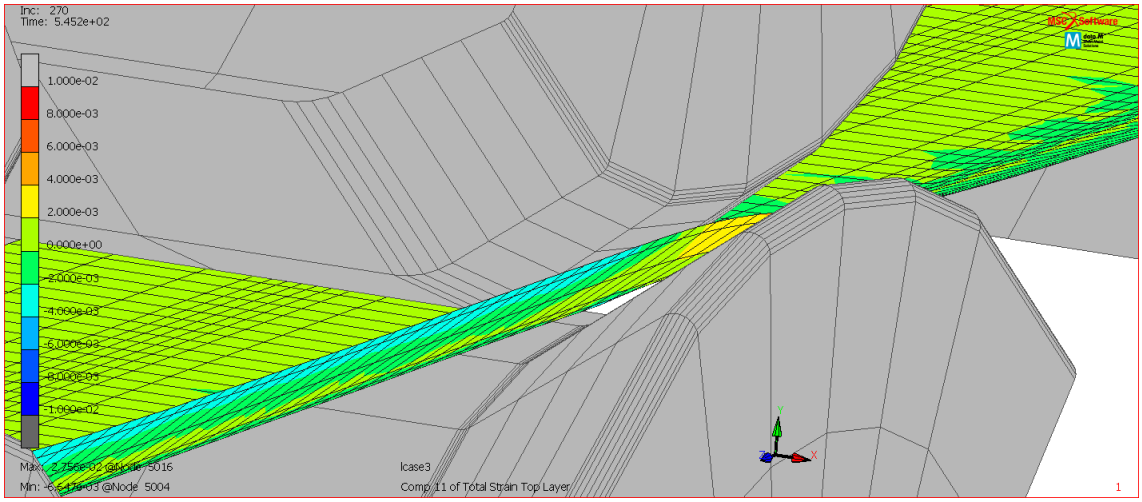

(a) Models with thick shell elements and 4 layers of solid elements



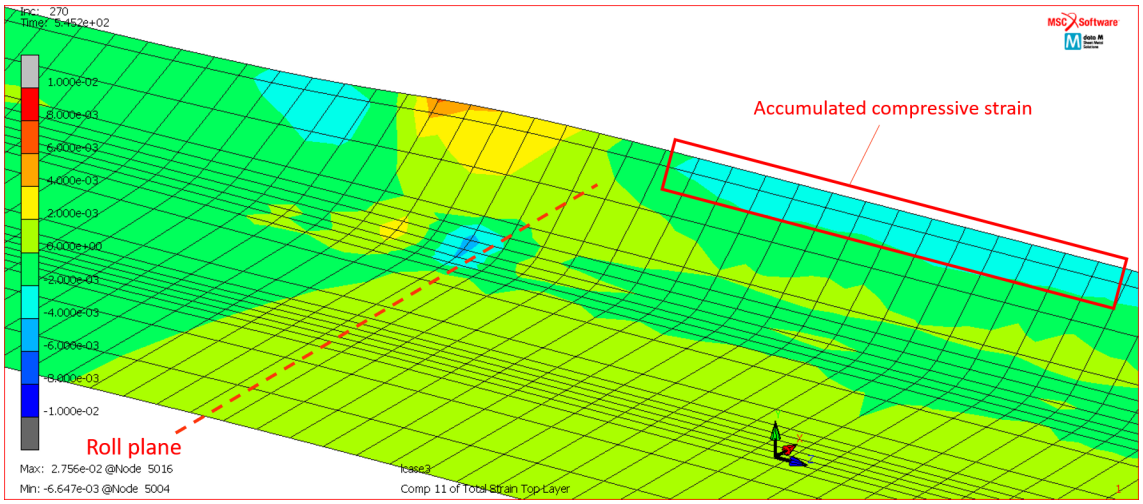

(b) Models with thin shell elements, shell elements with reduced integration, solid shell elements and 1 layer of solid elements

Figure 6.43: History of average value of longitudinal strain for the top and bottom layers of the sheet edge

Figure 6.43 shows that there is a uniform longitudinal strain distribution across the thickness of the sheet for the reference model. The models with thick shell elements experience a different behavior for the first five sections, where some longitudinal strain is accumulated in the top and bottom layers - the top layer accumulates compressive strain (as seen in Figure 6.44) and the bottom layer accumulates tensile strain. This generates a longitudinal strain gradient that, even with variations in longitudinal strain similar to the reference model after station five, results in the different peak values for the models with thick shell elements as was seen in Table 6.9.




(a) View including the rolls, similar to Figure 6.41




(b) Different view without the rolls

Figure 6.44: Top layer longitudinal strain in station 2 for the model with thick shell elements with 7 integration layers. The sheet undergoes longitudinal bending when entering the rolls and accumulates compressive strain in the top layer

The accumulation of strain for the outer layers of the sheet in the models with thick shell elements could not be explained.

It can be concluded that for the edge of the sheet:

- Models with 1 layer of solid elements, with thin shell elements, with shell elements with reduced integration, and with solid shell elements can accurately detect edge wave, having a similar representation of longitudinal strain yielding a uniform longitudinal strain distribution along the sheet thickness;
- Models with thick shell elements accumulate longitudinal strain for the first five stations, which leads to a gradient of longitudinal strain along the sheet thickness.

### 6.2.8 Thickness

As covered in Section 5.6, thinning of the sheet can occur on the bend lines. This phenomenon is more prone to occur for a bending radius close to the sheet thickness. The bends of the simulated C-shaped profile have a bending radius of $3mm$ and the thickness of the sheet is $2mm$, so some thickness reduction in the bend lines is expected [Marciniak et al. (2002)].

A post-processing tool, developed by Dr. Thomas Dietl from data M, was used in order to allow for a cross-section representation of shell elements. The tool extracts the results from the different layers of the shell elements and extrapolates them to solid elements. As the thickness nodal quantity is the same for all the layers, the values will remain the same across the two models.

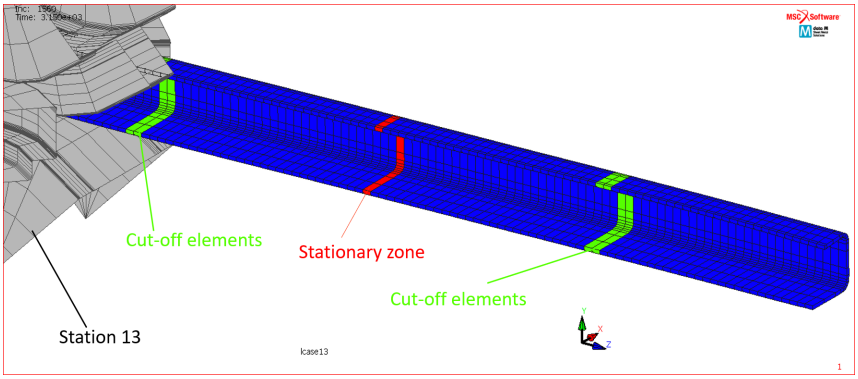


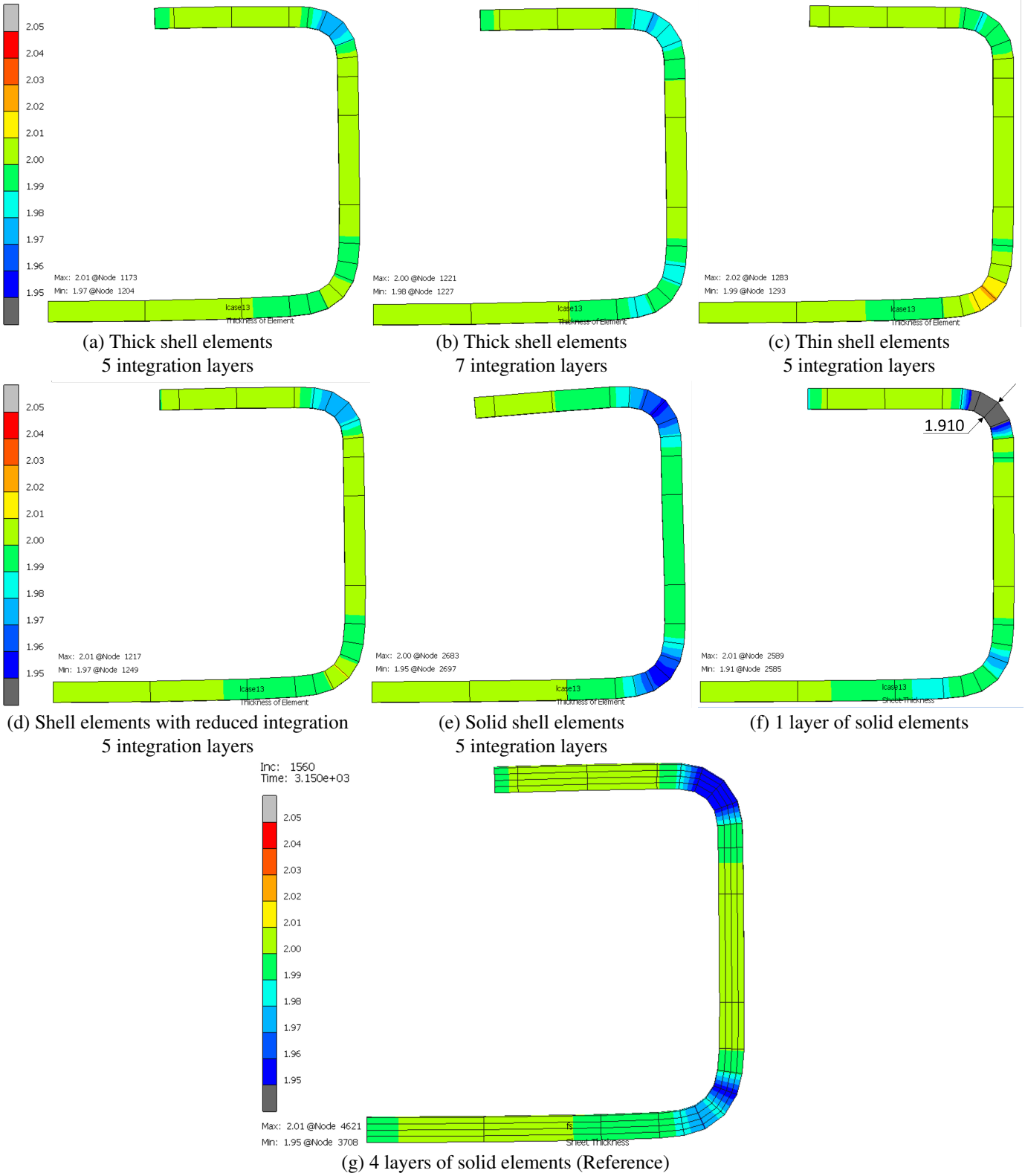

Figure 6.45: Sheet in the last increment before cut-off

Similar to what was done in Section 6.2.6 for the Total Equivalent Plastic Strain, the thickness will be analyzed at the end of the simulation in a stationary zone right before cut-off (Figure 6.45). Figure 6.46 shows the variation of thickness along the cross-section.

The shell elements underestimate the thinning of the sheet, which complies to the conclusions drawn in Section 5.6. This underestimation is critical for the model with thin shell elements, given the magnitude of the deviation and the fact that its thickness in bend $\beta$ even increased slightly, and is in line with the concerns raised by Gál and Lukacs (2020).

The solid element overestimates the thickness reduction for the $\alpha$ bend and might be a consequence of the locking behavior, verified in Section 6.2.3, for the area near the edge of the sheet. The solid shell element overestimates the thickness reduction for the $\beta$ bend.

The thinning for all the models had a magnitude not larger than $0.1mm$, corresponding to less than 5% of the sheet thickness. For smaller ratios of bending radius/sheet thickness, the thinning can be higher and reach values of 15% of the sheet thickness [Benson (2018)]. In those cases, the deviations seen for the shell elements and for just one layer of solid elements might become increasingly relevant.




(a) Thick shell elements
5 integration layers

(b) Thick shell elements
7 integration layers

(c) Thin shell elements
5 integration layers

(d) Shell elements with reduced integration
5 integration layers

(e) Solid shell elements
5 integration layers

(f) 1 layer of solid elements

(g) 4 layers of solid elements (Reference)

Figure 6.46: Cross-section view of the thickness of the elements

To sum up:

- The model with thin shell elements do not represent the thinning of the sheet;
- The models with thick shell elements and with shell elements with reduced integration represent the thinning of the sheet with an underestimation of its magnitude;
- The models with solid elements and solid shell elements represent the thinning of the sheet with an overestimation of its magnitude for some of the bends;

### 6.2.9 Computation time

The computation time, or CPU time, is an important result to analyze as it reflects the performance of the numerical models. It becomes even more important considering the nonlinearities involved in the numerical simulation of roll forming, and the demand for obtaining results as fast as possible. Table 6.10 shows the computation time for the different models.

Table 6.10: Results for the computation time of each model

| | **Elements** | **Nodes** | **Integration points** | **CPU Time [s]** |
|---|---|---|---|---|
| **Solid - 1 Layer of elements** | 2373 | 5016 | 18984 | 3854 |
| **Solid - 4 Layers of elements** | 9492 | 12540 | 75936 | 14734 |
| **Thick shell - 5 Integration Layers** | 2373 | 2508 | 47460 | 3501 |
| **Thick shell - 7 Integration Layers** | 2373 | 2508 | 66444 | 5811 |
| **Thin Shell - 5 Integration Layers** | 2373 | 2508 | 47460 | 2388 |
| **Shell with reduced Integration - 5 Integration Layers** | 2373 | 2508 | 11865 | 1725 |
| **Solid Shell - 5 Integration Layers** | 2373 | 5016 | 11865 | 1794 |

As foreseeable due to the reduced number of integration points, the models with reduced integration have the smallest CPU time, with a 55% time saving when compared with the default model with 1 layer of solid elements.

Even though the model with thick shell elements with 5 integration layers has 2.5 times more integration points, it still manages to yield results faster than the standard model with 1 layer of solid elements. For the model with thick shell elements, increasing the number of integration layers to 7 increases the CPU time by 65%.

It can also be seen that when there is the need for a better discretization in the thickness direction, using several layers of solid elements can drastically increase the computation time.

Figure 6.47 presents the values of computation time in minutes for a more expedite visualization.

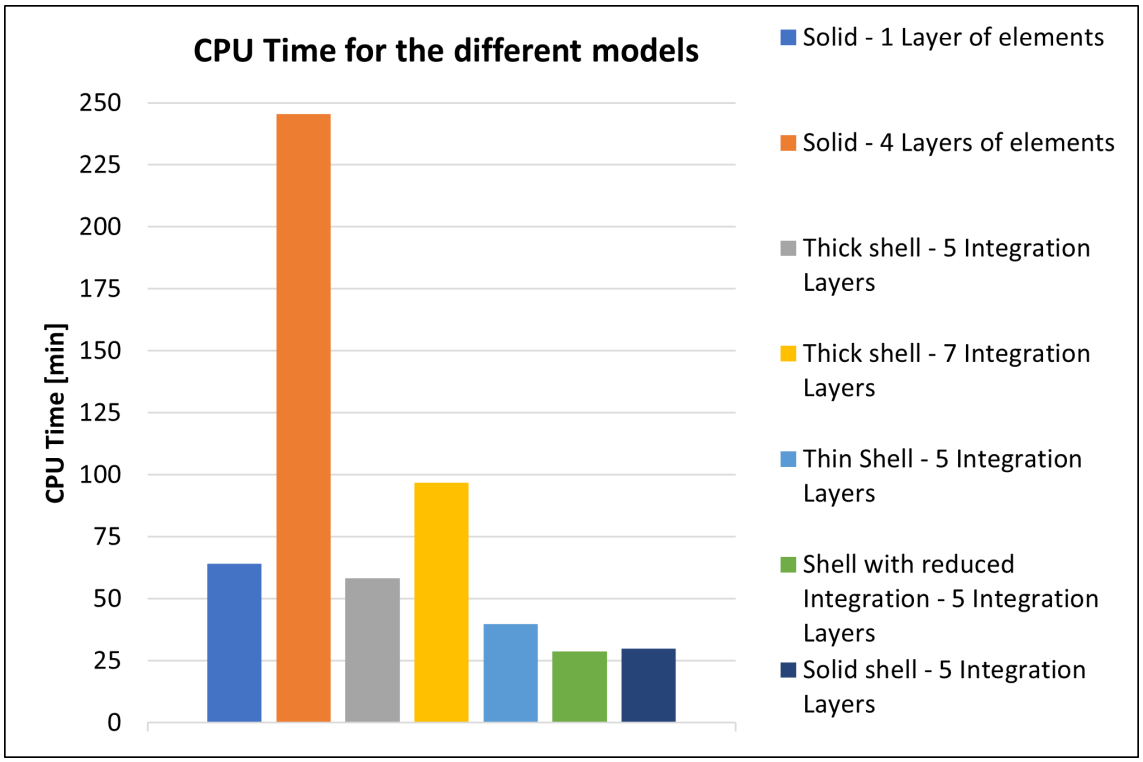



Figure 6.47: CPU time for the different models in minutes

To sum up, shell elements and elements with reduced integration are interesting in terms of computational costs. It is important to assure that, when using these alternative elements, good performance does not come at the expense of the reliability and accuracy of the results.

### 6.2.10 Discussion of the results

The different models had a wide variety of results depending on the analyzed parameters. Table 6.11 presents a summary of all the parameters analyzed. It is important to take into consideration that, when a model is stated to have a bad performance in a specific parameter, that is meant in comparison with the reference model.

For the models with thick shell elements, both five and seven integration layers present good results for some of the parameters. Not only was five the minimum number of integration layers recommended by MARC (2021b), the poor behavior of the model with thick shell elements with three integration layers was also confirmed, especially in terms of the geometrical representation of the profile. Using seven integration layers improves, indeed, the bending behavior of the elements, especially in terms of geometry accuracy. This improvement comes at the cost of increased computation time, which becomes 51% higher than the CPU time of the model with one layer of solid elements and 65% higher than the CPU time of the model with shell elements with five integration layers.

Table 6.11: Summary of the results of the roll forming numerical simulation

| | Contact establishment | | Defect representation | | Geometric accuracy | | | Additional parameters | | |
|---|---|---|---|---|---|---|---|---|---|---|
| | Double-sided contact | Edge contact | Edge wave | End flare | Thickness | Angle and springback Alfa | Angle and springback Beta | In-plane shear | Total Equivalent Plastic Strain | CPU Time [min] |
| Solid - 4 Layers of elements | * | | | | | | | | | 245.6 |
| Solid - 1 Layer of elements | | | | | | | | | | 64.2 |
| Thick shell - 3 integration layers | * | * | | | | | | | | |
| Thick shell - 5 integration layers | | | | | | | | | | 58.4 |
| Thick shell - 7 integration layers | * | * | | | | | | | | 96.9 |
| Thin Shell - 5 integration layers | * | * | | | | | | | | 39.8 |
| Shell with reduced Integration - 5 integration layers | * | * | | | | | | | | 28.8 |
| Solid shell - 5 integration layers | * | * | | | | | | | | 29.9 |

Reference model | Good performance | Satisfactory performance | Bad performance | Undetermined | * Assumption *

When compared with the model with thin shell elements, the model with shell elements with reduced integration performs worse in the representation of in-plane shear near the sheet edge, where the reduced integration scheme leads to a 10% underestimation of the in-plane shear stress, which also results in a poorer representation of the magnitude of end flare. Nonetheless, the model with shell elements with reduced integration manages to have a better representation of the profile's cross-section, especially in terms of the angle of the bend near the sheet edge and in terms of the thinning phenomenon in the bends, and a smaller computation time. Therefore, unless working with profiles that have drastic width reductions from station to station, which will induce high values of in-plane shear (phenomenon mentioned in Section 2.1.1.3), the shell elements with reduced integration are a better option than the thin shell elements.

When comparing the model with one layer of solid elements and the model with solid shell elements, for this particular profile, the latter has less accurate results only for the representation of end flare. The model with solid shell elements correctly represents the flaring direction but overestimates it by around 0.8°, does not suffer from locking issues as the model with solid elements, which result in an overestimation of the in-plane shear, and allows for the study of through-thickness variations of stresses and strains.

It is important to mention the limitations of some of the analyses made. The method for determining the angles was consistent across all the measurements, but drawing straight lines connecting only two nodes instead of considering more nodes, and using the nodes in the top layer for the brick elements and the nodes in the middle layer for the shell elements may lead to errors.

Moreover, the visualization method used might have had an impact on the drawn comparisons between models with solid elements, which only have two layers of integration through the thickness, and models with multiple layers of integration, such as the ones with shell elements or solid shell elements. For the models with multiple integration layers, the scalar results in the external

layers of the sheet were taken from the integration points. For the models with solid elements, in order to obtain the results in external layers of the sheet, the results calculated on the integration points, which are not in the faces of the elements (Figure 6.48), were linearly extrapolated.

The used comparison and visualization methods which relied on this extrapolation:

- could have impacted the study of the in-plane shear stress, as the through-thickness gradient of in-plane shear stress might not be exactly linear;
- are likely to have affected the analysis of the total equivalent plastic strain, as a linear extrapolation incorrectly represents the gradient yielded by the other models (positive values for the external layers of the sheet and values close to zero for the middle layer);
- did not affect the study of the edge wave, as for this particular profile the longitudinal strain gradient in the sheet edge was uniform through the thickness of the sheet.

The extrapolation has a smaller influence on the drawn conclusions for the model with four layers of solid elements than for the model with one layer of solid elements due to the difference in the through-thickness refinement of the meshes.

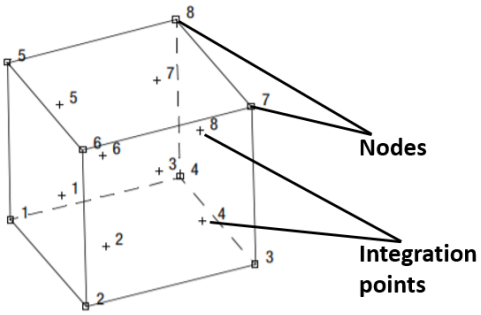



Figure 6.48: Visual representation of a eight-noded solid element with 8 integration points [MARC (2021b)]

To sum up, for each general model, it can be concluded that:

- **One layer of solid elements -** even though they undergo locking near the sheet edge, incorrectly representing the in-plane shear and the geometry of the inactive bend $\alpha$, they can accurately detect defects with a very good representation of end flare and edge wave. They have a good representation of the angle near the center of the sheet and manage to represent double-sided contact and its resulting forces.
- **Thick shell elements with three integration layers -** they do not present reliable results and are not a viable option for the finite element analysis of roll forming.
- **Thick shell elements with five integration layers -** they present a 10% reduction of computational costs when compared to the model with one layer of solid elements, and have no issues yielding in-plane shear stress near the sheet edge, accurately representing the angle

near the sheet edge. The main limitations of the model with thick shell elements and five integration layers reside in the representation of the contact forces when in the presence of double-sided contact, and in the representation of longitudinal strain near the sheet edge.

- **Thick shell elements with seven integration layers -** they present a 60% reduction of computational costs when compared to the model with four layers of solid elements, but a 51% increase when compared to the model with one layer of solid elements. They have no issues yielding in-plane shear stress near the sheet edge and have the best representation of the geometry of the bends among all the alternatives. The main limitations of the model with thick shell elements and seven integration layers reside in the representation of the contact forces when in the presence of double-sided contact, and in the representation of longitudinal strain near the sheet edge.

- **Thin shell elements with five integration layers -** they have small computational costs and are the only elements apart from the solid elements which can represent both end flare and edge wave correctly. The main limitation of the model with thin shell elements resides in the geometric representation of the bends.

- **Shell elements with reduced integration with five integration layers -** they have the smallest computation time among all the models. However, the model with shell elements with reduced integration raises concerns on the representation of in-plane shear associated with the transverse deformation of the sheet and on the representation of the correct magnitude of end flare.

- **Solid shell elements with five integration layers -** they have small computational costs. Alongside the models with solid elements, the model with solid shell elements is expected to be able to represent double-sided contact. Even though the model with solid shell elements raises some concerns on the representation of in-plane shear associated with the transverse deformation of the sheet and on the representation of the correct magnitude of end flare, it was the only model that did not have a bad performance in any of the analyzed parameters.

# Chapter 7

# Conclusions

The main goal of the present project was to study different element formulations in the finite element analysis of a roll forming process, ideally reaching a reliable alternative to the standard models created by COPRA® FEA RF. The roll forming process was studied, namely the forming mechanisms and the most common defects, which allowed to establish the most meaningful analysis parameters and to conduct an insightful analysis of the results.

Five is the minimum number of integration layers when using shell elements for a correct simulation of roll forming. The bending behavior of the sheet is not accurately represented when using three layers of integration, which leads to issues in exhibiting the geometry of the profile. Other model parameters also have an impact on the performance of the shell models. Increasing the contact bias factor and defining the sheet's deformable contact body with a smooth boundary condition can solve convergence issues.

Double-sided contact is prone to occur in a roll forming process. Shell elements cannot represent double-sided contact as they represent the geometry of the body in a reference surface, instead of in a brick with defined volume like the solid and solid shell elements, and each node can only be in contact with one contact body at a time. When double-sided contact occurs, the forces in the rolls are expected to become higher. As the shell elements do not represent the increase in the roll forces, yielding results as if there was no double-sided, and as shell elements cannot be used to detect double-sided contact, the results of the forces in the rolls for shell elements are not reliable.

Lateral edge contact was also tested due to the concern that shell elements would only be suitable for the simulation of in-plane forces. Differences can arise in the contact forces when contact is established laterally in the edge of the sheet, but they are not connected to a bad establishment of contact. Thus, lateral edge contact itself is not a limitation to any of the tested elements.

There is a high incidence of in-plane shear stresses for the edge portion of the sheet due to its width reduction from station to station. The model with solid elements exhibits a locking behavior, overestimating in-plane shear stresses. Due to the reduced number of integration points, elements with reduced integration underestimate in-plane shear stresses, a phenomenon which is expected to worsen when using a coarser mesh.

For the correct portrayal of the profile's geometry and of the springback phenomenon, the

models with thick shell elements with seven layers of integration is the only model to depict both bends accurately (apart from the reference model with four layers of solid elements). Models with thick shell elements and with shell elements with reduced integration have a good representation of the angle near the sheet edge. Models with solid elements and solid shell elements have a good representation of the angle near the center of the sheet.

The release of residual stresses after cut-off has an impact on the angularity of the ends of the sheet. This phenomenon known as end flare is only correctly pictured by models with solid elements, thick shell elements, and thin shell elements. Models with elements with reduced integration overestimate the magnitude of end flare.

The material of the sheet plastifies densely in the area of the bends, resulting in high magnitudes of Total Equivalent Plastic Strain for the outer layers of the sheet. The model with only one layer of solid elements fails to represent the neutral layer, as a result of its trilinear interpolation formulation with only two layers of integration through the thickness. This can be a drawback when there is the need to study the behavior of the material fibers.

High values of longitudinal strain are prone to arise in the edge of the sheet, which can lead to elastoplastic buckling and edge wave. The longitudinal strain and its drastic variations were accurately depicted by all the models except the ones with thick shell elements, which accumulate longitudinal strain for the first stations.

Thinning of the sheet occurs in the bending areas. The thickness reduction is of small magnitude for this profile, due to the not so small ratio between the bending radius and the thickness of the sheet, being only poorly represented by the model with thin shell elements.

For the studied profile, all the models managed to converge. The roll forming industry recognizes the robustness of models with solid elements, which are usually exempt from extensive parameter tuning. Different profiles need to be studied to assure that the alternative element formulations do not suffer from convergence issues.

To summarize, each element formulation has its limitations. The studied element formulations can indeed reduce computational costs. In an industrial context it is imperative that the product defects are detected, and none of the models, apart from the reference model, managed to accurately depict all the defects and the entire geometry of the profile. Thus, there is the need for future studies on the possibility of combining different element formulations, in order to develop roll forming models that successfully represent the behavior of the sheet.

## 7.1 Future work

The present work identified potential element formulations which can possibly be used in the numerical simulation of a specific roll forming process. Further steps should be taken to assure the applicability of the element formulations in different situations and to optimize the models, namely:

- To conduct single element tests with applied and released loads to better understand the elastic recovery and the release of stresses for the different element formulations;

- To study the mesh sensitivity of the different models; this is even more relevant for the models with elements with reduced integration, which are greatly impacted by the discretization of the mesh;

- To study the use of adaptive remeshing;

- To study the quality of the results for the models with shell elements without using the recommend enhanced transverse shear formulation; removing this formulation could result in even faster computation times but can reduce the accuracy of the results;

- To study the eight-noded solid elements with reduced integration from the Marc/Mentat library (mainly Element 117), considering the performance of the elements with reduced integration during this work which led to the reduction of computational costs; as the element type only has one integration point, it is expected that two or more layers of elements will be needed for the models;

- To study the roll forming of different profiles; solid elements are a robust option for the numerical simulation of roll forming and the robustness of the other element types should also be assessed; complex profiles with a higher amount of bends might be a threat for the elements with reduced integration which rely on a good mesh discretization for the representation of in-plane shear; profiles with higher bending radii should also be considered since it was verified during the air bending tests in Section 5.6 that the elements have different behaviors for different bending radii;

- To evaluate the impact of considering friction and driven rolls in the models, especially for double-sided contact situations;

- To study in even more detail the use of solid shell elements, whose model did not have a bad performance in any of the analyzed parameters and presented small computational costs; this element formulation is relatively new when compared with the other element types, is a recent trend in the roll forming industry and thus, there is a lot of room for research, such as in the tendency of the element to lock (as occurred in Section 5.5) and in the impact of the enhanced transverse shear parameter in its results;

- To study the coupling of different element types; for the profile studied in this work, a coupling between solid shell elements and shell elements with reduced integration could be recommended: using solid shell elements near the center of the sheet, including the bend $\beta$ and shell elements with reduced integration for the edge portion of the sheet, including the bend $\alpha$;

- To study the use of different numbers of layers of solid elements for different areas of the sheet; due to some of the issues verified for the model with one layer of solid elements, mainly in regards to accurate through-thickness distributions, four layers of solid elements

could be used exclusively for the bending areas allowing for a compromise between reliability and performance;

- To study a roll forming process with punched holes;
- To validate the numerical results and drawn conclusions with experimental results.

# References


Abaqus (2021). Reduced integration. Available at: https://abaqus-docs.mit.edu/2017/English/SIMACAEGSARefMap/simagsa-c-ctmreduced.htm.

Autodesk (2018). Thin parts can have inaccurate results when using solid elements. Available at: https://knowledge.autodesk.com/support/inventor-nastran/troubleshooting/caas/sfdcarticles/sfdcarticles/Thin-parts-can-have-inaccurate-results-when-using-solid-elements.html, accessed June 2021.

Barrett, P. R. (2014). Debugging complex finite element analysis using a single element model. Available at: https://www.engineering.com/story/debugging-complex-finite-element-analysis-using-a-single-element-model, accessed March 2021.

Batchu, S. (2015). Stress ebook. Available at: https://www.stressebook.com/rigid-body-mode/, accessed May 2021.

Bathe, K. J. (2014). *Finite element procedures* (Second ed.). K.J. Bathe, Watertown, MA.

Belytschko, T., J. S.-J. Ong, W. K. Liu, and J. M. Kennedy (1984). Hourglass control in linear and nonlinear problems. *Computer Methods in Applied Mechanics and Engineering 43*(3), 251–276.

Bengzon, F., T. Borrvall, and U. Basu (2018). An enhanced assumed strain (eas) solid element for nonlinear implicit analysis. In *15th International LS-DYNA Users Conference*, pp. 1–9.

Benson, S. (2015a). Bending basics: 6 steps to successful die selection for press brakes. Web-article from The Fabricator, available at: https://www.thefabricator.com/thefabricator/article/bending/bending-basics-6-steps-to-successful-die-selection-for-press-brakes, accessed April 2021.

Benson, S. (2015b). How an air bend turns sharp. Web-article from The Fabricator, available at: https://www.thefabricator.com/thefabricator/article/bending/how-an-air-bend-turns-sharp, accessed April 2021.

Benson, S. (2018). Press brake bending basics: Die angles, tonnage, and k-factors. Web-article from The Fabricator, available at: https://www.thefabricator.com/thefabricator/article/bending/press-brake-bending-basics-die-angles-tonnage-and-k-factors, accessed April 2021.

Betsch, P. and E. Stein (1996). A nonlinear extensible 4-node shell element based on continuum theory and assumed strain interpolations. *Journal of Nonlinear Science 6*(2), 169–199.

Bhattacharyya, D., P. Smith, S. Thadakamalla, and I. Collins (1987). The prediction of roll load in cold roll-forming. *Journal of Mechanical Working Technology 14*(3), 363–379.

Bischoff, M. and E. Ramm (1997). Shear deformable shell elements for large strains and rotations. *International Journal for Numerical Methods in Engineering 40*(23), 4427–4449.

Boman, R., L. Papeleux, B. Viet, J.-P. Ponthot, P. Wouters, and R. Kergen (2005). An ale model for numerical simulation of cold roll forming process. *778*, 768–773.

Brunet, M. and S. Ronel (1994). Finite element analysis of roll-forming of thin sheet metal. *Journal of Materials Processing Technology 45*(1), 255–260.

Bucalem, M. L. and K.-J. Bathe (2011). *The Mechanics of Solids and Structures – Hierarchical Modeling and the Finite Element Solution*. Springer-Verlag Berlin Heidelberg.

Chernov, N. and C. Lesort (2005). Least squares fitting of circles. *Journal of Mathematical Imaging and Vision 23*(3), 239–252.

Crutzen, Y., R. Boman, L. Papeleux, and J.-P. Ponthot (2016). Lagrangian and arbitrary lagrangian eulerian simulations of complex roll-forming processes. *Comptes Rendus Mécanique 344*(4), 251–266. Computational simulation of manufacturing processes.

Dassault Systèmes Simulia Corp (2011). *Abaqus 6.11, Abaqus/CAE User's Manual*. United States: Dassault Systèmes Simulia Corp.

data M Sheet Metal Solutions GmbH (2021). About us. Available at: https://www.datam.de/en/about-us, accessed March 2021.

DIANA FEA (2017). *DIANA-10.1 User's Manual - Theory* (First ed.). DIANA FEA BV.

Fernandes, J., D. Rodrigues, L. Menezes, and M. Vieira (1998). A modified swift law for pre-strained materials. *International Journal of Plasticity 14*(6), 537–550.

Ferreira, P. B. F. (2016). Roll forming - a study on machine deflection by means of experimental analysis and numerical developments.

Gao, J. F., Q. Li, and W. Zhao (2013). Thermal stress analysis for local heating variable cross-section roll forming. In *Advanced Materials and Engineering Materials II*, Volume 683 of *Advanced Materials Research*, pp. 599–603. Trans Tech Publications Ltd.

Groche, P. and C. Müller (2013). Merkblatt 180–walzprofilieren von flacherzeugnissen aus stahl. *Düsseldorf: Stahl-Informations-Zentrum*.

Groover, M. P. (2010). *Fundamentals of Modern Manufacturing: Materials, Processes, and Systems* (Fourth ed.). John Wiley & Sons.

Gu, P. (2021). Contact analysis and its parameter settings. Available at: http://docshare01.docshare.tips/files/8033/80335917.pdf, accessed April 2021.

Gál, V. and Z. Lukacs (2020). Numerical modelling of the thinning behaviour of sheet metal parts. *IOP Conference Series: Materials Science and Engineering 903*, 012055.

Halmos, G. T. (2006). *Roll Forming Handbook* (First ed.). Taylor & Francis Group.

Han, F., Y. Wang, and L.-l. Niu (2019). Deformation mechanism analysis of roll forming for q&p980 steel based on finite element simulation. *Journal of Iron and Steel Research International 26*.

Heislitz, F., H. Livatyali, M. A. Ahmetoglu, G. L. Kinzel, and T. Altan (1996). Simulation of roll forming process with the 3-d fem code pam-stamp. *Journal of Materials Processing Technology 59*(1), 59–67. Selected Papers on Metal Forming and Machining.

Hellborg, S. (2007). Finite element simulation of roll forming.

Hickey, K. (2020). Roll forming ahss. Available at: https://www.ahssinsights.org/news/roll-forming-ahss/, accessed April 2021.

Jimma, T. and H. Ona (1981). Optimum roll pass schedules on the cold roll forming process of symmetrical channels. In *Proceedings of the Twenty-First International Machine Tool Design and Research Conference*, pp. 63–67. Springer.

Li, D. Y., Y. B. Luo, and Y. H. Peng (2007). Solid shell element and its application in roll forming simulation. In *Engineering Plasticity and Its Applications*, Volume 340 of *Key Engineering Materials*, pp. 347–352. Trans Tech Publications Ltd.

Li, J.-c., S. Li, Z. Xie, and W. Wang (2015). Numerical simulation of incremental sheet forming based on gtn damage model. *The International Journal of Advanced Manufacturing Technology 81*.

Li, L., D. Li, and Y. Peng (2011). The simulation of sheet metal forming processes via integrating solid-shell element with explicit finite element method. *Eng. Comput. (Lond.) 27*, 273–284.

Lia, L., Y. Peng, and D. Li (2010). Explicit simulation of roll forming process with eas solid-shell elements. *AIP Conference Proceedings 1252*, 1223–1230.

Lindgren, M. (2005). Modelling and simulation of the roll forming process.

Lindgren, M., U. Bexell, and L. Wikström (2009). Roll forming of partially heated cold rolled stainless steel. *Journal of Materials Processing Technology 209*(7), 3117–3124.

Logan, D. L. (2007). *A First Course in the Finite Element Method* (Fourth ed.). Thomson.

LS-DYNA (2021). Hourglass. Available at: https://www.dynasupport.com/howtos/element/hourglass, accessed March 2021.

Lundh, H. (1997). *Formningshandboken: styckskärande bearbetning och plastisk formning*. SSAB Tunnplåt.

Mahajan, P., A. Abrass, and P. Groche (2018). Fe simulation of roll forming of a complex profile with the aid of steady state properties. *steel research international 89*(5).

MARC (2021a). Volume a: Theory and user information. Document extracted from the user documentation of the Marc/Mentat software.

MARC (2021b). Volume b: Element library. Document extracted from the user documentation of the Marc/Mentat software.

Marciniak, Z., J. Duncan, and S. Hu (2002). 6 - bending of sheet. In Z. Marciniak, J. Duncan, and S. Hu (Eds.), *Mechanics of Sheet Metal Forming (Second Edition)* (Second Edition ed.)., pp. 82–107. Oxford: Butterworth-Heinemann.

Mars, J., S. Koubaa, W. M., and D. Fakhreddine (2017). Numerical analysis of geometrically non-linear behavior of functionally graded shells. *Latin American Journal of Solids and Structures 14*, 1847–1873.

Martins, A. S. S. (2018). Simulation of cold rolling process of steel profiles for shelter applications.

Mises, V. (1913). Mechanik der festen körper im plastisch- deformablen zustand. *Nachrichten von der Gesellschaft der Wissenschaften zu Göttingen, Mathematisch-Physikalische Klasse 1913*, 582–592.

Mohd Saffe, S. N., T. Nagamachi, and H. Ona (2014). Mechanism of end deformation after cutting of light gauge channel steel formed by roll forming. *Journal of the Japan Society for Technology of Plasticity 55*, 331–335.

Moneke, M. and P. Groche (2018). End flare of profiles with multiple bending zones. *Procedia Manufacturing 15*, 743–750. Proceedings of the 17th International Conference on Metal Forming METAL FORMING 2018 September 16 – 19, 2018, Loisir Hotel Toyohashi, Toyohashi, Japan.

Natal, R. J. (2017). Sebenta: Mecânica das estruturas. Lecture Notes for the course "Structural Mechanics" Department of Mechanical and Industrial Management Engineering, Faculty of engineering of the University of Porto.

Öchsner, A. (2014). Bending of beams. In *Elasto-Plasticity of Frame Structure Elements: Modeling and Simulation of Rods and Beams*, Berlin, Heidelberg, pp. 55–149. Springer Berlin Heidelberg.

Panton, S., S. Zhu, and J. Duncan (1994). Fundamental deformation types and sectional properties in roll forming. *International Journal of Mechanical Sciences 36*(8), 725–735.

Pari, M., J. Rots, and M. Hendriks (2018). Non-proportional loading for 3-d stress situations in sequentially linear analysis. In G. Meschke, B. Pichler, and J. G. Rots (Eds.), *Computational Modelling of Concrete Structures* (First Edition ed.)., pp. 931–940. London: Taylor & Francis Group.

Plumbridge, W. J., R. J. Matela, and A. Westwater (2003). Non-linear finite element analysis. In *Structural Integrity and Reliability in Electronics: Enhancing Performance in a Lead-Free Environment*, pp. 305–318. Springer Netherlands.

Safari, M. and J. Joudaki (2018). Ovality and bow defect of pre-punched sheets in roll forming of trapezoidal sections. pp. 1123–1128.

Safdarian, R. and H. Moslemi Naeini (2015). The effects of forming parameters on the cold roll forming of channel section. *Thin-Walled Structures 92*, 130–136.

Sajjad, M., M. Murugesanb, and D. W. Jung (2020). Investigation of bow defect in roll forming. *IOP Conference Series: Materials Science and Engineering 758*, 012069.

Senanayake, R., I. Cole, and S. Thiruvarudchelvan (1994). The application of computational and experimental techniques to metal deformation in cold roll forming. *Journal of Materials Processing Technology 45*(1), 155–160.

SSAB (2018). Docol® 600dp. Material data sheet available at: https://www.ssab.com/api/sitecore/Datasheet/GetDocument?productId=02EE86D9374C4484AE76F56E86F2B92B&language=en, accessed May 2021.

Stoughton, T., M. Shi, G. Huang, and J. Yoon (2013). Material characterizations for benchmark 1 and benchmark 2. Volume 1567, pp. 9–14.

Swift, H. (1952). Plastic instability under plane stress. *Journal of the Mechanics and Physics of Solids 1*(1), 1–18.

Tata Steel (2016). Cold-rolled dp600-uc. Available at: https://www.tatasteeleurope.com/ts/sites/default/files/tata-steel-automotive-cr-dp600-uc-cr330y590t-hct590x-dual-phase-datasheet-EN.pdf, accessed May 2021.

Timoshenko, S. (1953). *History of strength of materials*. McGraw-Hill.

UBECO GmbH (2021). Profil product information. Available at: https://www.ubeco.com/profil.htm, accessed March 2021.

Velling, A. (2019). Sheet metal bending – methods, design tips & k factor. Available at: https://fractory.com/sheet-metal-bending/, accessed April 2021.

Vlassak, J. J. (2011). Linear elasticity. Available at: https://scholar.harvard.edu/files/jiaweiyang/files/3_principle_of_virtual_work_and_fem.pdf.

Wang, A., K. Zhong, O. El Fakir, J. Liu, C. Sun, L.-L. Wang, J. Lin, and T. A. Dean (2017). Springback analysis of aa5754 after hot stamping: experiments and fe modelling. *The International Journal of Advanced Manufacturing Technology 89*(5), 1339–1352.

Wang, M., Z.-Y. Cai, L.-L. Li, and M.-Z. Li (2015). Longitudinal bending deformation analysis of sheet metal in continuous roll forming process. *The International Journal of Advanced Manufacturing Technology 80*.

Wang, P., H. Chalal, and F. Abed-Meraim (2017). Quadratic solid–shell elements for nonlinear structural analysis and sheet metal forming simulation. *Computational Mechanics 59*, 161–186.

Wang, X., Y. Xu, and R. Jackson (2018). Theoretical and finite element analysis of static friction between multi-scale rough surfaces. *Tribology Letters 66*.

Weiss, M., H. Wolfkamp, B. Rolfe, P. Hodgson, and E. Hemmerich (2009). Measurement of bending properties in strip for roll forming. *International Deep Drawing Research Group*, 521–532.

Xia, Z. C. and S. C. Tang (1999). Locking phenomena in the use of solid elements for sheet metal forming simulation. *SAE Transactions 108*, 862–868.

Yan, Y., F.-H. Jia, and H.-C. Zhang (2015). Fem and springback analysis of dp980 steel roll forming based on different elements. *22*, 63–67.

Yu, H.-C., H.-Y. Chen, and K. Thornton (2009). Smoothed boundary method for solving partial differential equations with general boundary conditions on complex boundaries.

Zhang, Y., H.-P. Nguyen, and D. W. Jung (2016). Optimization of the spring-back in roll forming process with finite element simulation. *International Journal of Mechanical Engineering and Robotics Research 5*.

Zienkiewicz, O., R. Taylor, and J. Zhu (2013). Chapter 8 - the patch test, reduced integration, and nonconforming elements. In O. Zienkiewicz, R. Taylor, and J. Zhu (Eds.), *The Finite Element Method: its Basis and Fundamentals* (Seventh Edition ed.)., pp. 257–284. Oxford: Butterworth-Heinemann.